Efficiency and Linearity Improvement of Sub-6GHz Digital Beam-forming Transmitters

by

Hang Yu

A thesis
presented to the University of Waterloo
in fulfillment of the
thesis requirement for the degree of
Master of Applied Science
in
Electrical and Computer Engineering

Waterloo, Ontario, Canada, 2021

Author's Declaration

I hereby declare that I am the sole author of this thesis. This is a true copy of the thesis, including any required final revisions, as accepted by my examiners.

I understand that my thesis may be made electronically available to the public.

Abstract

The fifth-generation (5G) cellular network promises to bring higher data capacity, faster transmission speeds, and lower latency. 5G employs massive multiple-input multiple-output (mMIMO) architecture, a configuration that incorporates many more transceivers and antennas than 4G architectures, thus allowing for higher capacity and beam-forming capability. Since many more transceivers and antennas are being deployed, the RF front-ends used in these components need to be more compact, cheaper, and lighter and fit a similar physical footprint within 4G LTE base-station cell towers. One of the more profound changes made to RF hardware in an effort to reduce its size and weight is the removal of isolators/circulators between the power amplifiers (PA) and antennas, a change which brings with it the issue of isolation between the PAs' output and the antennas' input. A PA's performance (e.g., linearity, output power, efficiency) relies heavily on the impedance seen by the drain of the transistor. When the isolator is removed at the PA load, the limited isolation between the PA and antenna elements will cause significant losses in PA performance due to the significantly varying active antenna impedance during MIMO operations.

This work presents a 2x2 array of class AB PAs connected to an antenna array with re-configurable spacing and a study of the effects of antenna cross-talk on the linearizability and efficiency performance of 5G sub-6GHz wide-band mMIMO transmitters. The antenna array is formed of modular dual-polarized patch antenna components which measured -40dB in isolation between polarization ports and a -10dB bandwidth of 3.2 to 3.7GHz for both polarization ports. The antenna array inter-element spacing can be reconfigured to be 0.6λ, 0.7λ or 0.8λ, which corresponds to -21dB, -24dB, and -26dB in coupling levels respectively, to study the effect of antenna cross-talk during MIMO operation. The class AB PA is designed using gallium nitride transistors. Under continuous-wave excitation, single PA element measurements show a small signal gain of 12.5 ± 0.5dB, saturation powers of 36 to 37dBm, and drain efficiencies of 59 to 67%. A custom-built front-end frame is designed to accommodate both the PA and antenna arrays in a compact fashion while enabling the front-end transmitter to extend from 2x2 up to, but not limited to, a 6x6 array configuration. The ability of both single-input single-output (SISO) and dual-input single-output (DISO) digital predistortion (DPD) techniques to linearize the PA arrays is also assessed under 5G-candidate 100 MHz orthogonal frequency-division multiplexing test signals. From the measurement results, it was clear that the DISO DPD successfully linearized the transmitter front-end [adjacent channel power ratio (ACPR) under -48dBc] for the MIMO front-end for all re-configurable scenarios. The measurement results reveal that antenna load mismatch is the dominant factor affecting performance degradation in

MIMO systems, impacting output power, efficiency, and linearity. While antenna cross-talk mainly impacts linearity, degrading ACPR under SISO DPD, DISO DPD can successfully linearize the transmitter front-end in all scenarios.

Acknowledgements

I would most importantly like to thank my parents, Jean Zhu and Hunter Yu, for supporting me throughout my hardships. They alone have made this thesis possible.

I would like to thank Professor Slim Boumaiza for his guidance and mentorship, as well as for providing me the opportunity to study and work in the Emerging Radio Systems Group (EmRG).

I would like to thank Jingjing Xia, for helping with software, fabrication assembly, and measurement setups.

I would like to thank Mohammed Almoneer, for providing algorithms and helping with measurement setups.

Last and certainly not least, I would like to thank all EmRG colleagues who have participated in conversations with me. In specific, Emile Traore and Jin Gyu-Lim for lending a hand in times of need and helping me develop new perspectives. I thank you.

Table of Contents

List of Figures

List of Tables

Chapter 1

Introduction

1.1 Motivation

The evolution from fourth-generation (4G) to fifth-generation (5G) communication technologies and the anticipated 100x capacity improvement required by our ever-increasing demand for data requires a fundamental change in cellular communication RF system architectures and designs. With so many users, devices, automobiles, smart meters, low-power wide-area devices, and other machine-to-machine communication, the capacity of 4G cellular systems that employ fixed sector antenna systems will fall short [14]. In order to meet the massive data demands, 5G communication systems will use technologies such as ultra-densification to improve the area spectral efficiency, millimeter wave (mmWave) frequencies, and integration with WiFi's unlicensed spectrum in the 5GHz band for increased bandwidth, and massive multiple input multiple output (mMIMO) architectures to support more bits/s/Hz per node [2].

The implementation of 5G technologies such as mMIMO will bring drastic changes in the radio frequency (RF) design realm, especially transmitter components such as power amplifiers (PAs) in base stations (BS), as the broadband modulation bandwidths for 5G RF transmitters will require high power efficiency and stringent linearity from the PAs. With future 5G communication infrastructure heading towards mMIMO infrastructure, and with the increasing bandwidth and frequency of operation, many traditional design strategies used for 4G will not work for 5G.

A current focus in communication infrastructure design is multi-user mMIMO systems for the sub-6GHz spectrum. Here, a BS with multiple antennas simultaneously serves a

set of single-antenna users, and the multiplexing gain can be shared by all users [22]. In theory, the multi-user mMIMO concept demonstrates that the combination of multiple data streams provides high directivity and high robustness, and eliminates uncorrelated noise and signal distortion due to hardware impairments and small-scale channel fading [22].

To utilize the advantages of mMIMO systems, the RF front-end will need to incorporate high volumes of active antennas with multiple signal channels (Figure 1.1). Thus, the PAs employed in 5G wireless applications will be much different from those employed in 4G networks. In traditional PA designs, the dominant focus was power efficiency since 4G transmitters used only one highly efficient, high-power Doherty PA in conjunction with digital pre-distortion (DPD) to enhance the linearity. This concept is not compatible with mMIMO transmitters because mMIMO infrastructure requires multiple PAs with multiple antennas all implemented on a highly integrated platform, leaving no space (or cost allowance) for additional isolators between the PA and antenna elements as was possible within previous-generation transmitters. Due to the lack of isolators, the signals emitted by one antenna can be coupled to another antenna with limited isolation within the array and modulate the output load of the PA. The DPD techniques employed in past generations cannot mitigate the impact of the cross-talk induced load modulations caused by other antennas that result in non-negligible nonlinear distortions. On top of linearity degradation, DPD is typically quite energy consuming, especially when accommodating multiple wide modulation bandwidth signals which will be the case in 5G communication.

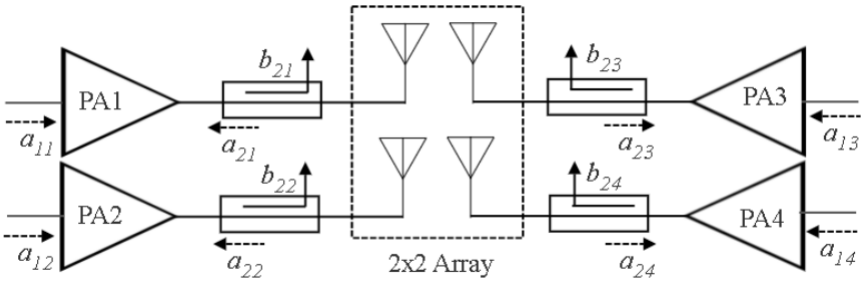

Figure 1.1: Simplified representation of a 2x2 MIMO transmitter front-end

In conclusion, 5G sub-6GHz transmitters bring massive complications in terms of design considerations given the cross-talk induced load modulation in the PAs, array arrangement decisions for optimal coupling levels, EM interference from PAs/antennas due to the compact environment, and thermal management issues which arises from limited hardware

space. To address and analyze these issues, a scalable and realistic PA-antenna array front-end hardware is required to study the overall linearity and efficiency of wide-band mMIMO transmitters.

1.2 Problem Statement

In the previous 4G BS transmitter designs, the PAs were required to have high output power and high efficiency due to the fact that the PA has the largest impact on the total efficiency of the system. The linearity of the PA can be improved with single input single output (SISO) DPD applied to each RF signal chain in 4G. Since the DPD power consumption was low compared to the PA's output power, the trade-off of PA efficiency over linearity made the entire system more efficient while offering good linearity.

The same design strategy cannot be considered for the 5G transmitter design. In 5G, due to the increased amount of RF chains in the transmitter system, each PA's output power is significantly lowered compared to that in 4G. The lowering of the PA's output power, increased number of RF chains, and higher modulation bandwidth of signals raise the DPD power consumption overhead. The trade-off of PA efficiency over linearity is no longer valid, as compensating for linearity may lead to more power lost than gained from individual PA efficiency improvements. Furthermore, with more RF chains in the transmitter system and low isolation between PA and antenna elements, linearity becomes problematic for SISO DPD to compensate due to cross-talk and load mismatch from the PA and antenna direct connections.

While there are much more complicated DPD schemes such as dual input single output (DISO) DPD [12] that include the effects of cross-talk, DISO DPD techniques will ultimately use more coefficients and in turn more power to linearize the entire system properly. Thus during transmitter design, a suitable trade-off between PA linearity and efficiency needs to be carefully examined, along with antenna array performance to ensure linearity requirements can be met while maintaining good efficiency for the entire front-end array.

This paper presents an experimental study of the effects of antenna cross-talk on the linearizability and efficiency of 5G sub-6 GHz wide-band mMIMO transmitters. The transmitter consists of 2x2 arrays of class AB PAs connected to an antenna array with reconfigurable spacing. The ability of SISO and DISO DPD techniques to linearize the PA arrays is assessed under 5G-candidate 100 MHz OFDM test signals.

1.3 Thesis Organization

The thesis is organized as follows. Chapter 2 introduces background information regarding PA linearity, efficiency, and common BS antenna architectures. This is followed by a literature review of sub-6GHz PA designs, sub-6GHz antenna array designs and MIMO transmitter measurements. The literature review will highlight past works focused on improving PA performance in MIMO settings, lowering antenna coupling in arrays, and state-of-the-art implementation of transmitter arrays.

Chapter 3 will present the design methodology of a class AB PA and modular antenna element. Electromagnetic (EM) simulations and measurements of a PA and antenna will be presented and compared.

Chapter 4 will present the array design methodologies including both antenna array analysis and front-end frame mechanical designs. This is followed by the system measurements of the transmitter front-end in both single chain and 2x2 chain configurations. Different array configurations will be tested, results analyzed, and conclusions summarized.

Chapter 5 will conclude the thesis with a summary of the findings from this work and suggestions for future work in this area.

Chapter 2

Background and literature review

In this chapter, the basic concepts of linearity and efficiency of PA will be explained in detail. General antenna architectures used in BS will be presented and compared. In the end, a literature review will be conducted for PA reduced load sensitivity techniques, antenna array de-coupling methods, and transmitter front-end performance, summarizing previous research progress.

2.1 Power amplifier linearity and efficiency

Power amplifier is one of the most important hardware in a transmitter since it largely determines the transmitter linearity and efficiency.

2.1.1 Power amplifier linearity

PA non-linearity in the forms of inter-modulation distortion (IMD) and gain compression will cause significant in-band interference and out-of-band spectrum expansion which are heavily regulated by communication standard protocols. To characterize these distortion behaviors, indicators such as AM/AM, AM/PM, 1dB output power compression point (P_{1dB}) and n-harmonic intercept points (IP_n) are essential to evaluate the linearity performance of PA design. Among these figure of merits (FoMs), AM/AM and AM/PM are the most informative and commonly used for linearity evaluation. AM/AM and AM/PM corresponds to amplitude to amplitude modulation versus input/output power and amplitude to phase modulation versus input/output power, respectively. AM/AM includes

information for P_{1dB} and from P_{1dB} initial IP_3 values can be approximated using Equation 2.1, carefully note that this approximation is not absolute, depending on different devices, the difference between P_{1dB} and IP_3 may vary between 8 and 15dB. To accurately obtain IP_3, multi-tone excitation analysis needs to be evaluated for the PA under test.

$$P_{1dB} = IP_3 - 9dB \tag{2.1}$$

The two dominating sources of AM/AM and AM/PM distortion in PA performance are the non-linearity of the trans-conductance, i.e., g_m, of the active device and intrinsic nonlinear capacitor of the device [3] corresponding to AM/AM and AM/PM respectively. For AM/AM distortion, the presence of threshold voltage for MOSFET during large signal excitation will present significant g_m non-linearity when device enters triode region from saturation region causing gain compression. Additional g_m non-linearity would also be present in the device saturation region due to the type of device used such as silicon, gallium nitride and so on. For AM/PM distortion, the presence of nonlinear capacitance of device includes the input gate capacitance C_{gs}, output drain capacitance C_{ds} and feedback capacitance between gate and drain C_{gd}. The major nonlinear capacitance contribution would be the input capacitance C_{gs} combined with the miller capacitance $C_{m_{in}}$ due to the feedback capacitance C_{gd} shown in eq.2.2, while the miller capacitance of the feedback capacitance C_{gd} shown in eq.2.3 at the output is not as significant.

$$C_{m_{in}} = C_{gd}(1 + gmR_L) \tag{2.2}$$

$$C_{m_{out}} = C_{gd}(1 + \frac{1}{gmR_L}) \tag{2.3}$$

While AM/AM and AM/PM are major linearity FOMs for PA under CW excitation, different FOMs such as normalized mean square error (NMSE) and adjacent channel power ratio (ACPR) are used for PA linearity evaluation under modulated signal excitation. NMSE measures the in-band signal deviation comparing the normalized output and input signals, while ACPR measures the out-of-band spectral regrowth of the output signal. The same NMSE and ACPR calculation can be used for transmitter system linearity evaluations.

2.1.2 Power amplifier efficiency

PA converts direct current (DC) power to RF power, empowering the input signal to be strong enough for antenna radiation for over-the-air (OTA) transmission link. There are two common indicators for PA efficiency assessment, drain efficiency (DE) and power added efficiency (PAE).

$$DE = \frac{P_{out}}{P_{DC}} \tag{2.4}$$

Drain efficiency calculation is shown in Equation 2.4, where P_{out} is the measured RF power in watts at the output of PA load, and P_{DC} is the measured DC power in watts at the drain connection. PAE is similar to DE but also accounting the effect of PA power gain. PA power gain, also known as transducer gain is defined as the power delivered to the load connected at the PA output to the power available from the source connected to the PA input.

$$G_t = \frac{P_{out}}{P_{avs}} \tag{2.5}$$

$$PAE = \frac{P_{out} - P_{in}}{P_{DC}} = DE(1 - \frac{1}{G_t}) \tag{2.6}$$

Transducer gain calculation is shown in Equation 2.5, where P_{avs} is the power available from the source in watts. The transducer gain is used in PAE calculation shown in Equation 2.6, where the gain relationship is embedded in the ratio between P_{out} output RF power and P_{in} input RF power in unit watts. Note, when the transducer gain is large, PAE approaches DE. In practice, PAE is the preferred indicator for general PA performance since it relates both the DC-RF conversion efficiency and PA power gain.

2.2 Base station antennas

BS antenna design in the past 4G has been about singular antenna performance specifications. Since 5G introduces mMIMO transmitter architecture, some of the old antenna design interests conflict with the current 5G antenna requirements. Past BS antennas aim to have high gain, high bandwidth, and good radiation performance while disregarding key mMIMO array requirements such as size, integration, scalability, and array coupling. A

general review will be carried out for different types of antenna architectures used in BS antenna design. Design considerations for the 5G mMIMO antenna array will be presented and lastly, comparisons between each general antenna topology will be carried out using the before-mentioned design considerations for the 5G antenna array.

In general, there are two major types of BS antenna topology, patch, and dipole, both extremely popular in the literature. Due to a large number of different design techniques and variations for both the patch and dipole antenna architectures, only a selected few variations will be mentioned in terms of basic theory and performance, however, a heavy analysis will not be conducted in this section.

2.2.1 Microstrip antennas

For microstrip patch operation, a transmission line model can be used for basic analysis, representing the microstrip antenna by two narrow radiating slots with dimensions of patch width and substrate height separated by a low impedance transmission line of patch length, shown in Figure 2.1. The main source of radiation is caused by the two radiation slots due to fringing effects since most electric field resides in the substrate, thus thicker substrates with low dielectric constant would bound electric field less in the substrate and provide better radiation efficiency, larger bandwidth at the expense of larger size.

Common design equations for rectangular patch antenna design would be shown below for patch width in Equation 2.7 and length in Equation 2.8 provided resonance frequency and substrate info.

$$W_p = \frac{\lambda_0}{2}\sqrt{\frac{2}{\epsilon_r + 1}} \tag{2.7}$$

where $\lambda_0 = \frac{c}{f_r}$, λ_0 is wavelength, c is speed of light and f_r is resonance frequency.

$$L_p = \frac{c}{2f_r\sqrt{\epsilon_{eff}}} - 2\Delta L \tag{2.8}$$

where ϵ_{eff} is shown in Equation 2.9 and ΔL is shown in Equation 2.10

$$\epsilon_{eff} = \frac{\epsilon_r + 1}{2} + \frac{\epsilon_r - 1}{2}\sqrt{1 + 12\frac{h}{W_p}} \tag{2.9}$$

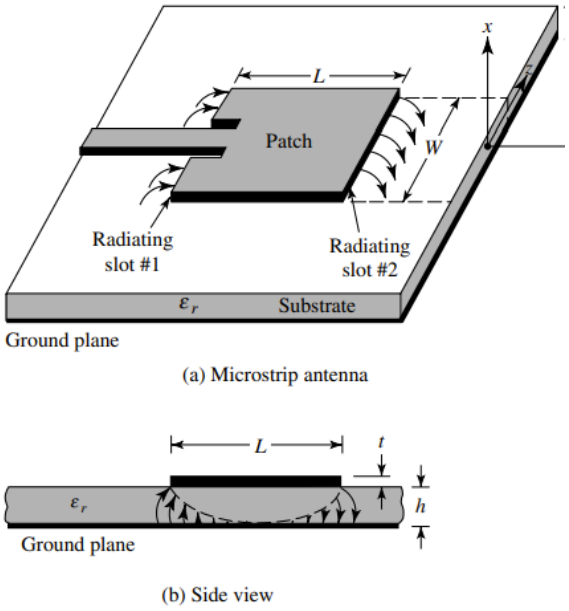

Figure 2.1: Microstrip antenna [4]

where h is the height of dielectric substrate and ϵ_r is the dielectric constant of the substrate

$$\Delta L = 0.412h\frac{(\epsilon_{eff}+0.3)(\frac{W_p}{h}+0.264)}{(\epsilon_{eff}-0.258)(\frac{W_p}{h}+0.8)} \tag{2.10}$$

Different techniques such as modified patch [18] (adding additional slots on the patch metal to create additional resonances) and stacked patch (top patch coupled to the lower patch for additional resonance) can be applied to the basic microstrip patch to enhance performance such as bandwidth. To clarify, the technique of adding slots to the patch is not limited to only bandwidth improvement but can also be applied with other purposes such as circular polarization conversion. The same can be said to stacked patch antenna, where feeding the lower patch will improve the bandwidth but feeding the top patch or both patches can achieve dual-band behavior.

2.2.2 Dipole antennas

For dipole operation, the basic half-wave dipole will be used to demonstrate basic theory since it is widely used and one of the simplest forms of a dipole antenna. Bypassing the in-depth derivation of Maxwell's equations for finite length dipole, half-wave dipole consists of two quarter-wave symmetrical conductive wires with source feeding in the middle. Due to the feeding position and length of conductive wire, current falls to zero at the end of the wire then varies sinusoidally reaching peak midway, while voltage peaks at the end of the wire then vary as cosine reaching a minimum midway. The operation frequency is determined by the length of the antenna to be half the wavelength of the resonance frequency. Figure 2.2 shows the standard radiation pattern of a half-wave dipole where the radiation is omnidirectional and nulls are located on the top and bottom of the dipole.

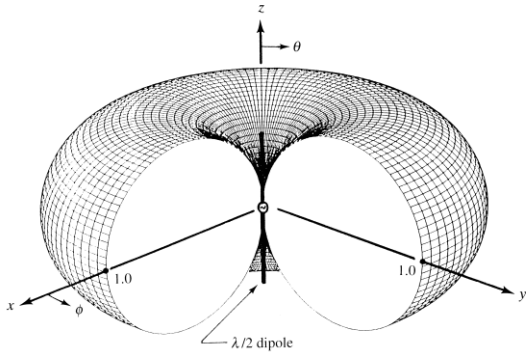

Figure 2.2: Three-dimensional pattern of a half-wave dipole [4]

One interesting variation of the dipole is the electro-magneto dipole which is rising in research popularity amongst dipole architectures in the BS antenna category. The concept of the electro-magneto dipole is first proposed on paper [23] in 2006. Electro-magneto dipole is one realization of complementary antenna which consists of an electric dipole and a magnetic dipole to achieve an equal E- and H-planes radiation patter and stable performance over frequency [23].

The basic operation of an electro-magneto dipole is shown in Figure 2.3, a planar dipole antenna Figure 2.3.a is combined with a wide-band short-circuited patch antenna as the magnetic dipole Figure 2.3.b to form the basic electro-magneto dipole antenna where the short-circuited patch is placed vertically and is connected to the planar dipole as shown in Figure 2.3.c. This particular variation of dipole antenna shows the great potential for wider bandwidth and stable radiation over bandwidth.

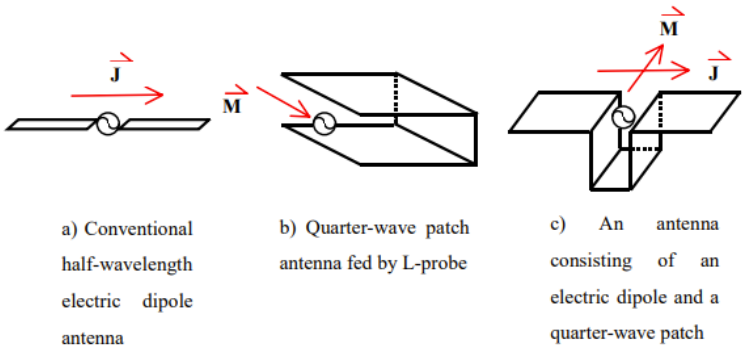

Figure 2.3: Principle of operation of an electro-magneto antenna [23]

2.2.3 5G mMIMO antenna specifications and comparison

Key antenna considerations for 5G mMIMO transmitters can be split into two general categories, electrical performance, and mechanical performance. In terms of electrical performance, criteria such as bandwidth, cross-polarization level, realized gain, directivity, stable performance across the bandwidth, dual-polarization isolation, array coupling level, and selectivity (out of band rejection) are to be considered. In terms of mechanical performance, criteria such as element size, profile height, array size, manufacture complexity, rigidity, and scalability are to be considered.

Antenna Architecture	Manufacture complexity	Design complexity	Size	Realized gain	Bandwidth	Scalability
Basic Patch	low	low	low	low	low	high
Stacked Patch	med	med	low	med	med	high
Modified Patch	med	high	low	med	med	high
Dipole	med	med	high	med	high	low
Electromagneto Dipole	high	high	high	high	high	low

Table 2.1: Comparison of antenna architectures

The Table 2.1 shows the comparison between different antenna architectures. In general, the patch antenna is smaller, easier to fabricate and scale into large arrays however suffering from lower bandwidth and realized gain comparing to a dipole antenna. While the microstrip patch antenna's bandwidth and gain can be improved with various techniques, both

the manufacturing complexity and design complexity will increase compared to the basic patch. For dipole, however, the opposite is true, dipole antenna has better performance in terms of gain and bandwidth compared to patch antenna at the expense of larger size, high manufacturing complexity, and harder to scale in an array. The electro-magneto dipole offers the highest electrical performance compared to the standard dipole but is also harder to design and harder to make as well. Thus, a balance must be reached between electrical and mechanical performances for the antenna array design in mMIMO transmitters due to practical design consideration and restrains.

2.3 Literature review

Literature reviews are conducted regarding sub-6GHz PAs with reduced load sensitivity techniques, sub-6GHz antenna designs, and array de-coupling methods, and sub-6GHz transmitter front-end system setup and performance.

2.3.1 Sub-6 GHz PAs with reduced load sensitivity

In 5G BS transmitters, PAs will be part of highly integrated active antenna arrays that support mMIMO techniques and beam steering while maintaining deployment flexibility and cost-effectiveness. The removal of the traditional lossy and bulky isolator/circulator in-between PAs and antennas is one such step toward a more effective integration [8]. The removal of isolator/circulator between PA and antenna will, first of all, introduce a mismatch between the PA output and antenna input impedance. Secondly, antenna array cross-talk during the operation of the transmitter will introduce load modulation into the PA output node. The active impedance seen by the PA will be a function of the output signal of the PA and all cross-talk signals coupled into the antenna shown in Figure 2.4.

PA performance such as efficiency, linearity, and power depends heavily on the load impedance, thus to reduce the uncertainty presented in active load modulation induced from antenna cross-talk, PA techniques to reduce load sensitivity are researched and tested in the past.

Paper [25] deploys balanced PA topology with the option of reconfiguration between balanced mode and DPA mode since balanced PA by nature of topology is proved to be insensitive to load mismatch, and DPA is proven to improve back-off efficiency. The reconfigurable balanced-to-Doherty (B2D) PA design is proposed shown in Figure 2.5, where

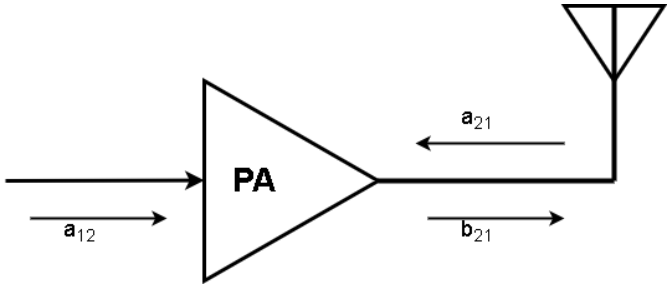

Figure 2.4: Active load impedance seen by PA connected to an antenna

the output hybrid coupler's isolation is configurable by a switch to either 50 ohms resistor (balanced mode) or ground (DPA mode).

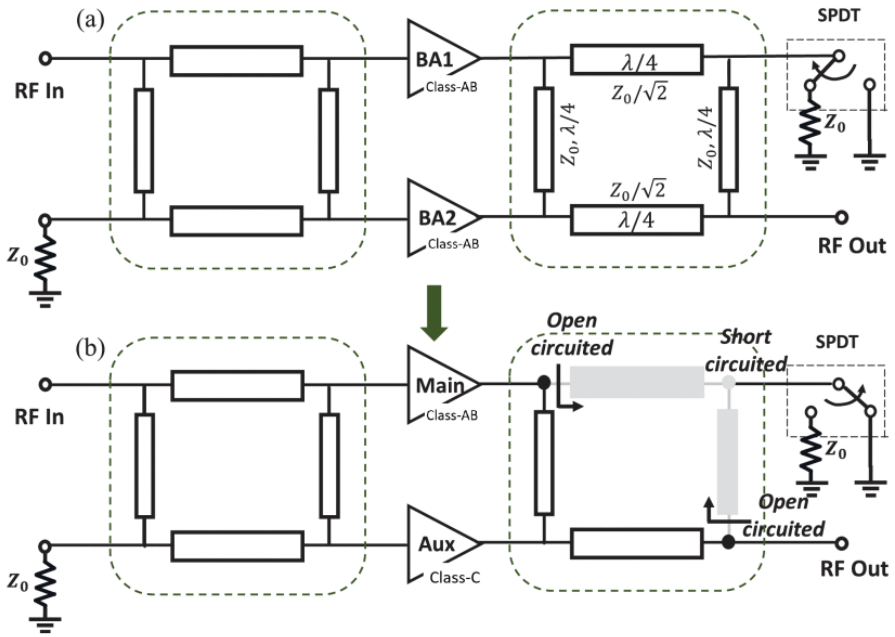

Figure 2.5: Conceptual architecture of B2D re-configurable PA [25]: (a) Balanced mode, (b) DPA mode.

B2D mode PA is designed using a GaN transistor operating at 3.5GHz in the sub-6GHz band. CW excitation measurement is conducted on fabricated PA, the DPA mode shows

a small signal (S.S.) gain of 13dB, saturated power of 42dbm, peak efficiency of 70% and 6dB BO efficiency of 55%, while the balanced mode shows an S.S. gain of 16dB, saturated power of 42dBm, peak efficiency of 68% and 6dB BO efficiency of 35%. Modulated signal testing is also conducted, with 10MHz 8.4dB peak to average power ratio (PAPR) LTE signal, the DPA mode PA presents an average efficiency of 42.4%, adjacent channel power ratio (ACPR) of -37dBc and 2.36% error vector magnitude (EVM) at maximum rated power of 34.5 dBm without DPD.

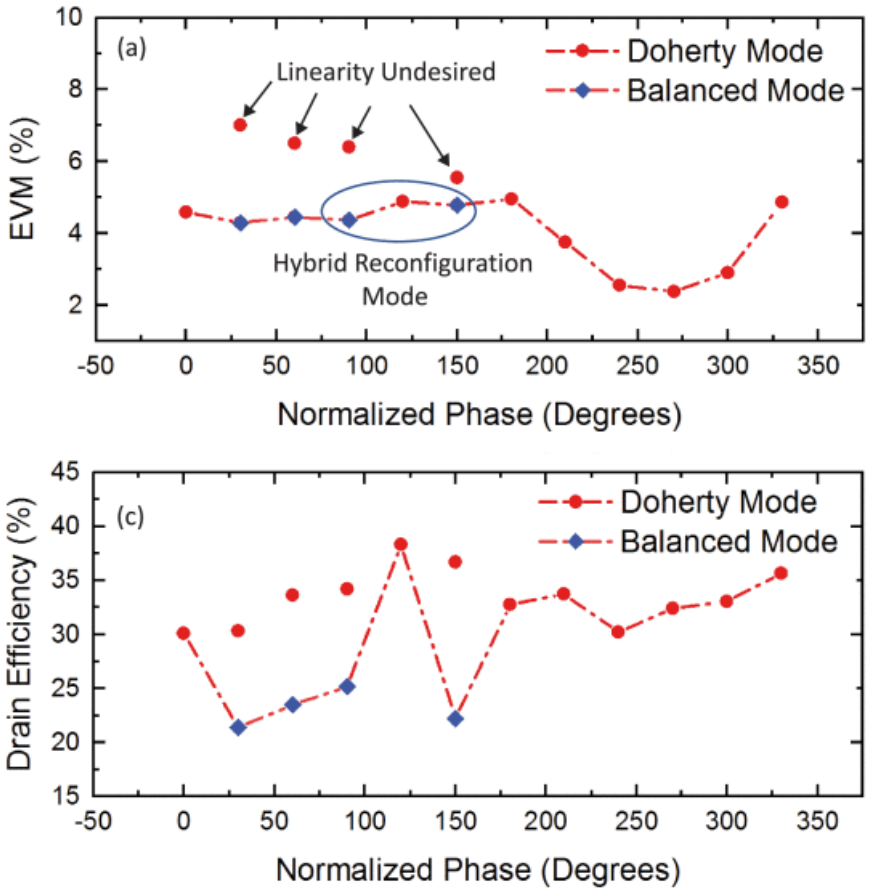

Figure 2.6: Measurement results for B2D PA under 2:1 VSWR over the entire phase range [25]: (a) EVM, (b) Average DE.

Testing of the re-configurable mode under load mismatch is conducted with PA output connected to load tuner at the output which covers 2:1 voltage standing wave ratio (VSWR)

circle on smith chart. With constant input driving the PA, the PA output is swept and balanced modes employed for load impedance which had un-satisfactory linearity for DPA mode. The measurement results for linearity and efficiency are shown in Figure2.6, linearity is maintained overall for a trade-off with efficiency.

The main advantage behind the B2D mode PA is the flexibility to use high efficient DPA when load mismatch is small and to use balanced PA when load mismatch is high. More importantly, modes can be implemented without having to physically detect the actual mismatch impedance, a superior feature over [9]. The flaw of this PA design is the lack of integration with large hybrid couplers at input and output and having additional switches (introducing losses) to change between modes, additional control circuitry, and the design complexity of combining both DPA and balanced PA as one.

2.3.2 Antenna array and de-coupling techniques

In addition to PA techniques on reducing load sensitivity, antenna array de-coupling techniques have also been explored to lower mutual coupling leading to reduced load modulation at PA output. Antenna considerations such as cost, size, profile height, mechanical rigidity, gain, selectivity, isolation, and cross-polarization are important in a 5G environment where a massive number of antennas are required to fit within a limited space and work within an EM dense environment.

Paper [7] presents a planar stacked dual-polarized patch configuration where each element consists of a 2x2 array and λxλ in area. The single antenna structure has seven layers which include feeding, ground, coupling metal strip, and patch array. Each polarization feeding is done using SMA surface-launch connectors onto the bottom of the antenna element connected to a T-junction power splitter. At the splitter end, input is guided through the ground layer bow-tie apertures, coupled to metal strips above the aperture which ultimately drives the two radiating patches by capacitive coupling at the two ends of the coupling strip overlapped by the patches. The two polarization are excited the same way with 90° rotation due to the symmetric nature of the antenna element which also improves the isolation between polarization ports. A single patch antenna element is fabricated and S.S. measured, showing 160MHz bandwidth centered at 3.7GHz and isolation between polarization ports to be -31dB within the bandwidth. The single element was also measured to have a realized gain at bore-sight to be 10.5dBi for both polarization and -25dB of cross-polarization level.

Mutual coupling studies are carried out for 1x4, 2x2, and 24x3 different array sizes where the highest mutual coupling are measured to be -32dB, -25dB, and -35dB respectively. The

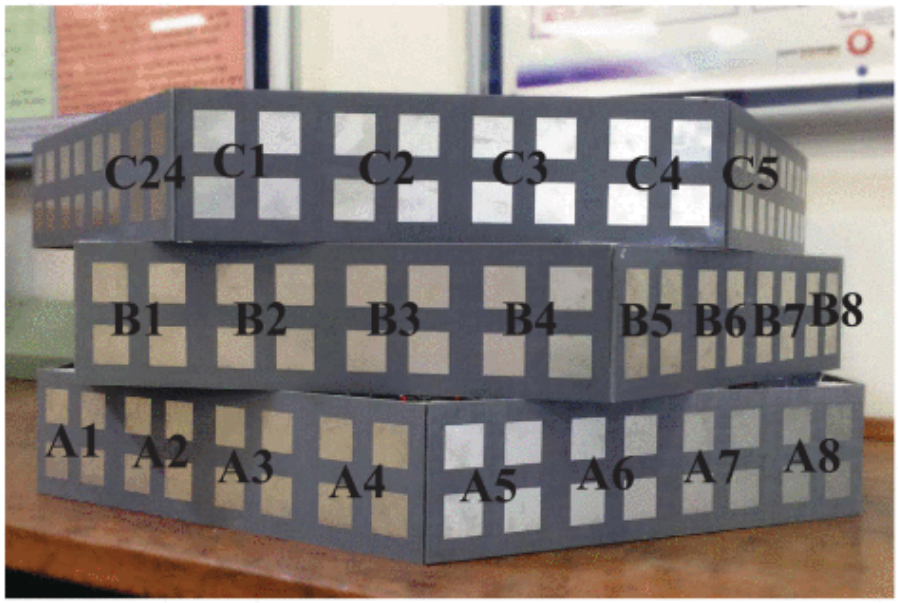

Figure 2.7: Configuration of three-level Turning Torso antenna array [7]

24x3 antenna array is shown in Figure 2.7 where individual antenna elements are indicated as C1, B1, and so on. Among the three tested arrays, the 2x2 array showed the worst mutual coupling due to the planar dimension affected by coupling from both horizontal and vertical, unlike the 1x4 and 24x3 arrays. Regardless, the mutual coupling of this array shows promising values, however, the antenna suffers low bandwidth and large single element size, difficult to integrate into a realistic sub-6GHz BS transmitter.

Paper [18] presents a dual band patch with dual polarization and filtering capability. The antenna consists of patch printed on top of upper substrate suspended in air with lower substrate below with ground and differential feeding network printed on both sides of the lower substrate. Four metal posts are vertically placed to connect the coupling patch and the feeding network. Slots are introduced on the patch to for additional resonance making the antenna dual band. The feeding network is composed of feed line with open-circuit stepped-impedance resonators (OCSIRs), transmission zeros of the feeding network can be tuned by picking the width and length of the OCSIRs, providing low transmission to the radiating patch. The OCSIRs feeding network can be seen in Figure 2.8.

The single antenna measures a -15dB bandwidth from 3.28–3.71GHz and 4.80–5.18GHz, with 37dB isolation between differential ports. For radiation measurements, the single

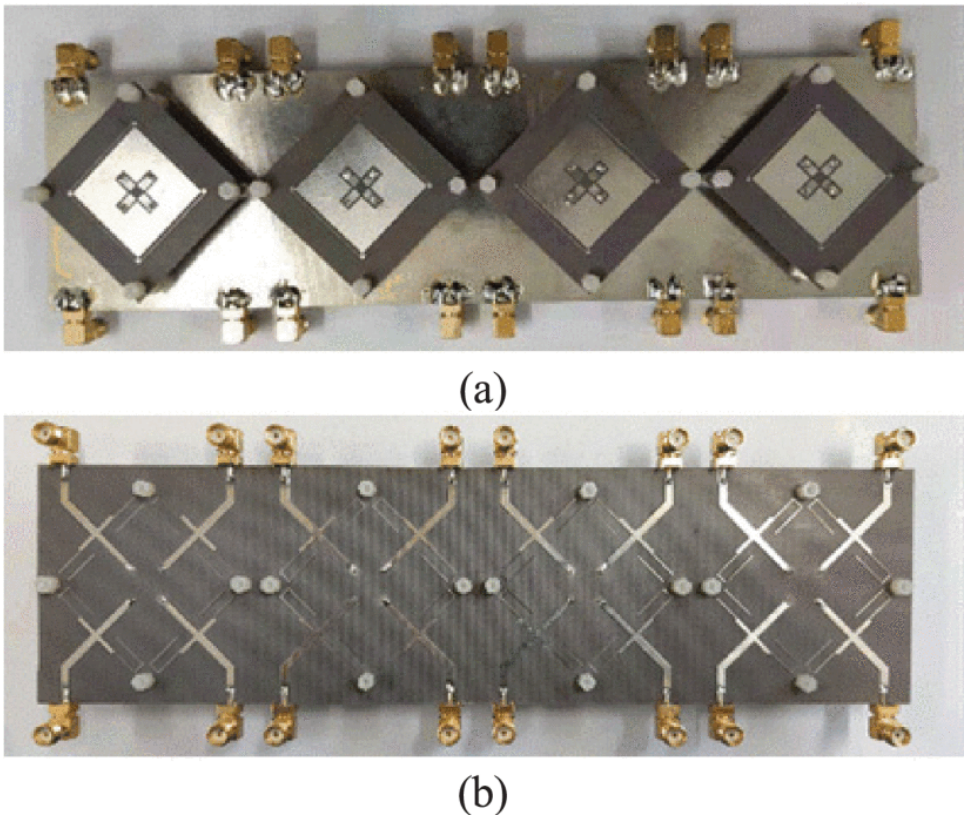

Figure 2.8: Configuration of 1x4 antenna array: (a) Top view, (b) Back view [18].

antenna has an average realized gain of 8.3dBi, cross-polarization of 30dB for both bands at boresight, and 17.5dB out-of-band gain suppression due to the two transmission zeros from the feeding network. The 1x4 antenna array is fabricated and shown in Figure 2.8, with the inter-element spacing of 0.7λ, the coupling level between elements are not presented, however, the radiation pattern of the array is measured to demonstrate beam-forming potential. The differential topology benefits the increased isolation between ports and polarization levels, however, the downside of doubling the input ports is a major challenge to integrate into a sub-6GHz nMIMO transmitter.

Lens antenna is another potential topic in 5G massive antenna systems, with gaining popularity in mmWave, the paper[17] proposes a lens antenna working in the sub-6GHz band. The paper showcases an 8x8 metasurface-based lens antenna array, where the design is separated into lens and antenna. The lens is composed of three identical metasurface metal layers separated by dielectric substrates and air layers. Different phase-shifting

elements, forming several annular zones, are incorporated to construct the metasurface layers. Each circular annular zone has the same phase shifting elements to achieve the same phase delay, the phase shift element dimensions are varied accordingly in order to focus the electromagnetic wave at a focal plane [17]. The array consists of dual-polarized prob-fed stacked patch antennas, having a -10dB bandwidth of 5.26 to 6.23GHz, isolation between polarization ports of -20dB. The single antenna radiation measurements show a realized gain of 8dBi and a cross-polarization level of 22dB at bore-sight. Within the array, the inter-element spacing is 0.8λ, which measures the worst coupling level being 25dB.

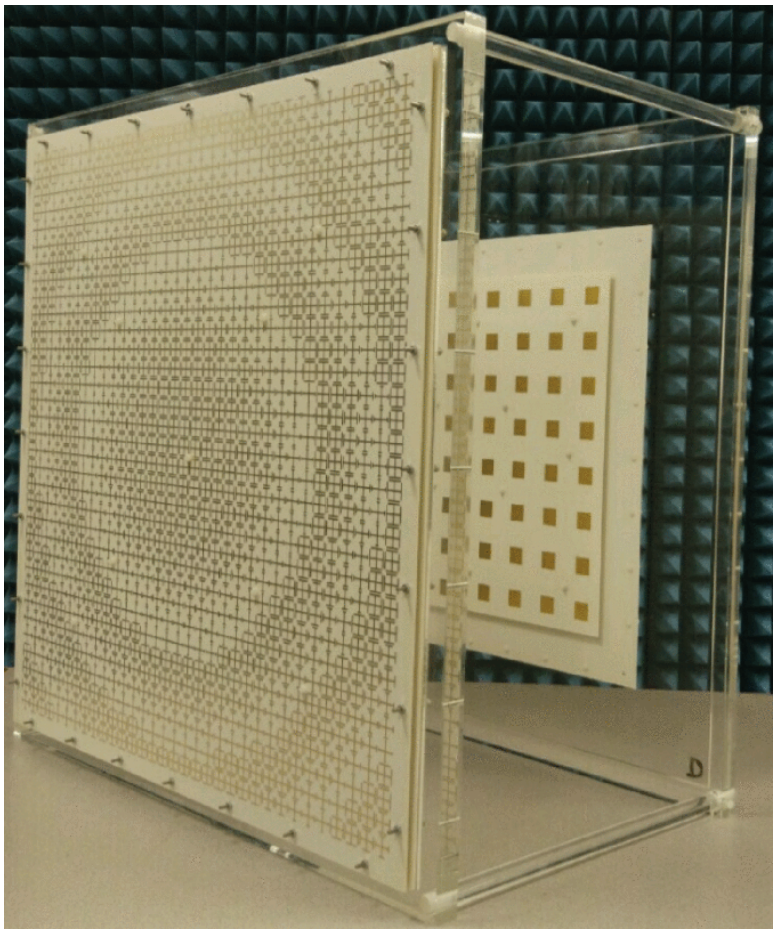

Figure 2.9: Photograph of fabricated lens antenna [17]

Combined with the lens and antennas, the array is formed shown in Figure 2.9 and tested. Switched beam-forming is employed and capable of steering the beam $\pm 50^{\circ}$ hori-

zontally and vertically providing full-dimension coverage. Compared with the other arrays, the analog and passive beam-forming capability of the lens has significantly reduced the complexity, power consumption, and boosted reliability [17]. However, issues such as size, scalability, and low isolation between polarization ports make the lens antenna solution not suitable in sub-6GHz mMIMO transmitters.

One technique to reduce antenna array coupling had been proposed in the paper [34] for mMIMO systems. The decoupling technique is general and referred to as array-antenna decoupling surface (ADS). An ADS is a thin layer of low-loss and low dielectric constant substrate printed with multiple electrical small metal reflection patches. The geometries and the dimensions of the patches are carefully designed to create a right amount of diffracted waves at the port of the coupled antenna element to cancel the coupled waves while minimizing the perturbation to the original array antenna. The separation distance (h) between the ADS and the ground plane of the array antenna is determined to ensure that the partial diffracted wave is out of phase of the coupled waves at the port of the coupled antenna element [34]. ADS can be easily applied to a 2-D array antenna, printed on a thin layer of low-loss substrate. However, a non-planar conformal ADS is also feasible with more design efforts, capable of integrating ADS with an antenna radome. A dual-polarized array can also be decoupled by making symmetric ADS patch geometries.

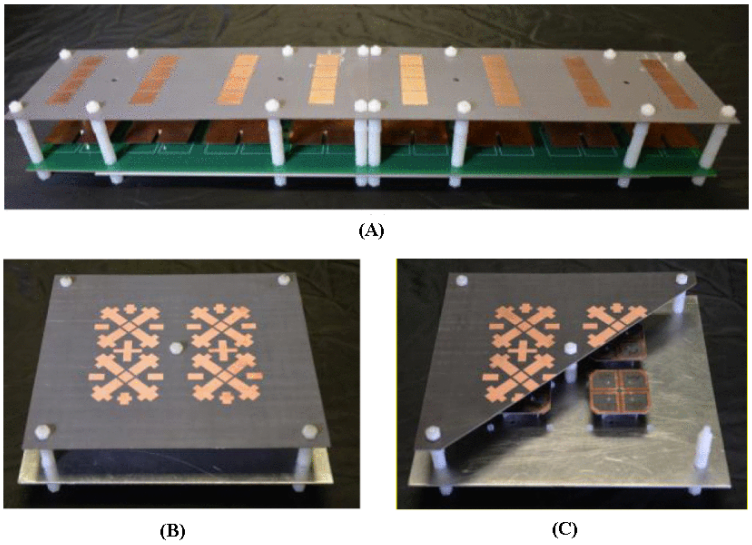

Figure 2.10: Photograph of fabricated arrays: (a) 1x8 single polarized array, (b) 2x2 single polarized array full ADS, (c) 2x2 single polarized array partial ADS [34].

Figure 2.10 shows fabricated single and dual-polarized antenna arrays with ADS. Mea-

surement study is connected for single polarized patch antenna 1x8 array at 2.45GHz and dual-polarized patch antenna 2x2 array at 3.5GHz using ADS for array decoupling. From the measurement of the 1x8 single polarized array, coupling between any two adjacent elements is significantly reduced from -15dB to below -30dB whereas coupling between nonadjacent elements maintains at the same level or is improved a little. The antenna array radiation and bandwidth are similar with and without ADS, showing ADS's limited effect on the matching and gain of antenna elements. From the measurement of the 2x2 dual-polarized array, the highest coupling is improved from -14dB without ADS to -25dB with ADS. The improvement coupling enhancement shown from ADS is significant and can be applied to any type of antenna array single or dual polarized. The downside of this method is the design complexity for dual-polarized arrays, added profile height, and mechanical rigidity of the overall structure. Although the author claims ADS can be designed with antenna radome, more simulations and studies are needed to consolidate this type of design.

2.3.3 Transmitter front-end architecture

5G MIMO transmitter system will deploy PAs with the power requirement being several orders of magnitude lower than that of the 4G PA, however, the classical problem of energy inefficiency still remains. The popular approach in 4G PA design is the use of Doherty PA (DPA) for improving back-off (BO) efficiency. The challenge with the DPA approach in mMIMO is the question of can the inherent BO efficiency benefit still be maintained under various load modulation from the active antenna array. Paper [8], Figure 2.11 shows an experiment with an 8x1 patch antenna array connected to a DPA array in the sub-6GHz Band.

The patch antenna array measures a bandwidth of 100MHz centered at 3.5GHz and a coupling level of -15dB. The asymmetric DPA designed using GaN transistor is measured to have a gain of 10dB, saturated power of 46dBm, peak efficiency of 56%, and 8dB BO efficiency of 40%. In system simulation, under the influence of 1D beam steering and mutual coupling, results show by restricting the beam steering angle and the operation bandwidth, the DPA performance benefits in BO operation over class AB and B amplifiers under an average VSWR of 4:1 induced from array beam steering less than 45°. The paper did not present any array system measurement results using modulated signals, however, the small-signal and CW measurements match with simulation. From this study, one can conclude DPA behavior can be maintained under some load modulation limits. However, the system restrictions to maintain BO benefit will become much more rigid once the scheme of digital beam-forming (varying amplitude output) is used instead of

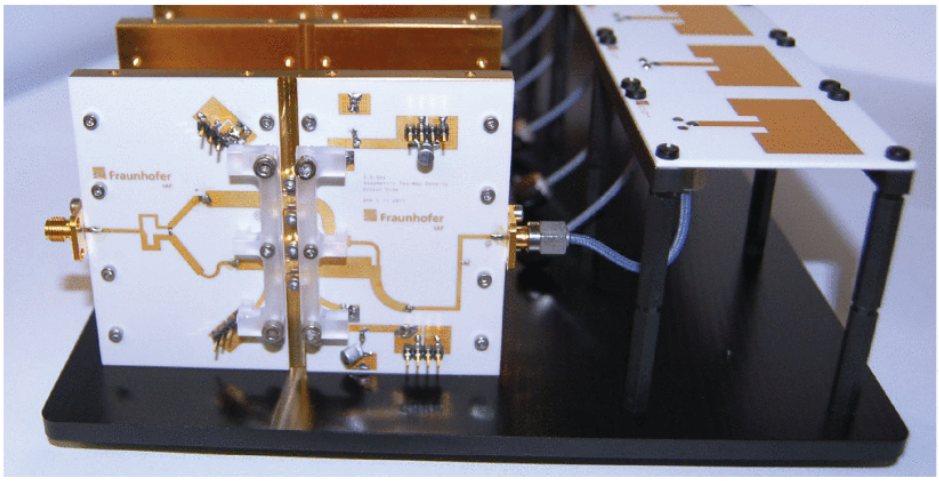

Figure 2.11: DPA connected to an 8x1 antenna array[8]

analog beam-forming (constant amplitude output) with increasing antenna array size such as 4x4 and 8x8 instead of 8x1. Further measurement studies with class AB PA and DPA in realistic MIMO setup using 5G modulated signal is needed to evaluate the benefits of different PA typologies that can bring in 5G sub-6GHz transmitter.

Multiple works in the literature have analyzed the linearity and efficiency of sub-6GHz MIMO transmitters under cross-talk effects. The paper [11] investigates cross-talk induced distortions in a 2x2 array with 8.5dB PAPR 20MHz OFDM modulated signals. The core of the paper mainly focuses on the simulation and DPD techniques employed to predict and linearize the transmitter in the presence of antenna cross-talk. The antenna array used consists of a basic inset patch with low bandwidth, single-polarization, and high coupling, while the PA used is SKY66001-11 (evaluation board) model at 2.12GHz operating in highly linear and power-inefficient modes compared to those used in a realistic deployment.

Two 2x2 antenna arrays were designed to be able to observe different coupling intensities with -12dB and -24dB. In Figure 2.12, the arrays are shown, for the array with higher coupling, the distance between antenna element centers is 0.35λ (49mm), and for the array with lower coupling, the distance is 0.5λ (70mm) at 2.14GHz resonance frequency.

Going into the measurement system setup details, four different and independent OFDM signals with 20MHz bandwidth and 8.5dB PAPR were generated in MATLAB. Two synchronized high-speed dual-channel arbitrary waveform generators synthesized the four driving signals for the PAs. The integrated couplers of the PA test boards were used to measure the individual PA output signals. The manufactured four-element antenna arrays were used

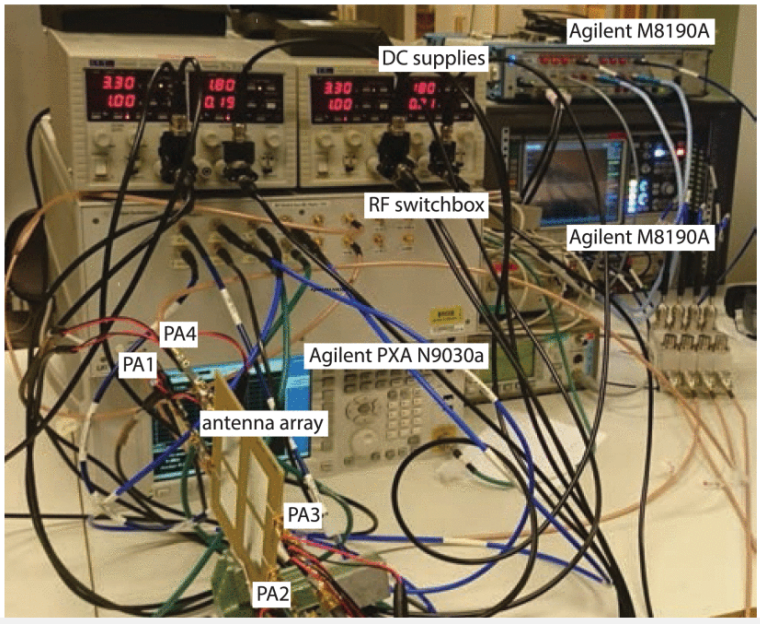

Figure 2.12: Photograph of measurement set up in the laboratory [11]

as TX arrays. The individual PA output signals were connected to an RF switch box with multiple inputs and one output, so only one signal at a time was switched through to the output of the switch box, connected to a vector signal analyzer where each signal was individually captured by the VSA. Processing was done in MATLAB [11]. The SKY66001-11 PA is modeled as dual-input PA in simulation using active load-pull measurements, the load-pull setup allows the injection of different multisine signals at the PA input and output, respectively.

The system measurement and simulation result for PA output spectra of the array is shown in Figure 2.13 with the high-coupling array results shown in Figure 2.13.a and low-coupling results shown in Figure 2.13.b. In the plots on the left, the spectra of the PA driven in a single-path scenario with and without SISO DPD are shown. In this scenario, all out-of-band distortion is due to PA non-linearity, and when SISO DPD is applied, distortions are compensated. In the plots on the right, the spectra of the PA driven in the MIMO scenario with and without SISO DPD are shown. For without DPD results in both scenarios, the difference between the distortion for the different arrays is very small, this is because the distortion due to PA is higher than the distortion due to crosstalk, thus the crosstalk distortion is masked. With the application of SISO DPD, PA distortion is eliminated and distortion due to crosstalk can be seen clearly for high and low coupling in

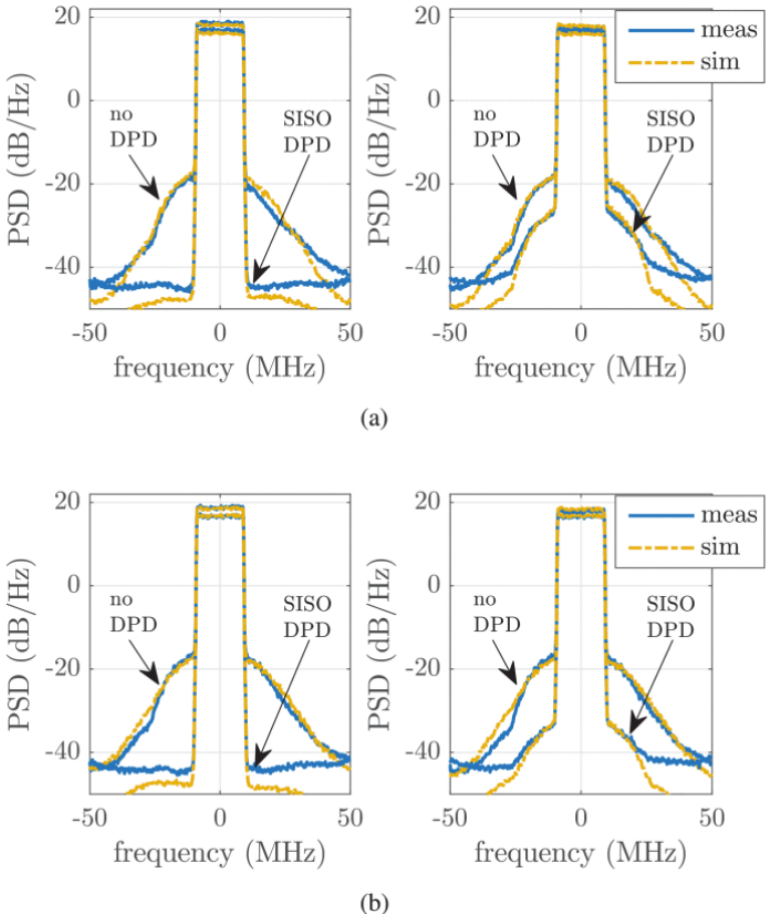

Figure 2.13: Spectra of PA1 for: (a) High-coupling array, (b) Low-coupling array. Left: PA is operated in a single-path scenario. Right: PA operated in MIMO scenario.[11]

MIMO scenarios, where the low coupling array case is visibly worse than the high coupling array case. The difference between simulation and measurement agrees well which shows the proposed technique from paper can be used to analyze the effect of crosstalk and mismatch in mMIMO transmitter environment with modulated signals.

Subsequent experiment on a 1x3 array in [24] employed PAs with higher output powers, efficiency, dual-polarized dipole 4G LTE antenna array, and over-the-air (OTA) DPD. The PAs were designed based on transistors from Freescale (MW6S004NT1), supplied with 28V. Not much information about the antenna array and PA is presented, the paper focus was on mMIMO system setup and OTA DPD with 20MHz 5.6dB PAPR OFDM modulated

signals. Both hybrid beam-forming and digital beam-forming are measured, with priority given to fully digital beam-forming since it will be the most common topology used in sub-6GHz mMIMO transmitters.

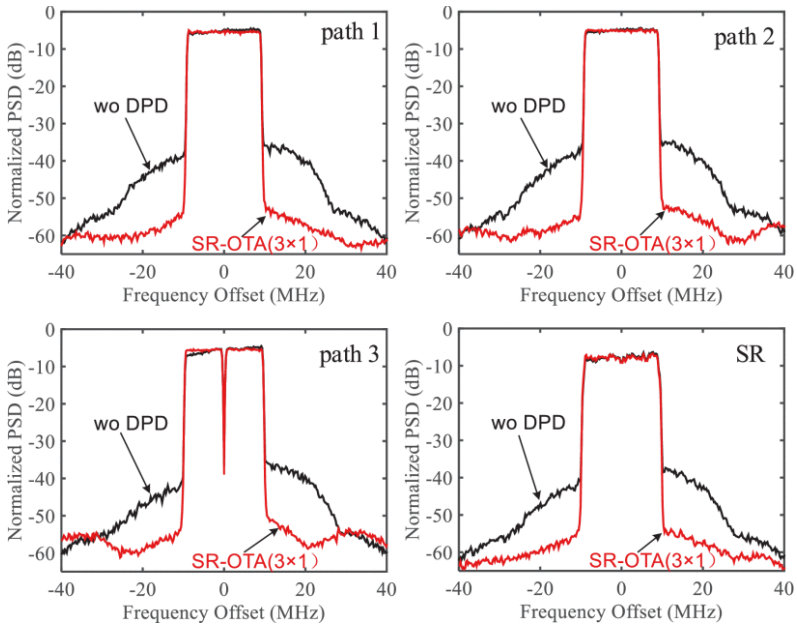

Figure 2.14: Output spectra with and without DPD [24]

The OTA measurement setup includes three transmitter paths, and each path includes a PA-antenna chain. Three uncorrelated and independent OFDM signals were generated by the software MATLAB in the computer, downloaded to vector signal generators, and then up-converted to 1.93GHz. A dual-channel vector signal generator was synchronized with a single-channel vector signal generator, and the two vector signal generators shared a local-oscillator signal. In the 3x1 scenario, the same antenna units are used in the array and share the same polarization. An oscilloscope was used to check the phase alignment of signals of three paths. After spatial propagating, three signals with nonlinear distortion were received by a standard horn antenna and then transmitted to a spectrum analyzer [24].

For the original 20MHz 5.6dB, PAPR OFDM modulated signals with no DPD applied, the adjacent channel leakage ratio (ACLR) results are around -34dB, and the normalized mean square error (NMSE) results are between -25 and -20dB. With the proposed OTA DPD applied, the ACLR results improved by around 14dB to -47dB and the NMSE results by around -18dB to -41dB. Figure 2.14 shows the normalized spectra of original signals

(without DPD), outputs of each PA output path, and output of single receiver antenna with the proposed OTA DPD in the 3x1 test. Using the proposed DISO OTA DPD, the measurement shows the transmitter can be successfully linearized using a more practical BS antenna and PA setup in the LTE band. However, the paper [24] mentioned very little about the antenna and PA design and performance, and the setup used had limited reconfigurability; thus the results gave limited insight into which performance trade-offs should be considered when designing PA and antenna arrays.

2.3.4 Discussion and analysis

There have been limited works conducted regarding the sub-6GHz PA with reduced load sensitivity, the majority of techniques employ multi-transistor PA typologies such as B2D to reduce load sensitivity. The issue with this type of approach is not only due to the increased design complexity, but also larger size, and more input controls. These problems when scaled up to a larger array will cause significant practical system concerns such as integration, cable management, and cooling. The trade-off between PA performance and transmitter system performance is unclear to justify the usage of currently available techniques for load sensitivity reduction, more circuit, and system-level studies are required.

As for BS antenna, vastly different from the PA works, major research efforts has been found in this category and vast surveys need to be conducted to differentiate the pro and con of each structure in terms of electrical and mechanical performance. The antenna literature review section includes a discussion of important works regarding different types of antenna ranging from lens antenna, patch antenna, and dipole antenna in configurations such as dual-polarized, single-fed, deferentially-fed in different array sizes from 1x4 up to 8x8. The effective de-coupling technique is also highlighted in the review, its advantages and disadvantages examined and practical implementation considered.

For sub-6GHz mMIMO transmitter architecture, this field of research is more occupied with DPD focused system implementation rather than circuit-focused system implementation. The majority of literature uses simple and irrelevant circuit elements within their system such as evaluation boards instead of PAs, basic inset-fed patch antennas instead of dual-polarized BS antennas for system testing. Important indicators such as output power, efficiency, and coupling level of the circuit elements are either missing or only partially mentioned. As mentioned before, most of these works are DPD focused, thus circuit-level performances are less interested as long as the DPD performance is shown. Thus, critical information regarding trade-offs between circuit-level designs and system specifications cannot be obtained, which calls the need for a circuit-focused system implementation of

sub-6GHz mMIMO transmitter. The highlighted works from the review however paved the way for the development of MIMO DPD techniques and transmitter system setup which will be later be deployed in this work for performance evaluation.

Chapter 3

Antenna and PA Design

3.1 Antenna design

In this section, antennas deployed in the transmitter front end will be discussed in detail. First of all, different structure designs will be carried out for deciding the suitable antenna structure to be used. Since many studies don't have complete evaluation studies and missing important electrical performance simulations/measurements, complete EM simulated designs need to be conducted to compare different structures for a satisfactory final design. Once a general structure is decided, the corresponding single-element antenna will be designed and simulated. Lastly, the design will be fabricated and measured, to confirm design specifications.

3.1.1 Design survey

Four types of general antenna structures are designed and evaluated in a full EM simulation environment, meta-surface (MTS) antenna, electro-magneto dipole antenna, stacked patch antenna, and L-probe fed antenna. Each antenna is evaluated in terms of standard performances such as bandwidth, variation within band, coupling and gain, dual-polarization performances such as isolation, and cross-polarization level, and mechanical performances such as size, integration, and rigidity.

3.1.1.1 MTS antennas

The MTS antenna is a new concept in antenna design [19][20][28]. A brief overview of meta-surface can be described as planar EM meta-material, mainly composed of sub-wavelength (element size reduced by more than one order of magnitude compared with the operating wavelength λ) scatterers and possesses unique EM property that is impossible or very hard to achieve in naturally occurring materials [32]. Some basic characteristics of MTS consist of uniform or non-uniform elements that must be sub-wavelength or deep sub-wavelength in terms of size and have the ability to achieve much more flexible EM functions such as frequency selection, polarization conversion, focusing ([17]), and so on. MTS antenna design employs characteristic model analysis (CMA) for initial element estimation and study. CMA calculates a weighted set of orthogonal current modes that can be supported on a conducting surface [10], individual modes can resonate at different frequencies and different modes can be excited simultaneously depending on the orthogonality and feed location. If multiple resonant modes with close resonance frequency can be excited together, then overall bandwidth will increase depending on how feeding is done and how many modes are excited. MTS antenna structure proposed in the paper [28] is used for survey, the paper proclaims the antenna to be low profile, broadband, high gain, simple structure, and small array size which are all desirable qualities, making it suitable for survey in comparison with other structures.

Units	L1	L2	L3	L4	L5	L6	W1	W2	W3	W4	H1	H2
mm	64.5	15	16.5	16	25.65	1.65	64.5	2.5	23.5	8	3.25	3.96

Table 3.1: MTS antenna dimensions

The overall structure and dimension of the MTS antenna design are shown in Figure 3.1 and Table 3.1. The antenna has five layers, the bottom metal is the horizontal and vertical feeding path, the feed layer and ground layer is separated by a thin substrate, where dual slots are etched onto the ground layer to perform aperture coupled feeding for each polarization. Since both polarization shares the same feed plane, to avoid overlapping of feed paths, part of the feed path for one polarization is routed through ground onto the top MTS layer and routed back to the bottom-feed layer, this technique however adds additional parasitic to one of the feed path degrading the port's matching. The MTS layer and ground layer are separated by a thick substrate and MTS elements are printed in four-by-four square patch sub-arrays. The simulation results shown in Figure 3.2 displays the -10dB bandwidth for both polarization to be 3.2 to 4.3GHz, realized gain to be 8dBi at

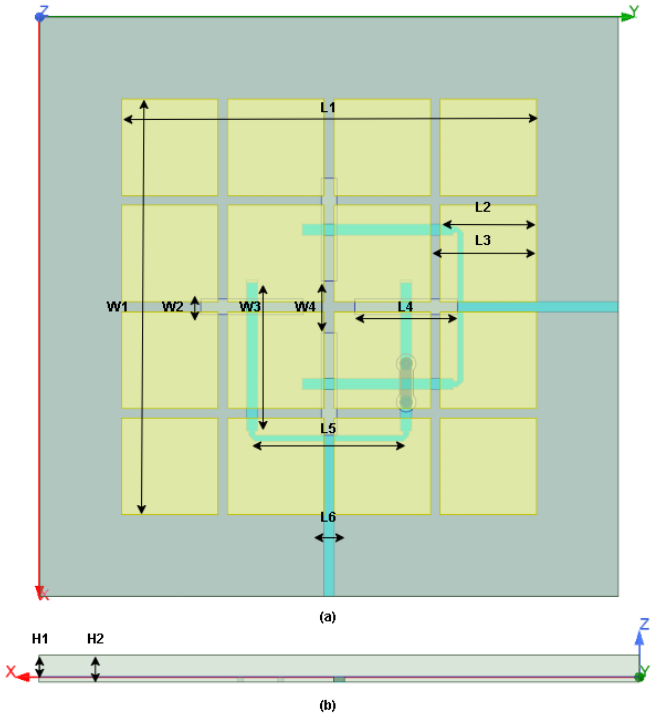

Figure 3.1: MTS antenna layout: (a) Top view, (b) Right view.

3.5GHz, isolation between polarization ports to be -22dB maximum, and cross-polarization at bore-sight to be -33dB.

An MTS antenna array is designed differently from the traditional planar arrays, MTS elements are shared between each antenna making the overall array size smaller and more compact. The array arrangement is shown in Figure 3.3, the highest coupling between elements is simulated to be -11dB. While MTS antenna offers good electrical performance, a major concern is raised from mechanical requirements. Due to the nature of being able to share MTS between adjacent elements, this makes the MTS antenna array unable to be modular and limits scalability and integration for testing. The high coupling for one polarization will also cause issues when performing fully digital beam-forming for mMIMO transmitter operations.

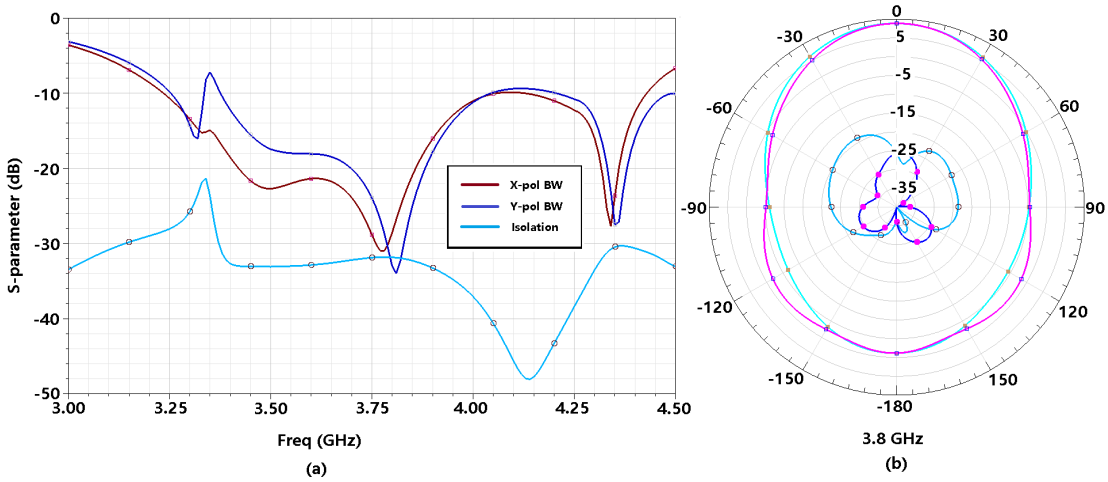

Figure 3.2: MTS antenna simulation results: (a) Simulated return loss for both polarization ports (red/blue/box) and isolation between ports (cyan/circle), (b) Co-polarization at 3.5GHz (cyan/purple/box) and cross-polarization at 3.5GHz (dark/light blue/circle).

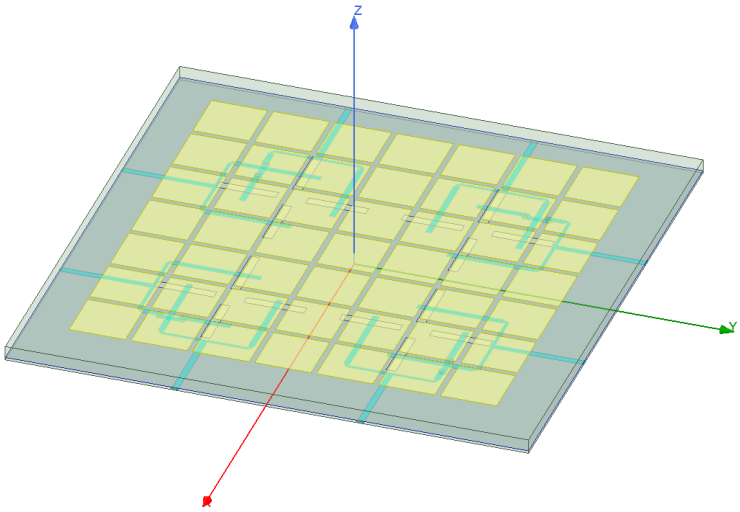

Figure 3.3: MTS antenna 2x2 array

3.1.1.2 Electro-magneto dipole antennas

The electro-magneto dipole antenna is also a young concept in antenna design, the basic theory and origin are discussed in the chapter background, section BS antenna thus this

sub-section will only talk about the implementation structure and simulation results for a dual-polarization EM dipole antenna. The EM dipole antenna structure proposed in the paper [30] is used for survey, the paper proclaims the antenna to be broadband, high gain with stable radiation pattern, EM dipole is known to have excellent electrical performance, making it suitable for survey in comparison with other structures.

The overall structure and dimension of the EM dipole antenna design are shown in Figure 3.4 and Table 3.2. The EM dipole antenna is a 3D structure instead of planar, composed of a horizontal crossed dipole, a vertically shorted patch, two Γ-shaped feeding paths, and a square ground reflector, similar to the traditional EM dipole structure, this particular variation is adjusted for dual-polarization while providing decent isolation between both dual-polarization ports. To realize dual-polarization configuration, both the magnetic dipole and electric dipole are cut away along the horizontal symmetry plane with a gap width of W3 as shown in Figure 3.4.a, the two polarization ports are rotated by 90° due to the symmetry of the overall structure [30]. The two Γ-shaped feeding paths are overlapped in the center of the antenna, thus to provide isolation, one path is curved upwards while the other path is curved downwards, suitable curve length is determined to provide the best trade-off between bandwidth and isolation. One interesting remark this particular EM dipole demonstrates is the fishtail-shaped patches, which control the E-plane and H-plane radiation pattern to achieve the desirable half power beam widths (HPBWs). The fishtail-shaped patches result from the combined symmetric geometry of using trapezoid shapes for both electric dipole and magnetic dipole instead of the traditional square/rectangle. It is been studied in the paper [30], by using trapezoid shapes and varying the additional length extension of sides, HPBW in E-plane will increase/decrease accordingly with the additional length, the opposite is true for H-plane HPBW, thus by tuning the trapezoid shapes symmetric HPBW can be achieved for both E-plane and H-plane.

Units	L1	L2	L3	L4	W1	W2	W3	W4	W5	H1	H2	H3
mm	65	17	18	18	65	4	11.5	17	5	21	18.5	12.5

Table 3.2: EM dipole antenna dimensions

The simulation results shown in Figure 3.5 displays the -10dB bandwidth for both polarization to be 3.2 to 4.2GHz, realized gain to be 10dBi at 3.8GHz, isolation between polarization ports to be -22dB maximum, and cross-polarization at bore-sight to be -25dB. The EM dipole array is initially designed at 0.75λ spacing due to the larger size of the EM dipole single element. The highest coupling between elements is simulated to be -14dB. The

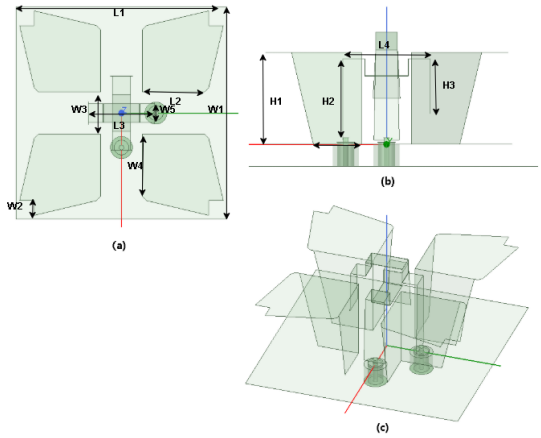

Figure 3.4: EM dipole antenna layout: (a) Top view, (b) Right view, (c) Trimetric view.

EM dipole antenna offers the most electrical performance among other types of antenna such as MTS and patch, however, due to the 3D structure of the antenna, the rigidity and fabrication complexity will be an issue to arrange such an array in an mMIMO fashion. The fairly large element size and high coupling level will also be problematic during the operation of a fully digital beam-forming transmission.

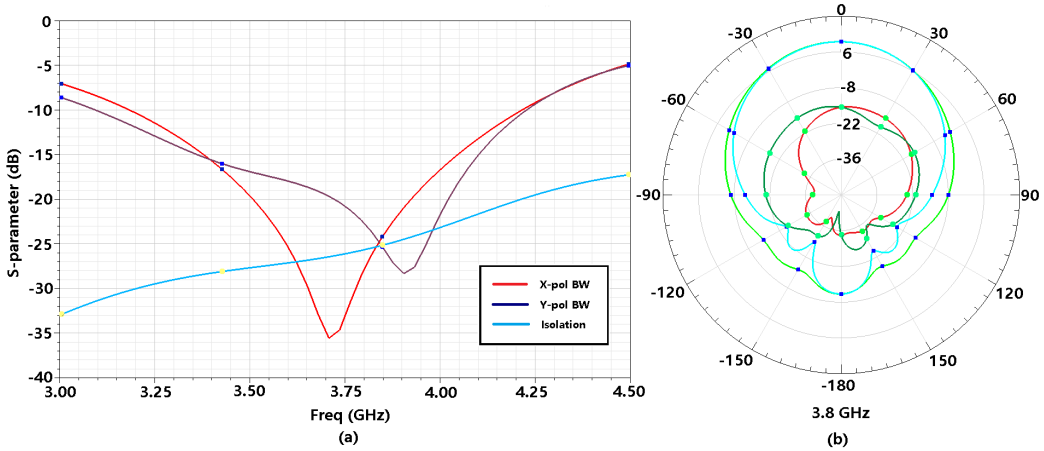

Figure 3.5: EM dipole antenna simulation results: (a) Simulated return loss for both polarization ports (red/brown/box) and isolation between ports (cyan/circle), (b) Co-polarization at 3.8GHz (cyan/green/box) and cross-polarization at 3.8GHz (emerald/red/circle).

3.1.1.3 Stacked patch antennas

The patch antenna is also a very popular concept in antenna design due to the ease of fabrication and easy structure, the basic theory of microstrip patch is discussed in chapter background, section BS antenna thus this subsection will expand upon the stacked patch technique to extend bandwidth, implementation of dual-polarization and simulation results for stacked patch antenna. There is a limit of how much impedance bandwidth a basic patch antenna can achieve and several methods have been attempted to improve the intrinsic narrow bandwidth. Out of all the bandwidth enhancement techniques, one effective method is to add a second patch on top of the main patch creating the stacked patch microstrip antenna structure. In general stacked configuration, there are two resonators, the main driven patch and the parasitic coupled patch. Depending on the substrate property for top and bottom layers and the required resonance frequency, the dimensions of the patches can be determined appropriately. Combined together with mutual coupling between both patches, the two resonance frequencies will be shifted with respect to each other producing an overall resonance and increased bandwidth. Proper coupling between the two resonators can be adjusted by the substrate's thickness and material property. The stacked patch antenna structure proposed in the paper [37] is used for the survey, the paper is a previous work within the group and has produced good results between antenna measurement and simulation. Adjustments are made to the original structure in order to integrate dual-polarization making the design more suitable for comparison with other structures.

The overall structure and dimension of the stacked patch antenna design are shown in Figure 3.6 and Table 3.3. The stacked patch antenna is a planar structure consisting of six layers, the bottom substrate separates the bottom ground layer and top driven patch layer, where circles are etched onto the ground layer to avoid shorting the probe-feeding vias. The parasitic patch is on the top layer of the top substrate where the top substrate is separated from the bottom substrate by an air layer. To implement dual-polarization, both patches are squares for symmetry, and the two polarization ports are rotated by 90° probe fed from two sides of the main driven patch.

Units	L1	L2	L3	W1	W2	W3	W4	H1	H2	H3	H4
mm	60	21.5	3	60	5	20.5	13.25	10.8	3.15	4.5	3.15

Table 3.3: Stacked patch antenna dimensions

The simulation results shown in Figure 3.7 displays the -10dB bandwidth for both polarization to be 3.2 to 3.9GHz, realized gain to be 7.2dBi at 3.5GHz, isolation between

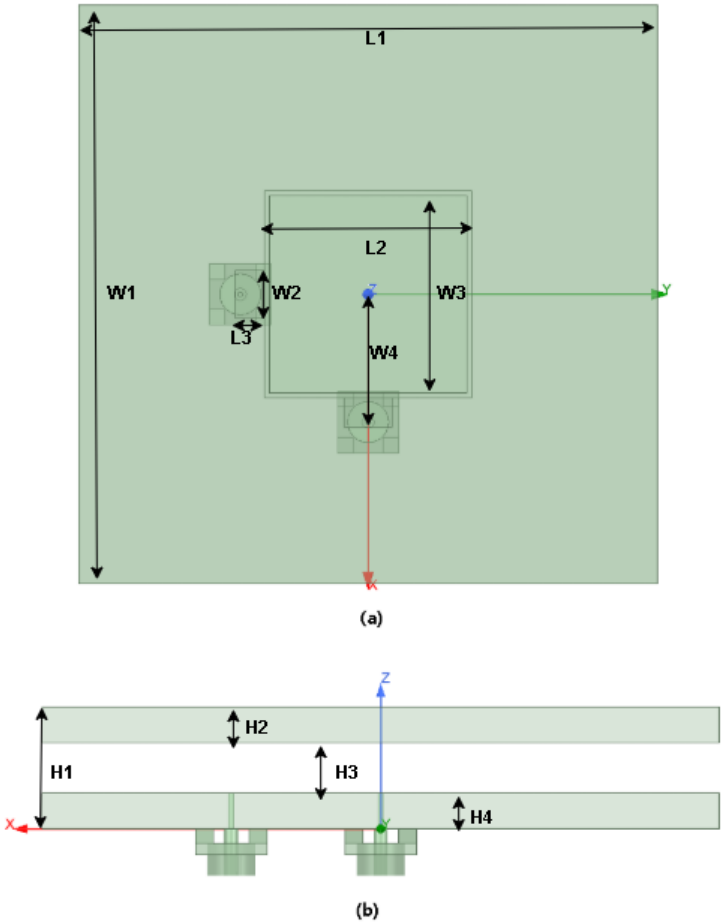

Figure 3.6: Stacked patch antenna layout: (a) Top view, (b) Right view.

polarization ports to be -18dB maximum, and cross-polarization at bore-sight to be -18dB as well. The stacked patch array is initially designed at 0.5λ spacing and the highest coupling between elements is simulated to be -18dB. The stacked patch antenna offers the least electrical performance in terms of bandwidth and gain, however, due to the planar structure and simple design, the rigidity, fabrication complexity and cost will make this type of array easy to realize in an mMIMO fashion. The high modularity of patch antenna also makes testing arrays much more flexible due to their small size and high integration. The array coupling level is also observed to be the highest amongst other structures due to the directional nature of the radiation pattern, making the array more desirable during

the operation of a fully digital beam-forming transmission.

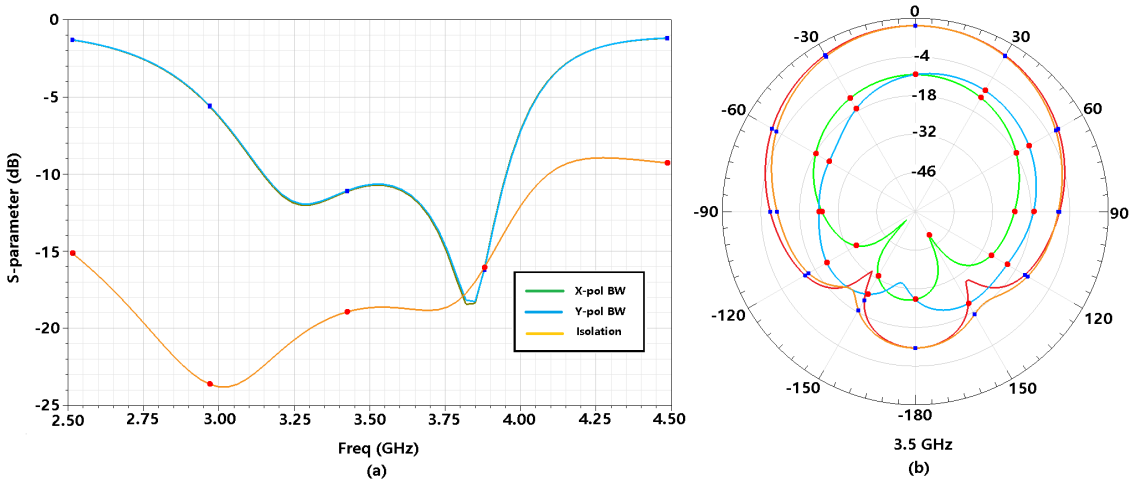

Figure 3.7: Stacked patch antenna simulation results: (a) Simulated return loss for both polarization ports (blue/green/box) and isolation between ports (orange/circle), (b) Co-polarization at 3.5GHz (red/orange/box) and cross-polarization at 3.5GHz (green/blue/circle).

3.1.1.4 L-probe fed patch antennas

L-probe feeding technique for patch antenna is first introduced in 1998 in the paper [16], it demonstrated good electrical performance with bandwidth up to 28% however lacks good cross-polarization in radiation. The enhanced bandwidth compared with the traditional probe comes from the unique structure of the L-probe. The vertical portion of the L-shaped probe forms an open circuit stub of length less than a quarter of the wavelength with the patch (capacitive) and together with the inductance of the horizontal portion of the L-probe, the stub acts as a series-resonant element with a resonant frequency close to that of the TM_{01}, mode of the patch [16]. Whereas, for the conventional probe, only an inductor is included in the equivalent circuit which deteriorates the bandwidth performance of the microstrip patch antenna. More variations of L-probe feeding have also been introduced as research progressed, such as dual-polarized L-probe [33], the M-probe [26], the anti-symmetric L-probe[27] and the double torsion coil feed [38].

A comprehensive design study has been conducted for the possibility of different types of probe-fed patch antennas. The structures, dimensions, and performances are shown in

Figure 3.8 and Table 3.4.

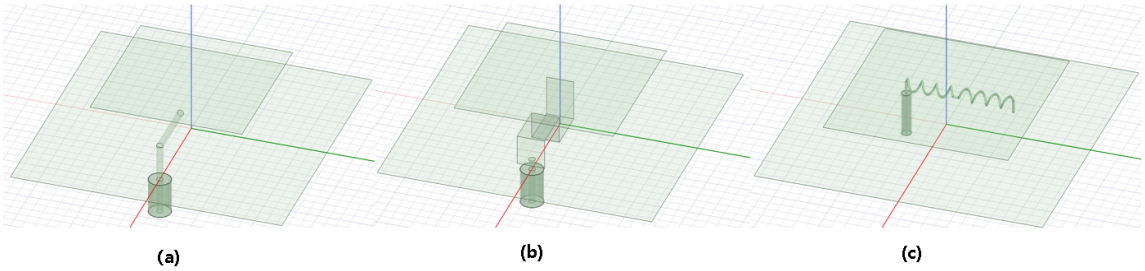

Figure 3.8: Probe fed patch survey: (a) Basic L-probe, (b) Basic M-probe, (c) Basic torsion coil.

Probe antenna	Patch size (mm)	Height (mm)	Bandwidth (GHz)	Gain (dB)	Cross-pol (dB)
L-probe	28x28	10	3.2 - 4.7	6.5 - 7.2	15
M-probe	29x29	9.0	3.2 - 4.1	6.3 - 6.5	22
Torsion coil	32x32	5.8	3.4 - 4.1	7.4 - 8.0	20

Table 3.4: Comparison of probe antennas

As seen from the study, different types of probe feeding techniques offer similar performances and similar sizes. The torsion coil offering slightly higher performance than the L-probe and M-probe but a much more complex feeding structure. The L-probe feeding technique is best in consideration due to its high bandwidth, decent performance, and simple structure, however, a solution must be found to improve cross-polarization of the radiation patterns. One simple yet effective technique to reduce cross-polarization for an L-probe fed patch antenna is proposed in the paper [13]. The paper claims that since the main source of cross-polarization comes from the vertical portion of the L-probe, an opposite current patch in contrast to the vertical feeding probe can counter-act the cross-polarization radiation field. The concept is clearly demonstrated in Figure 3.9 where a wire is placed in front of the feeding probe and the induced current from the vertical feeding probe's radiation will be opposite in phase.

The technique is adopted in a standard L-fed probe and a dual-polarized design is created and simulated in full EM. The overall structure and dimension of the L-probe fed patch antenna are shown in Figure 3.10 and Table 3.5. The L probe antenna consists of patch metal, spacers, isolation wall, and two dual-polarization L-feed probes. The structure

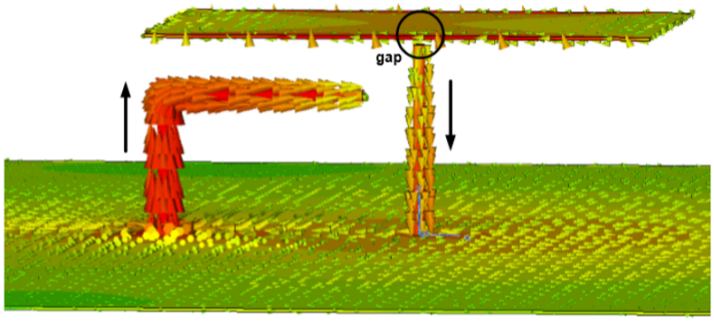

Figure 3.9: Surface current density on improved structure [13]

is simple however not as rigid as a planar antenna, the isolation wall provides both improved isolations between two polarization ports and cross-polarization in radiation pattern due to opposite induced current. The structure is symmetric to implement dual-polarization, and the two polarization ports are rotated by 90° L-probe fed from under the main patch.

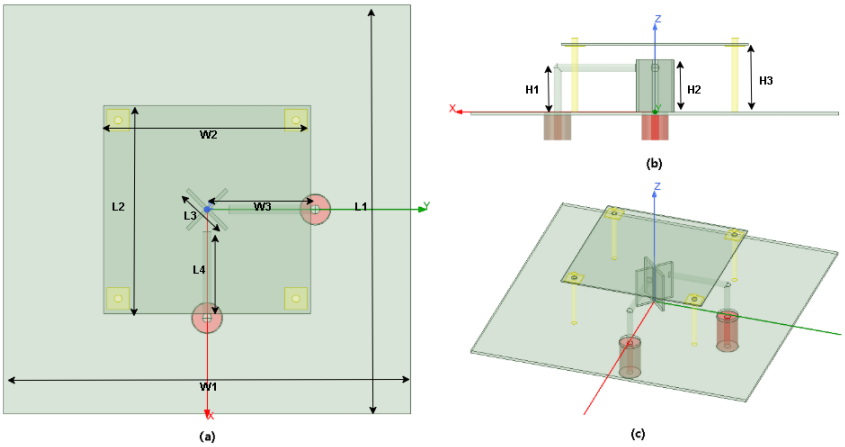

Figure 3.10: L-probe patch antenna structure: (a) Top view, (b) Right view, (c) Trimetric view.

The simulation results shown in Figure 3.11 displayed the -15dB bandwidth for both polarization to be 3.3-4.2GHz, realized gain to be 7.3dBi at 3.5GHz, and 6.7-7.3dBi across the entire bandwidth. The isolation between polarization ports is -22dB and cross-polarization at bore-sight is 26dB, significantly improved from the 15dB in the previous design. The array is also designed at 0.5λ spacing and the highest coupling between elements is simulated

Units	L1	L2	L3	L4	W1	W2	W3	H1	H2	H3
mm	60	21.5	3	60	5	20.5	13.25	10.8	3.15	4.5

Table 3.5: L-probe patch antenna dimensions

to be -15dB. The L-probe fed patch exhibits low profile height up to 0.1λ, high bandwidth, decent gain, good cross-polarization, and decent isolation. The modularity of the L-probe patch is high and compact, however, due to the substrate being air, the overall mechanical strength is not as good as patch antennas with solid substrates, and array coupling also leaves much to be desired in mMIMO operation settings.

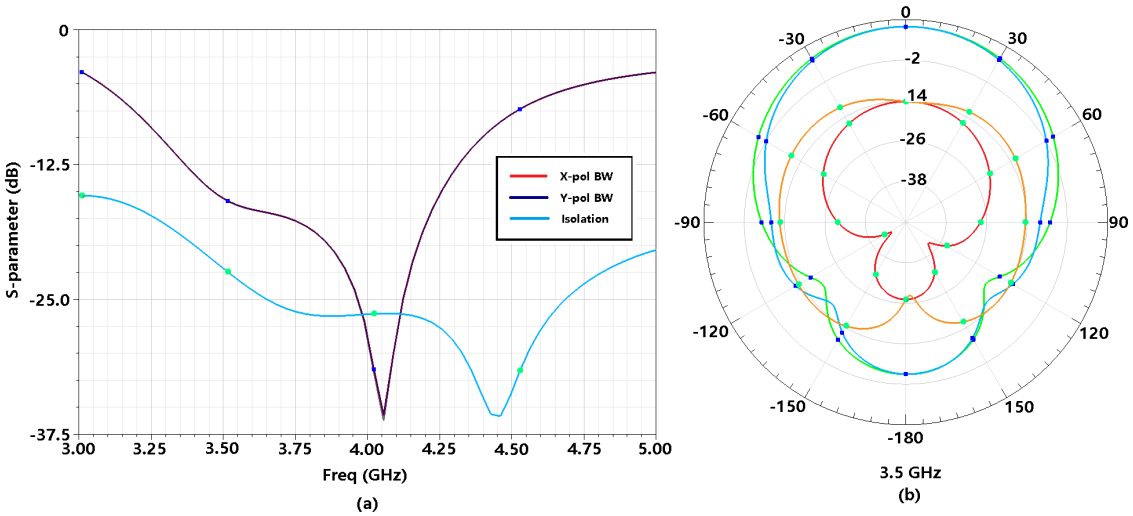

Figure 3.11: L-probe patch antenna simulation results: (a) Simulated return loss for both polarization ports (black/box) and isolation between ports (blue/circle), (b) Co-polarization at 3.5GHz (blue/green/box) and cross-polarization at 3.5GHz (red/orange/circle).

3.1.1.5 Design survey comparison and summary

The design survey consists of four architectures, MTS antenna, EM dipole antenna, L-probe antenna and stacked patch antenna, all have their own advantages and disadvantages. Factors of both electrical and mechanical performances such as bandwidth, gain,

isolation, cross-polarization, maximum array coupling, element volume, and integration will be considered in the comparison table.

Antenna Design	Bandwidth (GHz)	Gain (dBi)	isolation (dB)	Coupling (dB)	Volume (mm)	integration
MTS Antenna	3.2-4.3	8	-22	-11	64^2x4	med
EM Dipole	3.2-4.2	10	-22	-14	65^2x21	low
Stacked Patch	3.2-3.9	7.2	-18	-18	60^2x11	high
L-probe	3.3-4.2	7.3	-22	-15	60^2x11	med-low

Table 3.6: Comparison of antenna architectures

The Table 3.6 shows the comparison between different antenna designs. In general, EM dipole offers the best electrical performance in terms of bandwidth, gain, and isolation, followed by MTS antenna and stacked patch, although the difference in performances is not huge. The issue EM dipole brings is a large size and complex structure which makes the antenna harder to integrate into large volumes and mechanically delicate. This is a huge drawback in the context of building an mMIMO transmitter test-bench, practices such as handling, moving, and rotating the test-bench are often performed, and breaking the antennas will cause huge issues during testing. A more rigid structure such as planar is more preferred in a testing environment. MTS antenna offers the second-best in terms of electrical performance, high array integration, and low profile height, however, it suffers from high coupling level issues and low modularity due to shared MTS cells in an array configuration. Compared to the stacked patch which has the lowest electrical performance but excellent mechanical properties, high modularity, and low array coupling. Between MTS antenna and stacked patch antenna, the stacked patch is preferable due to its better performance in array setup. Although MTS antenna offers better single antenna performance compared to stacked patch, however the end goal of this work is to build an mMIMO transmitter front-end that will operate multiple RF chains simultaneously instead of a single RF chain and the better coupling level, high modularity and integration will benefit the transmitter system much more rather than trading array performance for single element performance. A difficult decision is made between L-probe fed antenna and stacked patch antenna, overall the L-probe fed antenna has good electrical performance with wide bandwidth, high gain, decent isolation, and good cross-polarization level. The array coupling is an issue but much improved compared to the MTS antenna and EM dipole antenna. The mechanical aspect of the L-probe patch is not the most convincing compared to the stacked patch, mostly because the L-probe patch is suspended in the air so there is not much stable structural support for the entire antenna. Compared to the

stacked patch which is solid and planar, undeniably the best option in terms of mechanical performance. In the end, the stacked patch is picked as the main antenna structure simply because of its excellent mechanical property and satisfactory electrical property. There is a lot of research in patch antenna designs and finding a technique for the patch antenna to improve the isolation and cross-polarization performance will be optimal.

3.1.2 Aperture/proximity coupled feeding technique

The feeding technique employed for stacked patch design in the previous section is probe-fed, one of the most commonly used techniques for feeding stacked antenna, a feeding probe is inserted between the ground layer and radiation patch to achieve mode excitation. The location of the feeding probe is critical since it affects the matching between the SMA input connector and the main driven patch, impacting bandwidth, radiation pattern, and gain of the antenna. The common fundamental mode of the patch can be typically excited by putting the feed location in the center of the patch's width direction (y-axis) where the length direction (x-axis) will determine the impedance seen by the feeding probe. From the general voltage and current profile described in the background chapter, BS antenna section, the probe will experience the highest impedance when fed at the edge of the patch and least impedance when fed at the center of the patch, thus an appropriate matching point can be found somewhere between. From the design survey in the previous section, the problem of probe-fed technique becomes clear, the lack of isolation between both polarization ports is a major problem and different feeding technique is required to achieve better isolation and cross-polarization level.

Aperture coupled feeding technique is a popular feeding method for patch antenna first proposed in the paper [29]. One of the earlier works for dual-polarized stacked patch antenna with aperture coupled feeding is presented on paper [31]. The input RF signal is coupled from the micro-strip feed line through the slot in the ground plane to the main driven patch, which is capacitively coupled to the parasitic patch above for wider bandwidth. To generate dual linear polarization, two input feeding microstrip line is made along with a cross-shaped slot in the ground plane. The issue of this type of feeding results in overlapping of the path between the different input paths, thus additional complexity such as air bridge or via-bridge-via needs to be implemented for one path, and imbalance will occur between the two input branches. The results of this technique are presented with a bandwidth of 23% and isolation of more than 27dB between both polarization ports over bandwidth with a good cross-polarization level[31]. The high isolation is a major improvement over the probe-fed dual-polarized antenna, however, a cleaner solution is

needed for overlap since the air bridge solution demonstrated in the paper is not suitable for this work in terms of mechanical performance.

Paper [21] presents an alternative solution to dual-polarized patch antenna, where the feed networks consist of an upper layer and lower layer separated by the ground plane. The input path on the lower layer under the ground plane uses aperture coupled feeding while the input path on the upper layer above the ground plane uses proximity coupled feeding. The measurement results of this technique implemented in a single path antenna structure show a -10dB bandwidth of 3.3-3.8 GHz, isolation of more than 50dB across the bandwidth, and cross-polarization of -38dB at bore-sight. The improvement of isolation is huge due to the dual-polarized feeding ports are located on different substrates.

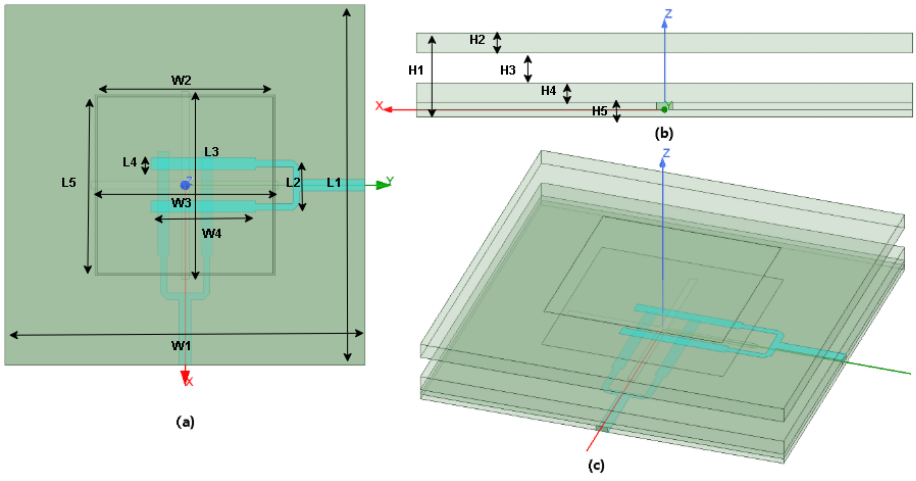

Figure 3.12: Stacked patch structure: (a) Top view, (b) Right view, (c) Trimetric view.

Combing techniques from paper [31] and [21], an dual-polarized aperture/proximity coupled stacked patch antenna is designed and simulated. The overall structure and dimension of stacked patch antenna is shown in Figure 3.12 and Table 3.7. W2 represents the parasitic square patch length, L5 is the driven square patch length and W3 is the cross-shaped slot length etched in the ground. The stacked patch antenna consists of a parasitic patch layer, driven patch layer, proximity coupled feeding layer, ground layer, and aperture coupled feeding layer. Both the proximity coupled feed path and aperture coupled feed paths use balanced feeding topology, where the input RF microstrip line is power divided and split into two symmetric branches to coupled through the ground cross-shaped slot.

The simulation results in Figure 3.13 shows the -10dB bandwidth for both polarization ports to be 3.3-3.9GHz, realized gain to be 6.5dBi at 3.5GHz, and 6.2-7dBi across the en-

Units	L1	L2	L3	L4	L5	W1	W2	W3	W4	H1	H2	H3	H4	H5
mm	50	6.9	26	1.6	25	50	24.5	26	14.5	8.43	2	3	2	0.713

Table 3.7: Stacked patch antenna dimensions

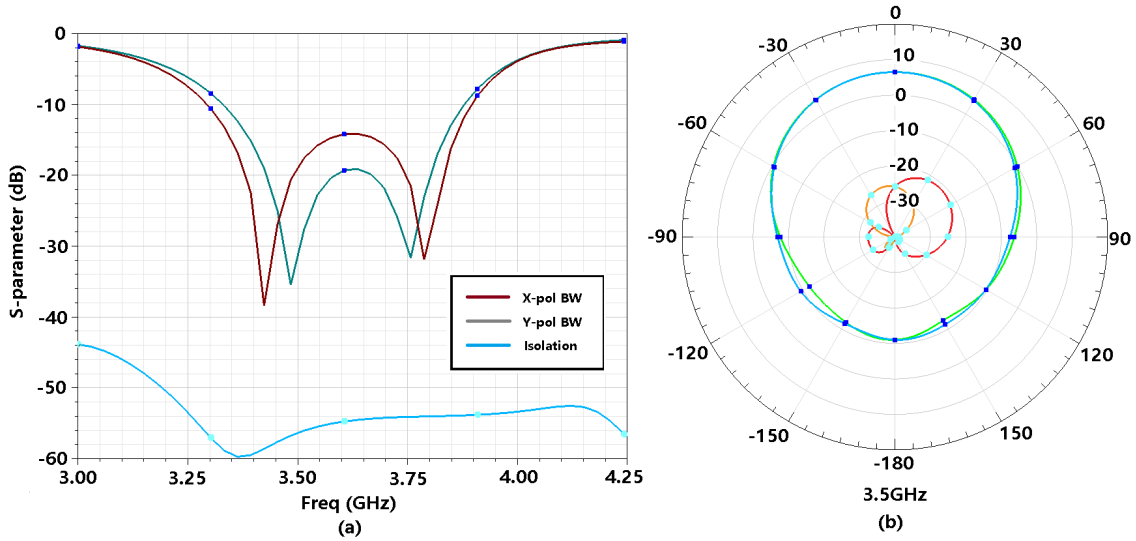

Figure 3.13: Stacked patch simulation results: (a) Simulated return loss for both polarization ports (black/green/box) and isolation between ports (blue/circle), (b) Co-polarization at 3.5GHz (blue/green/box) and cross-polarization at 3.5GHz (red/orange/circle).

tire bandwidth. The isolation between polarization ports is -50dB and cross-polarization at bore-sight is 33dB. The array is also designed at 0.5λ spacing and the highest coupling between elements is simulated to be -18dB. The stacked patch has decent electrical performance while offering good mechanical stability and high integration possibility. The dual-polarized aperture and proximity coupled stacked patch antenna design will be chosen as the final antenna design type and further simulations will be conducted as the design is modified to fit for more realistic implementation in the next section.

3.1.3 Finalized antenna design

With the antenna structure and feeding network decided, practical considerations such as stack-up, assembly, and connectors need to be implemented in the design and simulated.

The connectors chosen for this antenna are surface launch SMA connectors, with this type of connector, no soldering is needed, instead, screws will be used to connect between the antenna and connector allowing easy re-connection between the connector rendered loose during testing. The stack-up of the antenna is made to be symmetric for fabrication purposes. Due to a large number of antenna layers and air layer between the parasitic patch and driven patch, the entire antenna design is split up into three parts: feed network, driven patch, and parasitic patch, all three sub-designs use the same stack-up configuration. The three sub-designs will be fabricated separately on the same panel and assembled using spacers and screws. The final structure is shown in Figure 3.14, an additional back-frame is added in the antenna design to reduce interference from the antenna to other front-end hardware due to the backward radiation from the aperture coupled feeding technique and to fixate each antenna module in an array formation. Three parts for antenna assembly are shown in Figure 3.14.c and all parts are printed on the same stack-up.

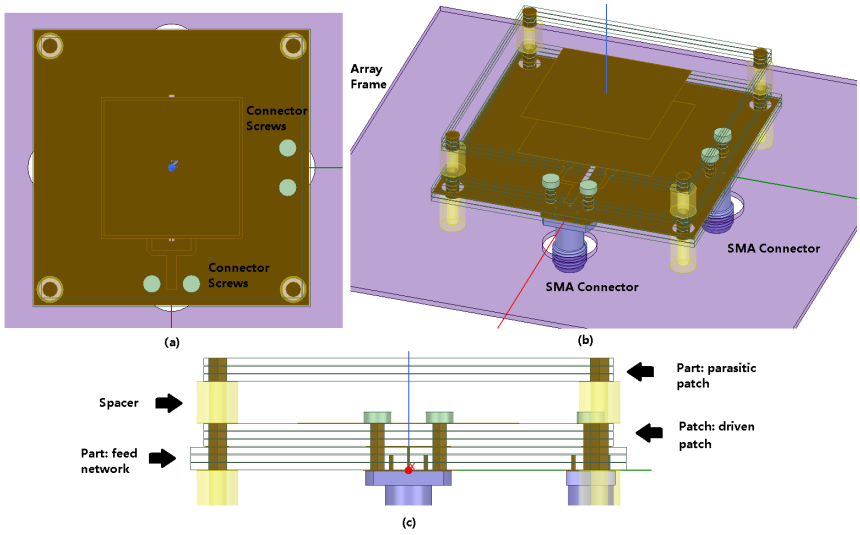

Figure 3.14: Final antenna structure: (a) Top view, (b) Trimetric view, (c) Right view.

The simulation results are shown in Figure 3.15, the -10dB bandwidth for both polarization ports to be 3.2-3.7 GHz, isolation between polarization ports is -35dB, cross-polarization at bore-sight is 25dB at 3.5 GHz, realized gain to be 6.8dBi at 3.5GHz and 6-7dBi over the entire bandwidth. The radiation pattern is simulated at 3.2, 3.5, and 3.7 GHz in Figure 3.16, gain and cross-polarization are persistent across frequency bandwidth. Isolation and cross-polarization are degraded from the ideal stacked patch design shown in the previous section, the contribution however comes from the added backplate which acts

as the antenna array frame and shielding. Bandwidth is also slightly reduced due to the extra parasitic effects of the SMA connection transition from the probe to micro-strip. The final simulated performance for the antenna design is satisfactory from both an electrical and mechanical point of view.

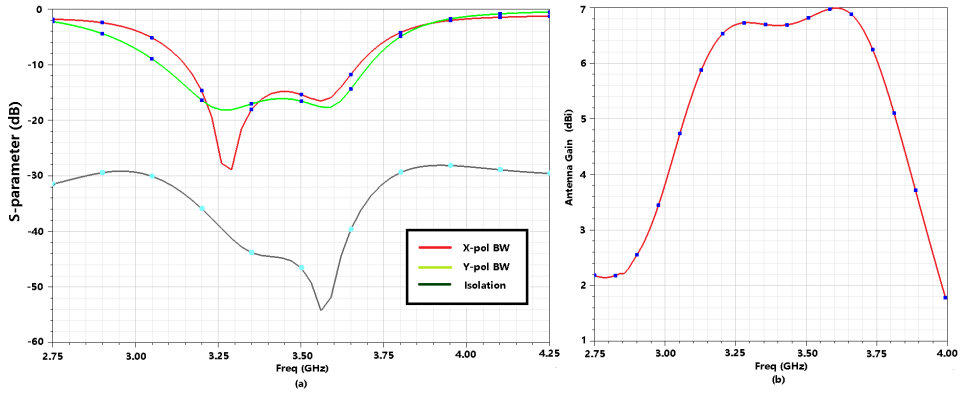

Figure 3.15: Final antenna structure simulation results: (a) Simulated return loss for both polarization ports (red/green/box) and isolation between ports (black/circle), (b) Realized antenna gain (red/box).

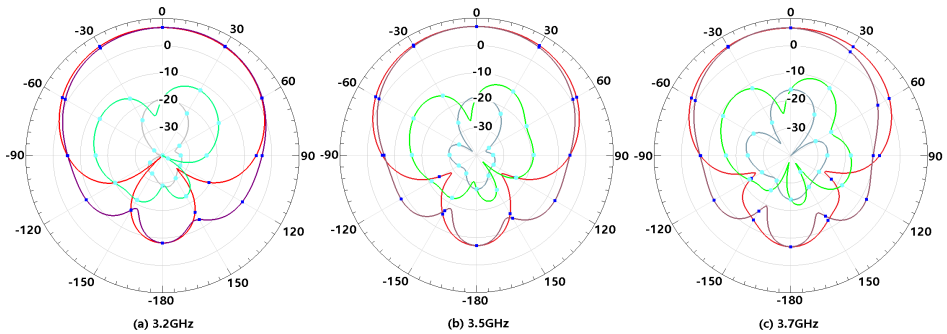

Figure 3.16: Final antenna structure radiation patterns for co-polarization (red/purple/box) and cross-polarization (green/grey/circle) at: (a) 3.3GHz, (b) 3.5GHz, (c) 3.7GHz.

3.1.4 Antenna measurements

The single element antenna is fabricated, assembled, and tested. The single element antenna measurement is given in Figure 3.17 with simulation comparison. A slight frequency shift is observed between measurement and simulation, overall the simulation matches very well with measurement due to the well-made simulations models from previous sections. The -10dB bandwidth for both polarization ports is 3.15 to 3.7GHz and isolation within bandwidth is better than 40dB.

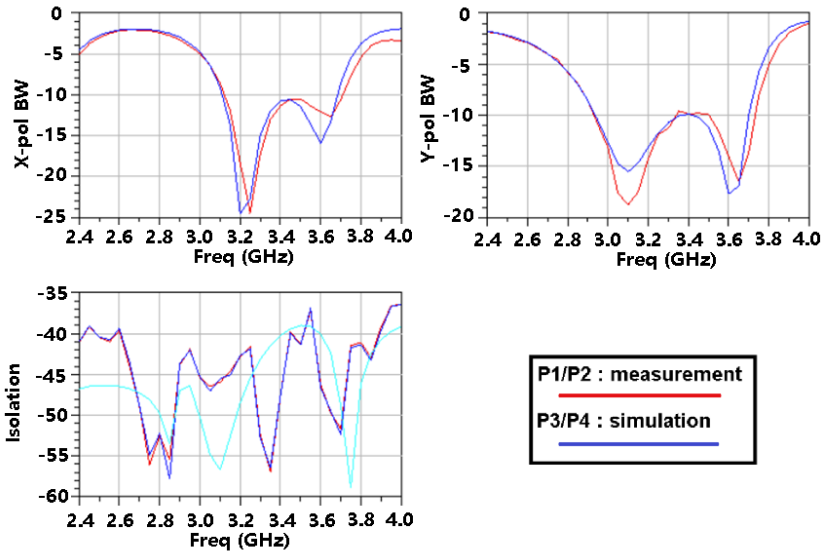

Figure 3.17: Patch antenna measurement vs. simulation results for: (a) X-pol port, (b) Y-pol port, (c) Isolation between ports.

3.2 PA design

3.2.1 Basic PA operation mode

Power amplifiers have different modes of operation. PA transistor is commonly divided into two different types, field-effect transistor (FET) or bipolar junction transistor (BJT). FET has a much higher input impedance compared to BJT, thus FET is commonly characterized

as a voltage-controlled device where BJT is commonly characterized as a current-controlled device. Due to mMIMO sub-6GHz PA specifications such as operating frequency, efficiency, output power, and gain, the majority of BS PAs are designed using FET due to their high efficiency, output power, and operational frequency. Common operation modes for FET PAs are class-A, AB, B, and C depending on the conduction angles of operation.

As mentioned FET can be characterized as a voltage-controlled device such as voltage-controlled current source (VCCS) where the input gate voltage, V_gs, controls the output drain current, I_dc, through a trans-conductance value, g_m. As shown in Figure 3.18, an ideal FET model behavior is characterized through an ideal VCCS with a threshold voltage. As seen from the ideal FET model DC-IV curves, for a linear PA output, V_gs would need to be between the threshold voltage and maximum gate voltage with the FET operating in the saturation region. From the DC-IV curves for the ideal FET, the basic theory of different conduction angles of operation mode for PA can be conducted. The transistor is only conducted when the input signal voltage together with the gate bias is past the voltage threshold point, thus the transistor will experience different conduction times in one signal period, and multiple operation modes are defined based on the conduction time or conduction angle of the transistor.

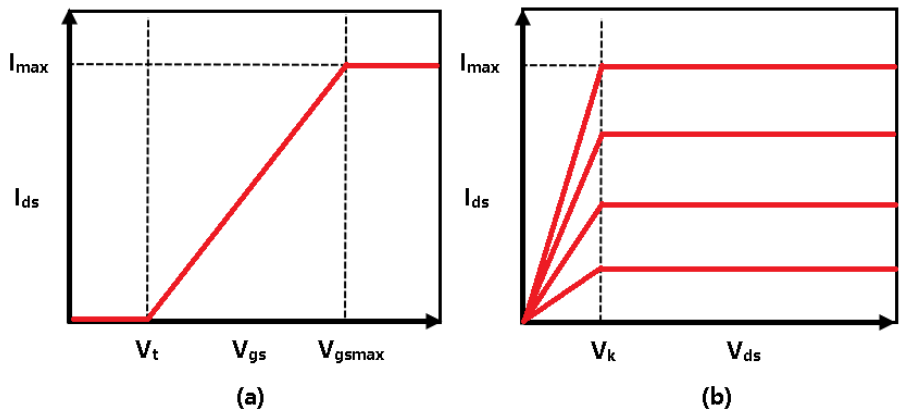

Figure 3.18: DC IV characterization of a transistor, (a) Idc vs Vgs (b) Ids vs Vds

Depending on the conduction angle of the transistor, the drain current may or may not be a perfectly sinusoidal wave which translates to an output waveform following the shape of the input gate voltage waveform. A general formulation of a non-sinusoidal waveform can be broken down with Fourier series decomposition, analyzing the fundamental and

harmonic drain current is shown in Equation 3.1 to Equation 3.3. The general power and efficiency equation is derived shown in Equation 3.4 to Equation 3.6.

$$i(\omega t) = I_0 + I_1 cos(\omega t) + I_2 cos(\omega t) + ... \tag{3.1}$$

$$I_0 = \frac{1}{2\pi}\int_{\theta}^{-\theta} I(cos(\omega t) - cos(\theta))d\omega t = \frac{I}{\pi}(sin(\theta) - \theta cos(\theta)) \tag{3.2}$$

$$I_1 = \frac{1}{\pi}\int_{\theta}^{-\theta} I(cos(\omega t) - cos(\theta))cos(\omega t)d\omega t = \frac{I}{\pi}(\theta - sin(\theta)cos(\theta)) \tag{3.3}$$

$$P_0 = I_0 V_{dc} \tag{3.4}$$

$$P_1 = \frac{I_1 V_1}{2} \tag{3.5}$$

$$\eta = \frac{P_1}{P_0} = \frac{I_1 V_1}{2 I_0 V_{dc}} = \frac{(\theta - sin(\theta)cos(\theta))V_1}{2(sin(\theta) - \theta cos(\theta))V_{dc}} \tag{3.6}$$

Assuming ideal FET operation, where knee voltage is set to 0, V_1 will be the same as V_dc for maximum voltage swing and the general DE equation will be simplified to Equation 3.7.

$$\eta_{ideal} = \frac{P_1}{P_0} = \frac{(\theta - sin(\theta)cos(\theta))}{2(sin(\theta) - \theta cos(\theta))} \tag{3.7}$$

The general formula above can be used to form different modes of PA operation. For class A, the transistor is always conducting with the gate bias is located center point between threshold voltage and maximum gate voltage, the corresponding conduction angle 2θ is 2π. Setting the half conduction angle θ as π, the ideal class A can achieve peak efficiency of 50% with the full linear operation. For class B, the transistor is conducting half the time, with the gate bias is located at the threshold voltage point, the corresponding conduction angle up to π. Setting the half conduction angle θ as $\frac{\pi}{2}$, the ideal class B can achieve peak efficiency up to 78.5% with linear operation depending on output harmonic impedance.

For class AB, the transistor's conduction time may vary between full and half cycle, the game bias is located between the threshold voltage and center point for class A, the corresponding conduction angle is between 2π and π. Setting the half conduction angle θ between π and $\frac{\pi}{2}$, the ideal class AB can achieve peak efficiency up to 78.5% with less linear operation compared to class A and class B. For class C, the transistor is conduction less than half the time, with the gate bias below the threshold voltage point, the corresponding connection angle is less than π. Class C experiences the highest peak efficiency at the price of low gain and highly non-linear operation.

Operation mode	Linearity	Gain	Efficiency
Class A	High	High	Low
Class AB	Moderate	Moderate	Moderate
Class B	High	Moderate-low	Moderate
Class C	Low	Low	High

Table 3.8: Comparison of PA operation modes

A trade-off between linearity, gain, and efficiency is made when selecting the PA operation mode between class A, class B, class AB, and class C. A comparison table is made in Table 3.8, the most flexible and comprehensive PA mode of operation is determined to be class AB. While advanced modes of operation such as Doherty PA, switched PA and out-phasing PA are available, it is out of the scope of this work to discuss in further detail.

3.2.2 Matching, layout, and simulation

The FET transistor chip used in this design is the packaged GaN HEMTs CGHV1F006S from Cree. The stack-up uses a two-layer configuration with the top metal layer being the main PA layer and the bottom layer being ground, the substrate used is 32 mil RO4003C material, with a dielectric constant of 3.55. Initial DC simulations are conducted for drain/gate bias point and R_{opt} approximation from DC-IV load curves. For the class AB design, the gate bias point is picked to be 0.22V, drain bias point is picked to be 28V. The R_{opt} is calculated to be 84Ω and the output capacitance of the transistor C_{out} is measured to be 0.514 fF.

Commercial packaged PA transistor has non-negligible parasitic such as bond wire inductance and pad capacitance at the frequency of operation for mMIMO sub6-GHz PAs thus both input and output matching network of PA needs to be designed with the parasitic

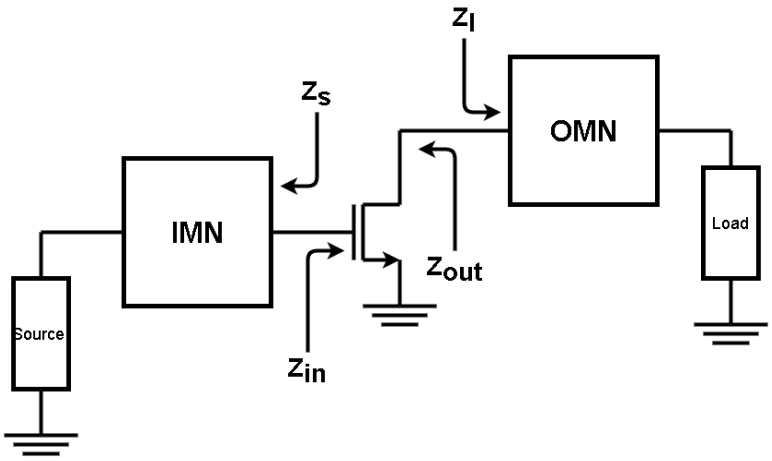

Figure 3.19: PA source/load impedance matching

in mind for proper absorption or compensation. The transistor is load and source pulled at fundamental and harmonics to find the optimum impedance at input and output of PA with packaged parasitic included as well as EM simulated transistor pad for realistic model. Once the source and load impedance is determined, the matching networks are realized with stepped microstrip transmission lines for capacitive and inductive impedance matching shown in Figure 3.19. The output matching network has a major contribution to PA efficiency and output power, which is a crucial part of PA design. The output matching network needs to be designed to absorb the non-linear output capacitance of the packaged transistor which will undoubtedly be a difficult to implement and band-limited solution due to limited variables from the matching network alone. Thus the drain bias network is also used as part of the output matching for easier implementation and wider band performance while the decoupling capacitors on the drain bias network are selected to provide a low impedance at low-frequency bands to prevent drain voltage modulation. The input matching network has a major contribution to the PA gain, stability, and AMPM, and the same design method for output matching network is implemented for input matching network with the additional considerations for the stability of the overall PA. Stability resistors are established for both in-band RF, low freq, and harmonics to ensure antenna-induced load modulation will not cause the PA to see unstable loads. Overall simplified PA schematic is shown in Figure 3.20.

The PA is designed in Advanced Design Software (ADS), with layout full EM simulated by EMpro. Space-mapping technique is employed to transfer the design from schematic to initial EM layout, later on, global optimization is deployed for overall system performance

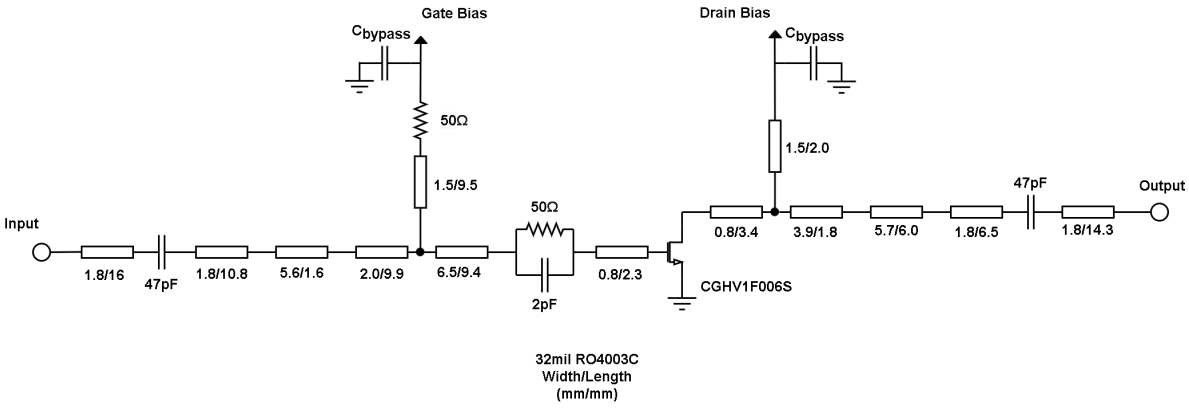

Figure 3.20: PA schematic

tuning. Once tuned performance is satisfied, the design is ported to Altium for PCB layout and re-simulated in Ansys HFSS for cross-validation between ADS and HFSS results. The final layout design is shown in Figure 3.21 from Altium where all SMD elements are highlighted.

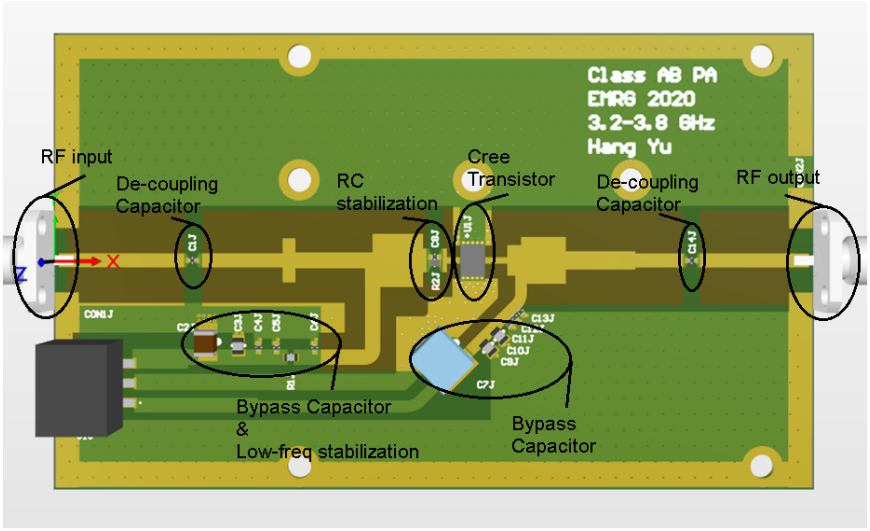

Figure 3.21: Altium PA 3D layout

The simulated PA CW results with 50Ω load are shown in Figure 3.22. Input power is swept from 0 to 30 dBm with the frequency ranges from 3.2 to 3.8 GHz. The final simulated results show the small-signal gain of 12 to 13.5 dB, saturated power of 36 to 37

dBm, drain efficiency up to 61 to 69, and PAE up to 55 to 61 at saturated power. The P_{1db} power is simulated to be 33 to 34 dBm and drain efficiency up to 42 to 54 and PAE up to 38 to 51 at P_{1db} power. The AMPM is shown to have a maximum peak 7° within saturated power over the entire frequency bandwidth.

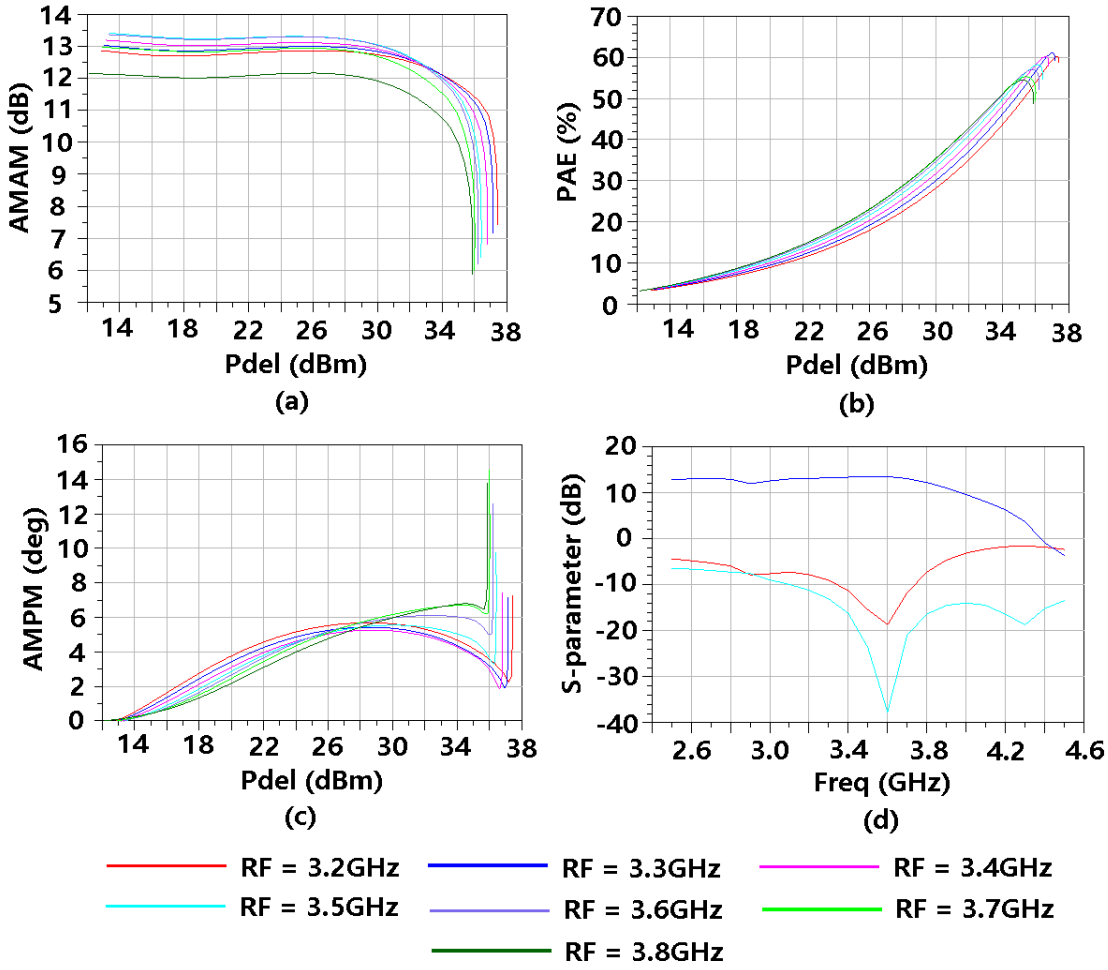

Figure 3.22: CW simulation results: (a) AM/AM vs. output power, (b) AM/PM vs. output power, (c) PAE vs. output power, (d) Small signal S-parameters.

The simulated PA modulated signal results with 50Ω load are shown in Table Table 3.9. Input signals simulated are 100MHz and 200MHz 8dB PAPR OFDM signal fed into HFSS EM simulated PA. Table 3.9 presents modulated signal results for different bandwidths

before and after SISO DPD applied. The purpose of this simulation is mainly to verify the linearizability of the PA in terms of DPD application.

Before DPD					
Bandwidth (MHz)	NMSE (%)	ACPR Left (dB)	ACPR Right (dB)	Average DE (%)	Average Power (dBm)
100	5.1	-34.8	-33.3	25.0	27
200	5.9	-35.5	-32.8	24.7	27
After DPD					
100	0.2	-63.5	-63.0	24.7	27
200	0.3	-60.6	-59.5	24.4	27

Table 3.9: Modulated signal simulation results

3.2.3 PA measurements

3.2.3.1 Small signal and large-signal measurements

Four PAs are fabricated for 2x2 array configuration and evaluated for performance with small signal, large signal, and modulated signal. Small signal measurements are shown in Figure 3.23 for input matching (S_{11}), output matching, forward gain and reverse isolation. Comparison between measurement and simulation matches very well with simulation with a slight frequency shift and minor variation is observed between individual PA units due to fabrication variance.

For large-signal measurements, Keysight PNA-X N5247A is used to characterize the PAs. The input sinusoidal wave is amplified with Mini-Circuits ZHL-42+ drivers, providing enough power to saturate PA. The PA output is connected to a -30dB attenuator matched to 50Ω followed by the Keysight PNA, the attenuator is in place to protect PNA from excessive power. Large signal measurement results are shown in Figure 3.24, Figure 3.25, Figure 3.26 and Figure 3.27 for the four different PAs respectively. The measurement results demonstrate the small-signal gain of 11.7 to 14 dB, saturated power of 36 to 38 dBm, drain efficiency up to 62 to 69, and PAE up to 51 to 61 at saturated power across all four units. The AMPM is shown to have a maximum peak 5° within saturated power over the entire frequency bandwidth for all four units.

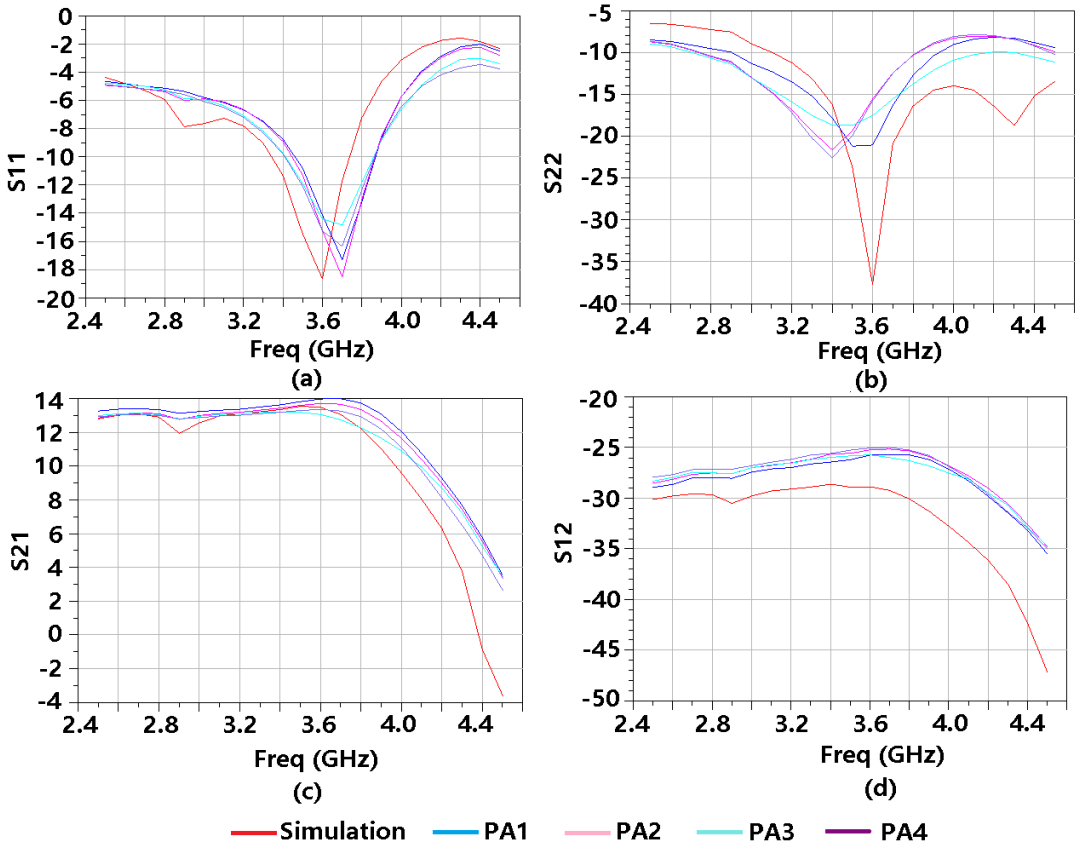

Figure 3.23: S.S. PA array measurement vs. simulation results: (a) S11, (b) S22, (c) S21, (d) S12.

3.2.3.2 Modulated signal measurement

For the modulated signal test, a Keysight M8190A dual-channel arbitrary wave generator generates an 8dB PAPR OFDM signal with different bandwidths. The PA output is passed through a -30dB attenuator and captured by a Keysight DSOS404A four-channel oscilloscope which is fed to PC with MATLAB for digital signal processing.

The measured PA modulated signal results with 50Ω load are shown in Table 3.10 with different DPD coefficients applied. The PA is shown to be capable of linearizing 100MHz and 200 MHz OFDM signals with 31 coefficients, and a plateaued improvement of ACPR level is observed with DPD coefficients increased up to 61 and 96.

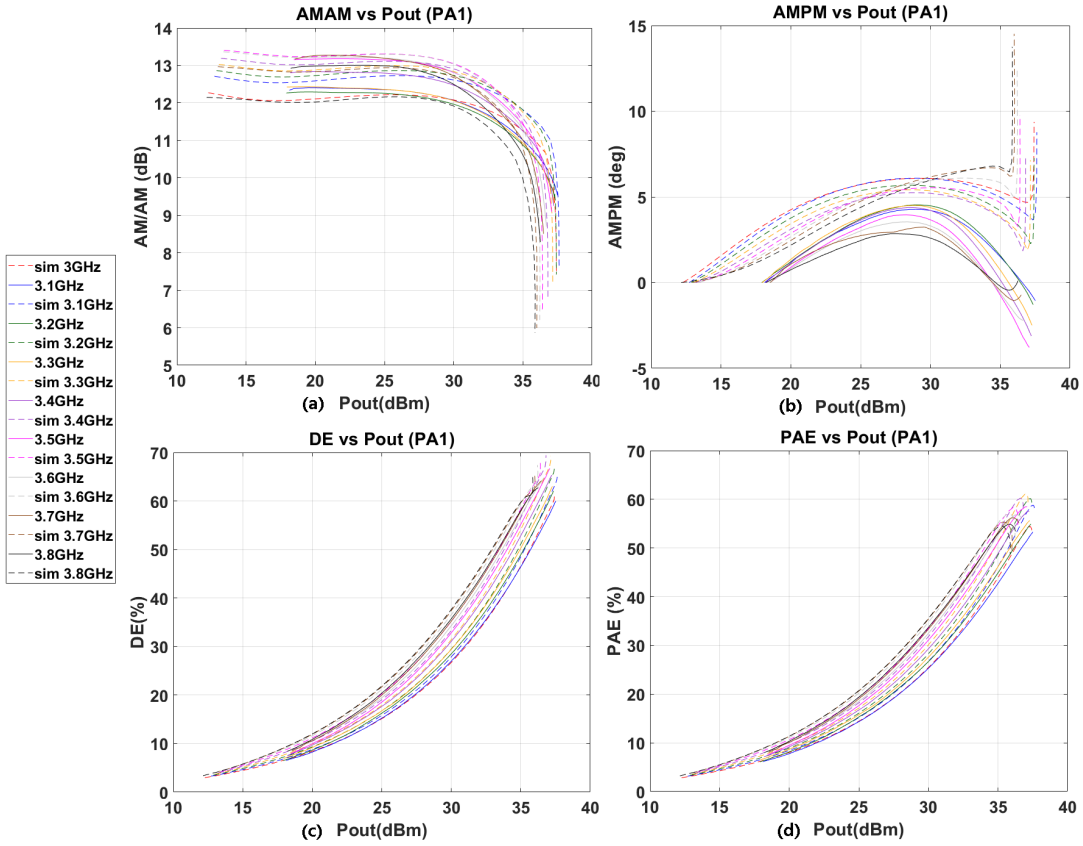

Figure 3.24: L.S. PA1 measurement (solid) vs. simulation (dotted) results: (a) AMAM, (b) AMPM, (c) DE, (d) PAE.

The measured PA modulated signal results with 50Ω load are shown in Table 3.10 with all 4 pairs of PA with driver for 2x2 configuration. All four PAs can linearize 100MHz OFDM signals with 61 coefficients, variations can be contributed due to PA and driver hardware differences, but overall similar behaviors. The output spectrum, AM/AM, AM/PM and gain variation result plots for measured PA unit4 with 100MHz OFDM 8dB PAPR and 61 DPD coefficients are shown in Figure3.28.

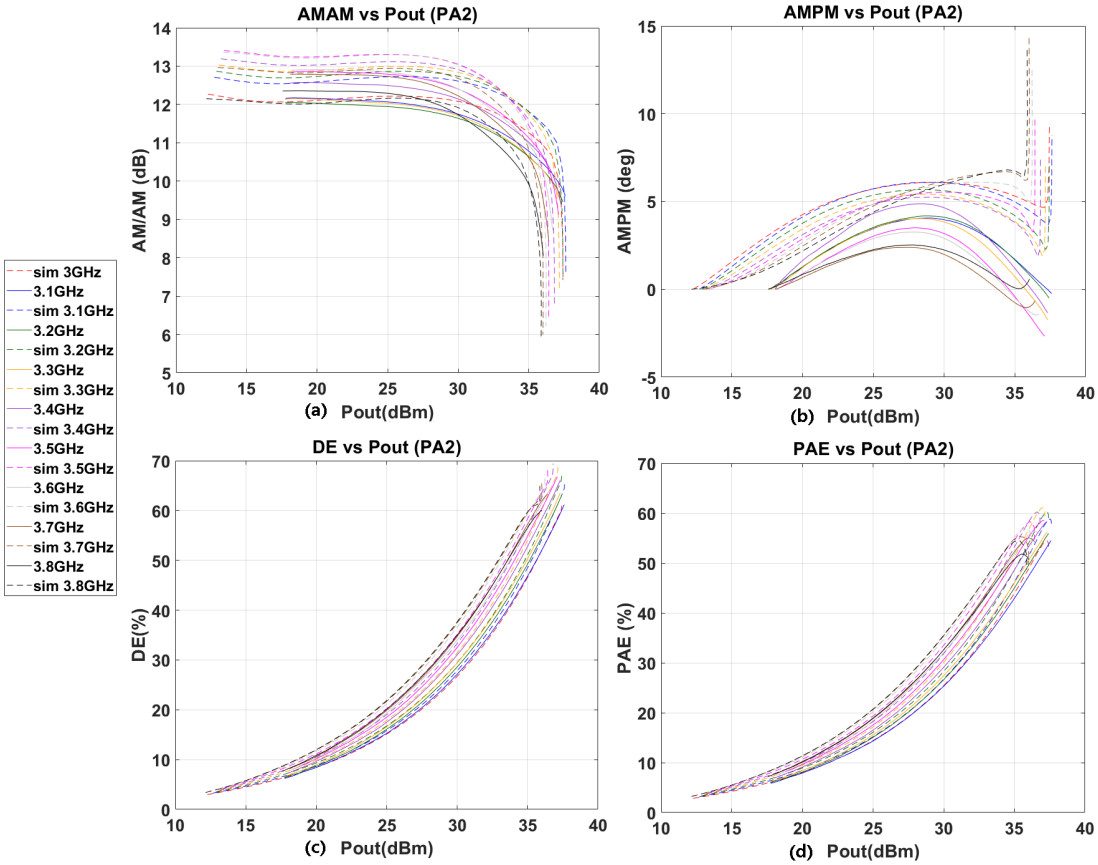

Figure 3.25: L.S. PA2 measurement (solid) vs. simulation (dotted) results: (a) AMAM, (b) AMPM, (c) DE, (d) PAE.

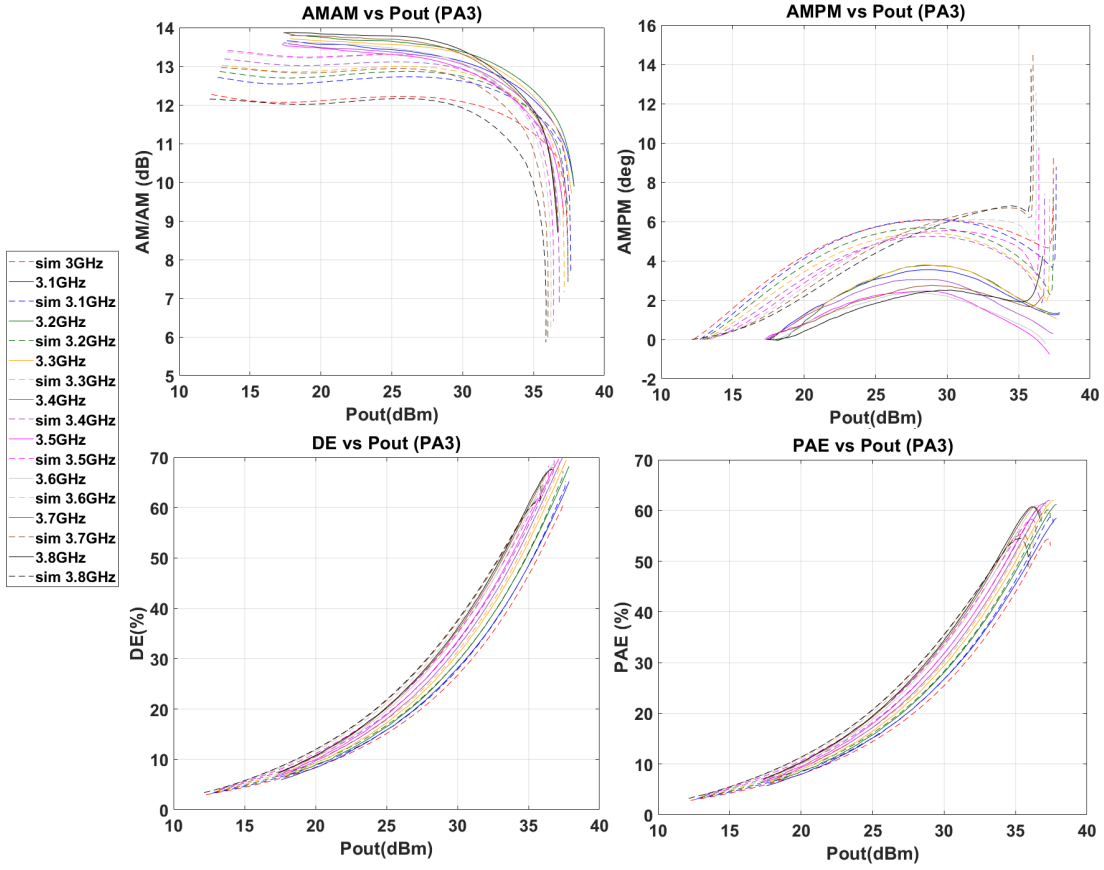

Figure 3.26: L.S. PA3 measurement (solid) vs. simulation (dotted) results: (a) AMAM, (b) AMPM, (c) DE, (d) PAE.

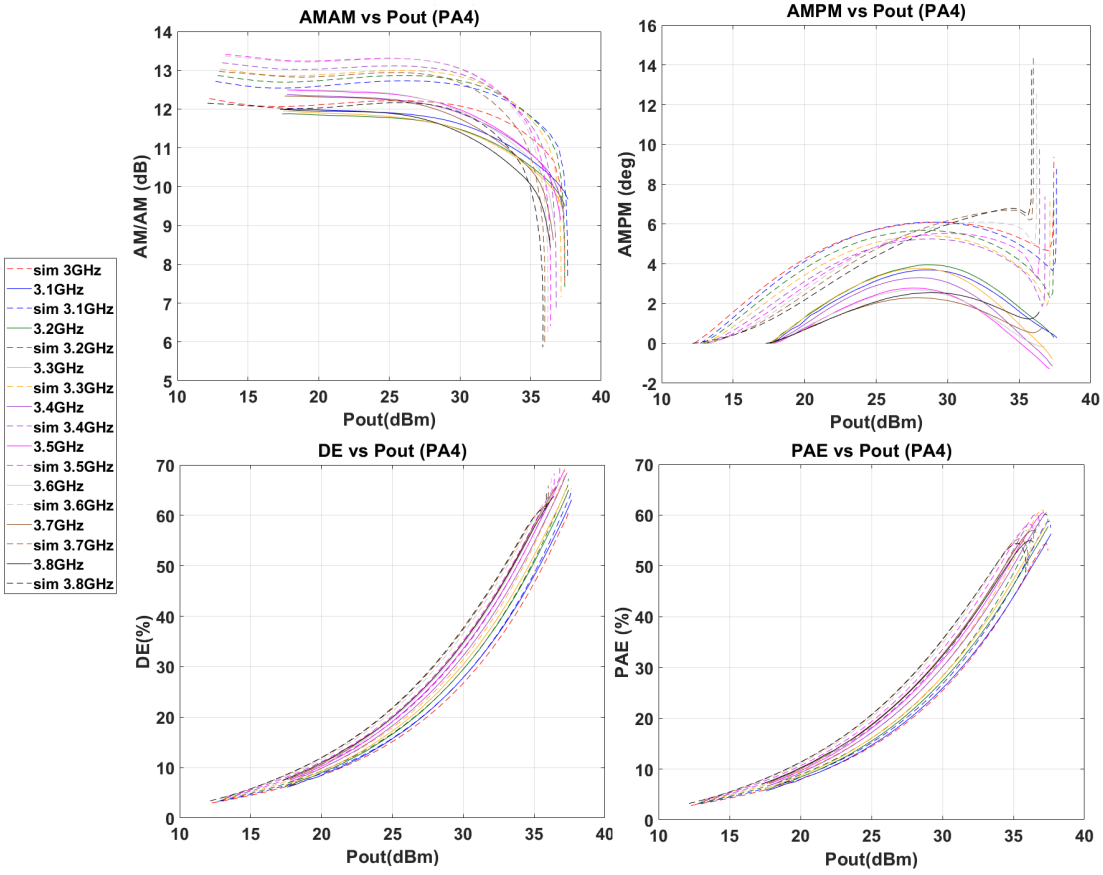

Figure 3.27: L.S. PA4 measurement (solid) vs. simulation (dotted) results: (a) AMAM, (b) AMPM, (c) DE, (d) PAE.

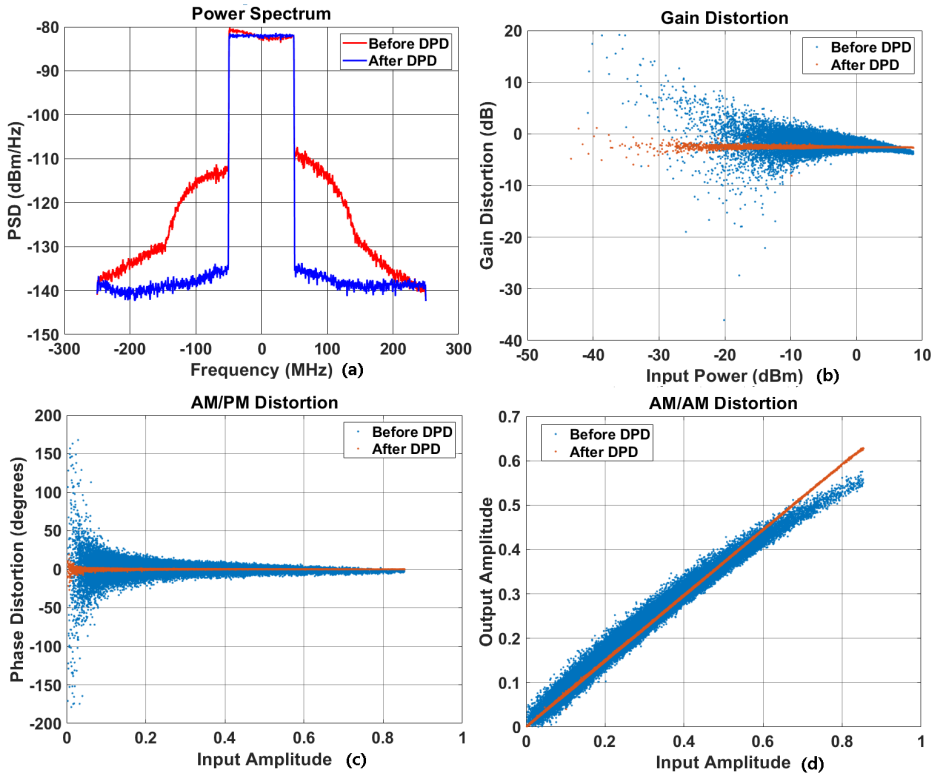

Figure 3.28: PA modulated signal measurement results with 50Ω load

Before DPD					
Bandwidth (MHz)	DPD Coeff.	NMSE (%)	ACPR Left (dB)	ACPR Right (dB)	Average Power (dBm)
100	31	8.8	-33.8	-31.7	29.0
100	61	8.9	-33.8	-31.7	29.0
100	96	8.8	-33.9	-31.7	29.0
200	31	11.2	-33.3	-31.7	29.0
After DPD					
100	31	0.4	-54.0	-54.8	29.0
100	61	0.3	-57.3	-57.6	29.0
100	96	0.3	-58.7	-58.9	29.0
200	31	0.7	-50.8	-50.2	29.0

Table 3.10: Modulated signal measurement results vs. DPD coefficients

Before DPD					
Bandwidth (MHz)	DPD Coeff. PA#	NMSE (%)	ACPR Left (dB)	ACPR Right (dB)	Average Power (dBm)
100	61 (PA1)	9.2	-33.0	-30.0	29.3
100	61 (PA2)	10.5	-33.0	-31.0	29.4
100	61 (PA3)	10.0	-34.0	-31.0	29.3
100	61 (PA4)	10.3	-34.0	-32.0	28.9
After DPD					
100	61 (PA1)	0.36	-57.0	-56.0	29.2
100	61 (PA2)	0.30	-59.0	-58.0	29.3
100	61 (PA3)	0.42	-54.0	-55.0	29.0
100	61 (PA4)	0.45	-54.0	-54.0	28.8

Table 3.11: Modulated signal measurement results vs. PA+driver pairs

Chapter 4

Two-by-two front-end demonstrator

4.1 Antenna array design

4.1.1 Simulation

Each antenna element was designed to be modular such that different array spacing can be configured to test the effect of cross-talk during mMIMO transmitter performance. Full EM simulations are conducted for different spacing options to study the effect of coupling level and radiation pattern in array setups.

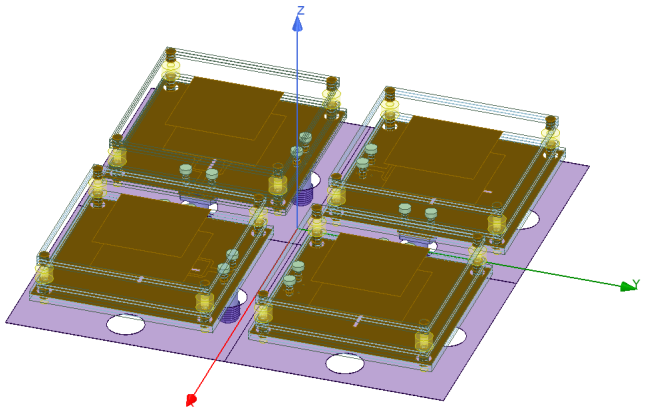

Figure 4.1: Stacked patch 2x2 array

The 2x2 array is simulated in EM shown in Figure 4.1. With different spacing options, the highest coupling levels are -20.4dB at 0.6λ, -22.6dB at 0.7λ and -23.0dB at 0.8λ at 3.5 GHz. The largest improvement in the highest coupling level with respect to array spacing is from 0.6λ to 0.7λ for 2.2dB while an improvement from 0.7λ to 0.8λ coupling is not significant. Suggesting just simply increasing the spacing indefinitely is not an efficient idea to improve coupling because of the plateaued trend and the trade-off with the overall array radiation pattern.

The radiation pattern of 4x4 array beam-forming is shown in Figure 4.2 for bore-sight and 15° beam steer. Due to the complex antenna models, simulating 16 antennas with 32 ports requires computing power beyond available resources thus a simplified antenna model is used instead. Although the simplified model results are less accurate than reality, it is enough to show a general trend about the radiation pattern of an array for different spacing options.

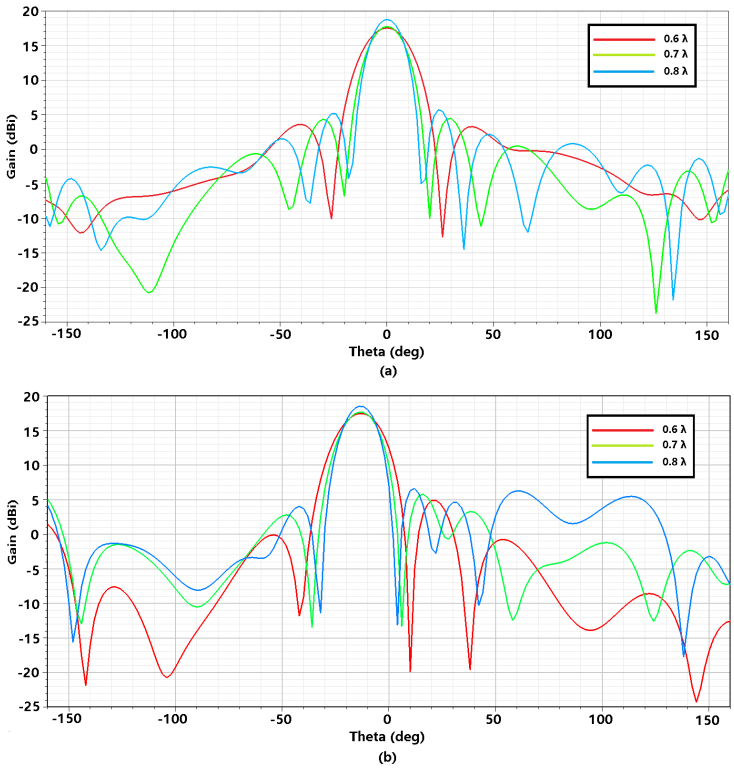

Figure 4.2: Array simulation results: (a) S-parameters at 0.7λ, (b) Highest coupling at different spacings.

At bore-sight with various spacing at 0.6λ, 0.7λ and 0.8λ, comparing the radiation pattern with different array spacing options, the side-lobes are higher as spacing becomes greater as well as the overall gain and beam-width. The same observation holds true for beam-steered radiation pattern at 15°, but the side lobes and radiation leakage degrades more than at bore-sight. This type of beam-forming radiation pattern however only holds true for line-of-sight scenarios, only for analog beam-forming, while sub 6GHz mMIMO transmitter will be deployed with fully digital beam-forming, where the transmitter will not operate in line-of-sight scenario majority of the operation time. An important trade-off needs to be addressed between the array cross-talk level and side-lobe leakage level for optimal mMIMO transmitter performance.

4.1.2 Measurements

The array measurements are given in Figure 4.3.a with the default spacing of 0.7λ. The -10dB bandwidth is measured to be 3.15 to 3.7GHz. Different coupling levels are measured and divided into three categories as high coupling (adjacent ports with co-polarization), medium coupling (diagonal ports with co-polarization or adjacent ports with cross-polarization), and low coupling (isolation between polarization ports). Different arrays with a variation of inter-element spacing is measured at 0.6λ, 0.7λ and 0.8λ in Figure 4.3.b, the worst coupling level at 3.5GHz is measured to be -21.4 dB, -24.0 dB and -26.3 dB, respectively.

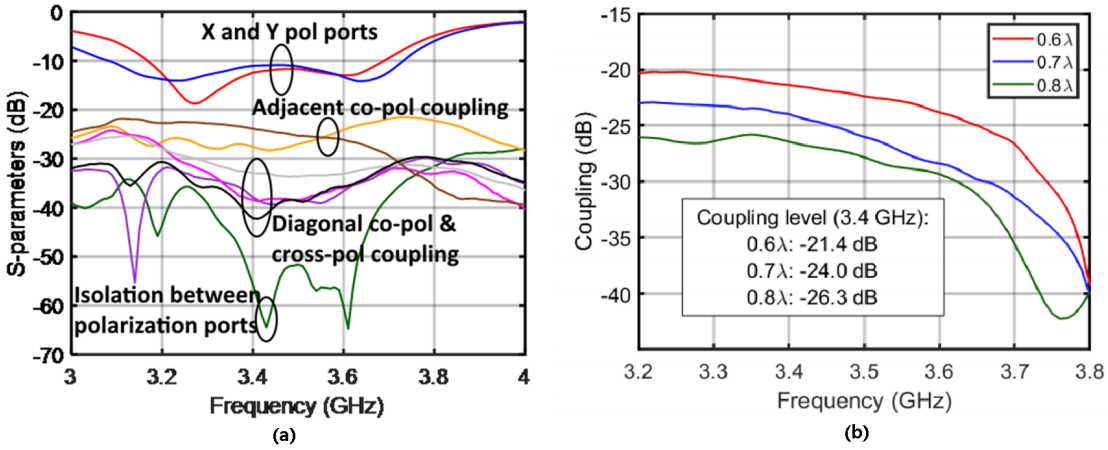

Figure 4.3: Array measurement results: (a) S-parameters at 0.7λ, (b) Highest coupling for 0.6λ, 0.7λ and 0.8λ spacings.

4.2 Mechanical design

The overall frame which houses both the PA array and antenna array is crucial since actions such as handling and traveling will often be performed during testing. The frame is designed with scalability in mind, the mMIMO transmitter front-end would not only be limited only to a 2x2 array but up to 4x4 and 8x8 in the future. This makes modularity and integration extremely important specifications alongside key considerations such as cooling and structural rigidity in the design process.

The transmitter front-end frame is designed to be able to house both the PA array and antenna array in one module, since the antenna array used is dual-polarized, the total number of PAs required to fit within the frame would be doubled compared to the antenna array size. The frame is made to house four antennas, eight PAs, eight SMA cables for antenna PA connection, and two fans for proper cooling. Due to the antenna array spacing, the size of the frame is limited accordingly as well. Multiple antenna frames are designed for reconfigurable antenna array spacing for 0.6λ, 0.7λ, and 0.8λ. The default antenna array spacing is 0.7λ from both electrical and mechanical considerations. The antenna frame model, antenna model, and assembly model are shown in Figure 4.4. As seen from the frame model, and the assembled model, the small cavities of the frame are for screws and bolts mounting antenna modules to the frame, and the big cavities of the frame are for SMA connector cables feeding on PA output ports to antenna input ports.

In mMIMO transmitter, it is desirable to have a solid and short connection between PA and antenna to avoid losses from long cable length and mechanical instability. In order to accommodate eight PAs and four antennas in a modular fashion, the PA is housed below the antenna, limiting the PA design to have width constraints but unlimited length options. The final front-end frame is shown in Figure 4.5, six individual parts can be assembled into a whole frame, with options to scale into an array, and mount cooling fans, screws, and bolts will be used for a stable connection. The slots between the side frame shown in Figure 4.5.c is where the PA heat-sinks will be exposed to airflow and the PAs will be mounted onto the side frames with PA bases screwed in.

The assembled frame with antennas, PAs, fans, and connectors is shown in Figure 4.6, fabrication margins are included in the final design process. Cooling fans are mounted on a fan frame and connected to the mainframe via spacer, screws, and bolts. Small fans and spacers are used to reduce vibration transmission from fans to side frames in order to improve overall frame rigidity. A 90mm long-vacant space is made between the PA and antenna for SMA cable connections, as the shortest SMA cables found online available for purchase are 100mm long. Four PA bases are mounted onto the frame with each base fitted

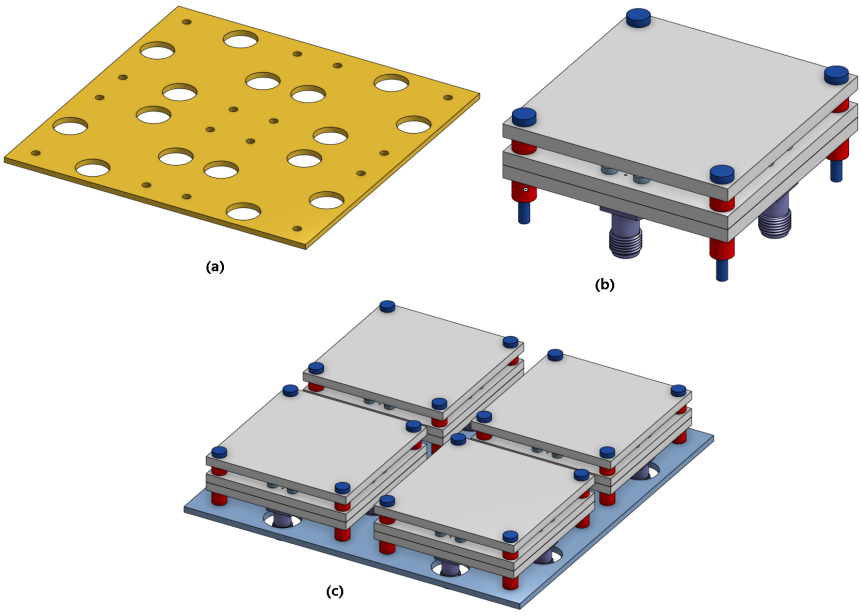

Figure 4.4: Mechanical models: (a) Antenna frame, (b) Antenna, (c) Antenna array assembly.

for two PAs, overall eight PAs can be accommodated under the antenna array. As shown in Figure 4.6.b, the PA output ports are faced towards the antenna input while the PA input ports, DC connectors, and output coupled ports are all routed towards the bottom of the PA bases, this enable easy and clean cable management during testing.

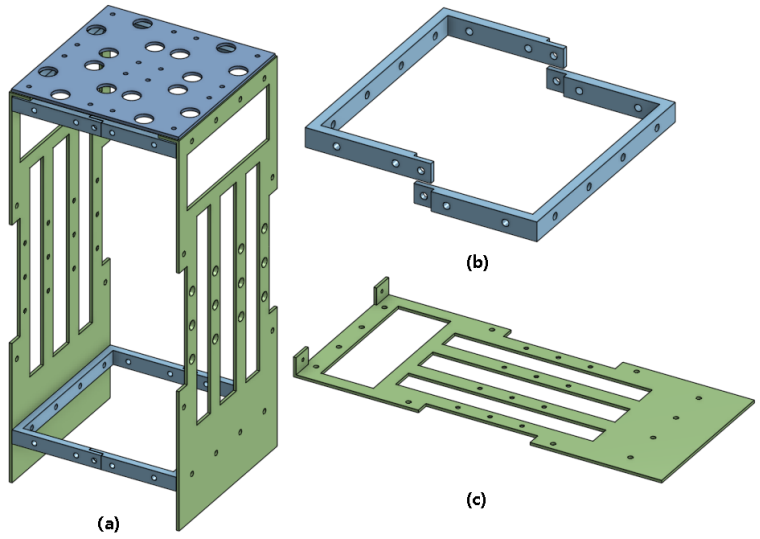

Figure 4.5: Mechanical models: (a) Assembled frame, (b) Support U-frame, (c) Side frame.

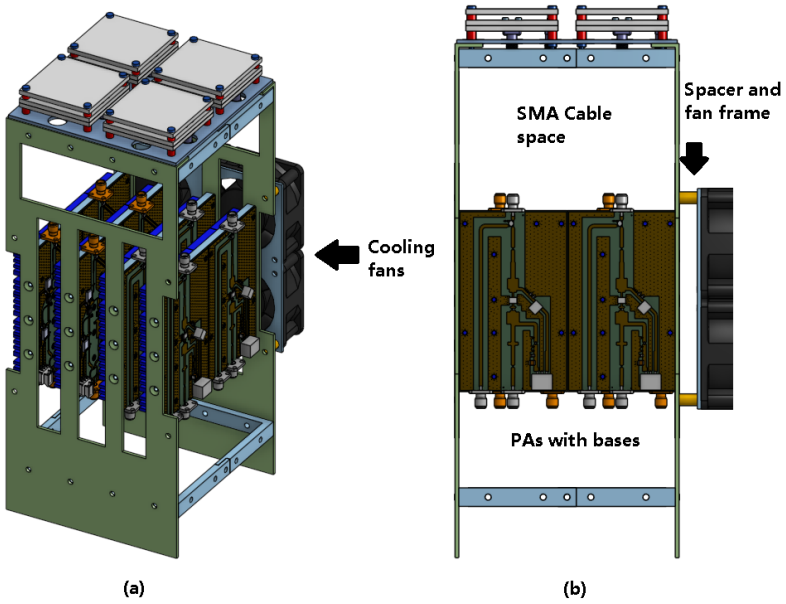

Figure 4.6: Fully assembled model: (a) Trimetric view, (b) Right view.

Figure 4.7 shows the fabricated assembled transmitter front-end with antennas, couplers, PAs, and fans for cooling, The RF inputs and DC connections of PAs are fed from underneath the frame while the coupled PA outputs are received from the sides. The frame only contains 4 PAs for single-polarization only and since the coupler is not integrated within the PA PCB, the bases are forced to be shifted one hole down in the mainframe to create enough space for coupler allocation between antenna and PA.

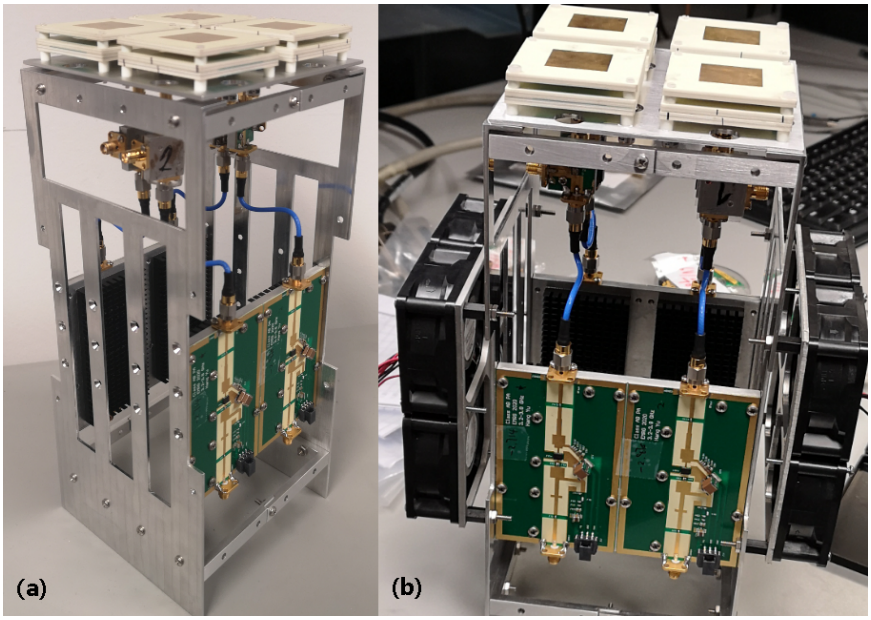

Figure 4.7: Modular 2x2 transmitter front-end: (a) Side view, (b) Front view.

4.3 System setup, measurement, and analysis

4.3.1 Single chain Transmitter

4.3.1.1 Measurement setup

The block diagram of the one-path system is shown in Figure 4.8. The path includes a Mini-Circuits ZHL-42+ driver, designed class AB PA, Anaren X4C40K1-20S directional coupler, and designed dual-pol antenna or 50Ω terminated load. An OFDM signal is generated by

the software MATLAB on a local computer, uploaded to one Keysight M8190A dual-channel arbitrary waveform generator (AWG). The bandwidth of the signals is 100 MHz, and the PAPR is 8dB. The PA output is coupled for both 50Ω and antenna load for a fair comparison, the partial output signal is fed into a Keysight DSOS404A four-channel oscilloscope looping back to the PC, which performs the DPD processing and records measurement results.

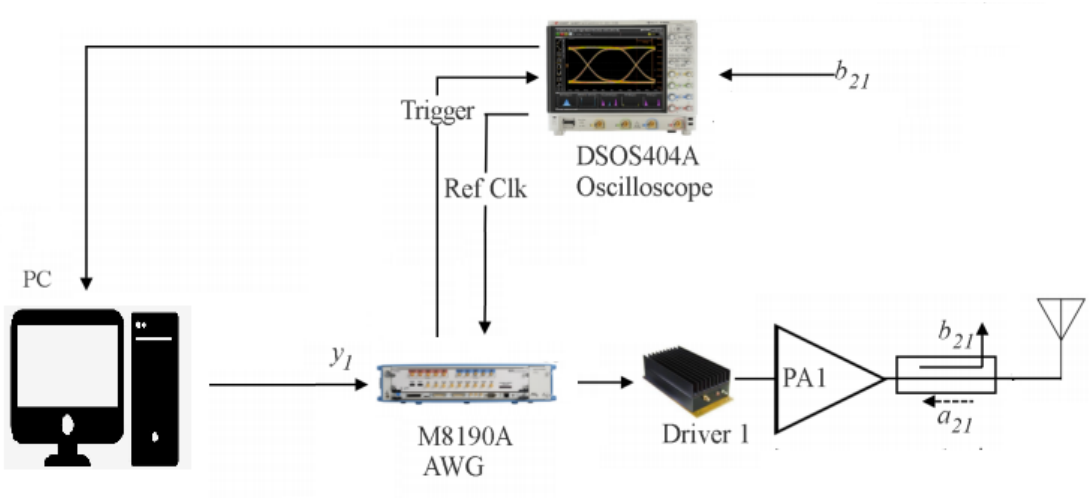

Figure 4.8: One chain modulated signal test setup

4.3.1.2 Measurement results and analysis

Modulated signal testing is conducted for single PA with an antenna chain to compare the performance loss between the ideal 50Ω PA output load versus the antenna PA output load. Figure 4.9 shows the modulated signal measurement plots for class AB PA with antenna as output. Overall modulated signal performance is still satisfactory due to the high linearity performance of the PA from the ideal 50Ω load. The measurement results are compared between 50Ω load and antenna load in Table 4.1, the effect of load mismatch was significant in terms of performance lost. The class AB PA lost 1.2dB of output power, and 8.0 percentage points in drain efficiency, changing the PA output load from 50Ω to antenna. Linearity performances such as NMSE and ACPR also degraded, with the major deterioration being ACPR, increasing from -55 dBc to -50 dBc using the same DPD setup and coefficients.

The antenna has a -10dB bandwidth within the operating frequency range, however,

this amount of performance loss is still alarming and alternative design goals need to be considered to avoid significant transmitter performance loss. Methods such as designing the PA with antenna load instead of 50Ω can be considered in the future, however, this makes the PA circuit element evaluation difficult since precise measurements cannot be conducted for 50Ω load which would no longer offer optimal performance. Techniques to increase the antenna input matching are also possible, however, wideband matching is difficult when trying to balance performance factors such as isolation, size, bandwidth, and matching simultaneously. The possibility of PA designs with reduced load sensitivity was also investigated during the literature review section of Chapter 2, however, currently, no satisfactory solutions are available in terms of sub-6GHz mMIMO PA designs.

Single Chain Measurement: 50Ω load vs antenna								
Load Termination	NMSE (%)		ACPR Left (dB)		ACPR Right (dB)		Average DE (%)	Average Power (dBm)
	Before DPD	After DPD	Before DPD	After DPD	Before DPD	After DPD		
50Ω load	9.5	0.4	-33.7	-56.2	-31.5	-55.2	29.1	28.8
Antenna load	7.9	0.8	-33.1	-49.2	-31.5	-50.7	21.1	27.4

Table 4.1: Modulated signal measurement results for different loads

4.3.2 Two-by-two chain Transmitter

4.3.2.1 Measurement setup

The block diagram of the four-path transmitter system is shown in Figure 4.10. Each path including a Mini-Circuits ZHL-42+ driver, designed class AB PA, Anaren X4C40K1-20S directional coupler, and designed dual-pol antenna. Four uncorrelated and independent OFDM signals are generated by the software MATLAB on a local computer, uploaded to two Keysight M8190A dual-channel AWGs. The bandwidth of the signals is 100 MHz, and the PAPR is 8dB. The two Keysight M8190A AWGs are clock synchronized for optimal input signal quality across all four signal paths. The independent OFDM signals are sent to each RF path of the transmitter front-end where the PAs are connected to a 2x2 antenna array of the same polarization, only one polarization is used currently in this measurement setup. The PA outputs are coupled and partial output signals are fed into a Keysight DSOS404A four-channel oscilloscope looping back to the PC, which performs the DPD processing and records measurement results. The entire measurement is conducted within

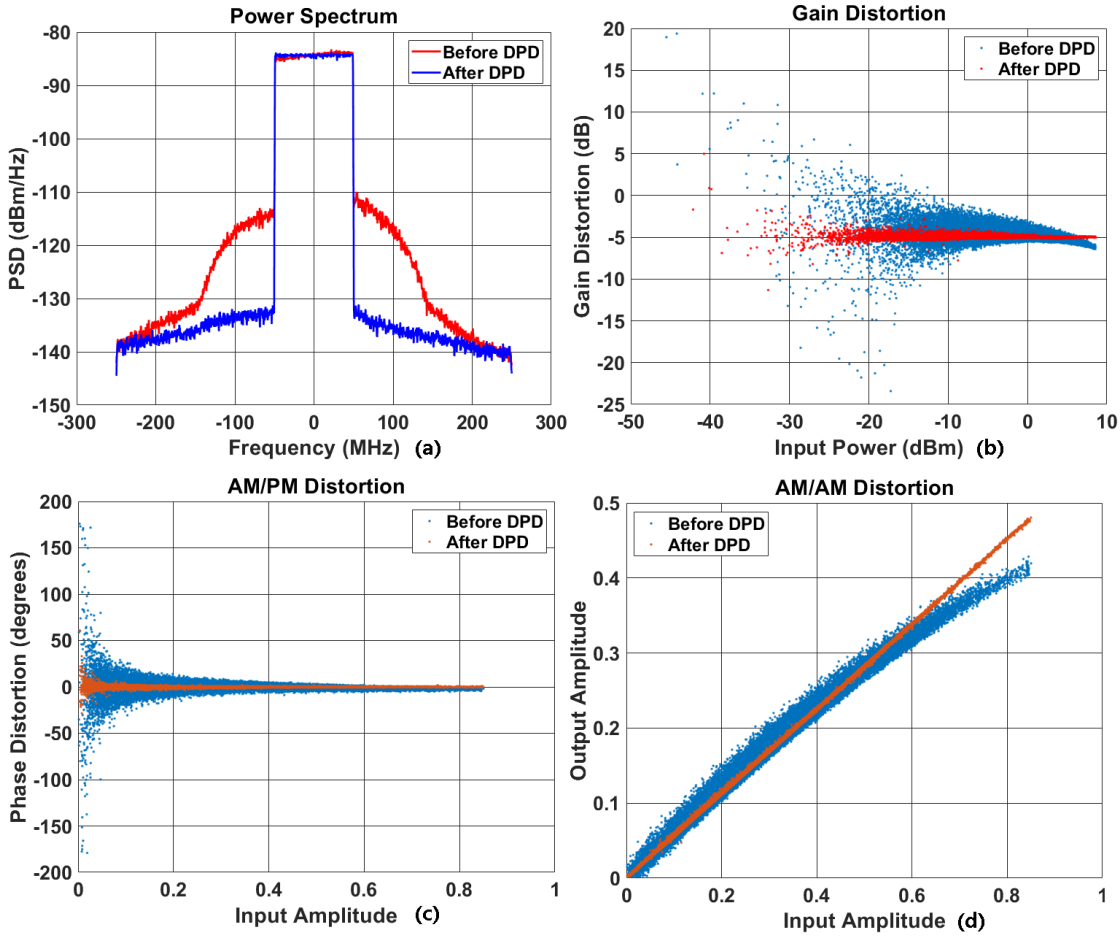

Figure 4.9: Single chain modulated signal measurement antenna load: (a) AMAM, (b) AMPM, (c) gain variation, (d) spectrum.

an anechoic chamber to avoid radiation interference or pollution from the transmitter and outside sources.

4.3.2.2 Measurement results and analysis

Modulated signal testing is conducted for 2x2 PA with antenna chains to compare the transmitter performance between 0.6λ, 0.7λ and 0.8λ spacing for different array coupling levels of -21.4 dB, -24.0 dB, and -26.3 dB, respectively.

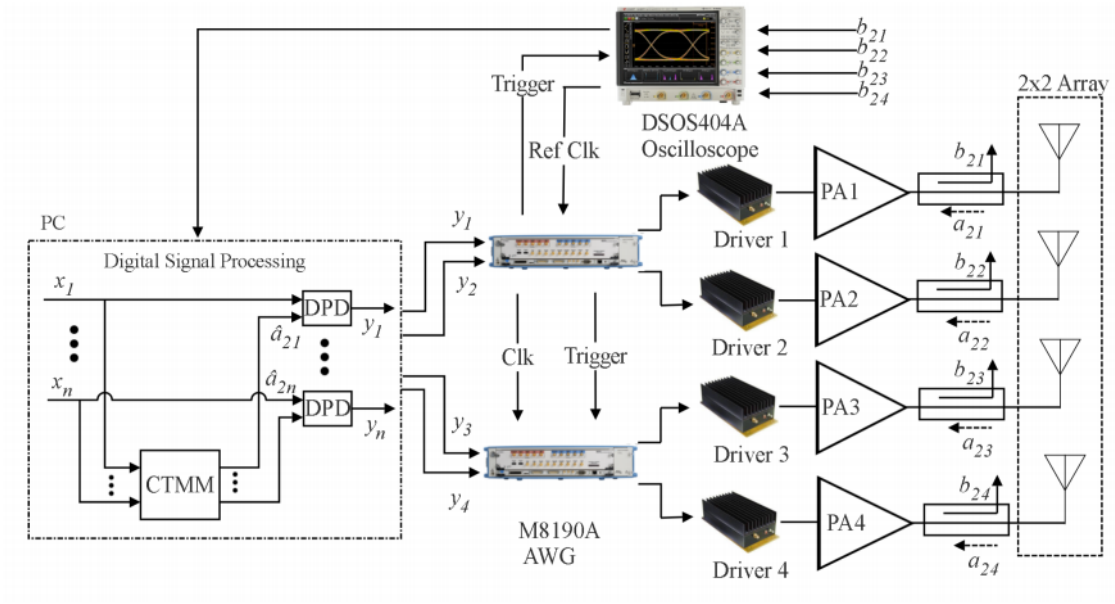

Figure 4.10: Two-by-two modulated signal test setup [36]

The spectrum plots are shown in Figure 4.11, Figure,4.12 and Figure 4.13 for each PA in a 2x2 transmitter setup with 0.6λ, 0.7λ and 0.8λ array spacing respectively. Single input single-output (SISO) and dual input single output (DISO) DPDs are applied separately for transmitter array to compare the effect of cross-talk impact on linearity, power, and efficiency. SISO DPD only considers singular PA linearity, not accounting for array cross-talk and induced load modulation. The DISO DPD employs the dual-input DPD architecture [12], DISO DPD can mitigate the combined effects of PA nonlinearity and antenna cross-talk unlike SISO DPD. As shown in Figure 4.10, the DPD output in each path is a dual-input function of both the path input and the output of the crosstalk and mismatch (CTMM) block that corresponds to this path. The CTMM block approximates the cross-talk signal impinging on each PA output port as a linear combination of the signals in the other paths [12]. During this testing, SISO DPD will have 31 coefficients while DISO DPD will have 43 coefficients, 12 coefficients more to account for cross-talk interference between chains.

The results for individual PA performances are compiled in Table 4.2, Table 4.3 and Table 4.4 for different array spacing of 0.6λ, 0.7λ, and 0.8λ respectively. All four PAs are operated at the same power level with DPD applied to ensure fair comparison and ideal

Four Chain Measurement with SISO DPD (31 coeff.): PA variation								
PA#	NMSE (%)		ACPR Left (dB)		ACPR Right (dB)		Average DE (%)	Average Power (dBm)
	Before DPD	After DPD	Before DPD	After DPD	Before DPD	After DPD		
PA1	9.8	6.0	-33.1	-43.8	-31.7	-44.8	21	27.4
PA2	12.4	5.2	-35.8	-43.7	-34.2	-44.5	21	27.4
PA3	9.3	6.8	-34.3	-43.7	-32.5	-46.8	21	27.4
PA4	13.4	7.3	-34.2	-45.1	-31.2	-45.5	21	27.4
Four Chain Measurement with DISO DPD (43 coeff.): PA variation								
PA#	NMSE (%)		ACPR Left (dB)		ACPR Right (dB)		Average DE (%)	Average Power (dBm)
	Before DPD	After DPD	Before DPD	After DPD	Before DPD	After DPD		
PA1	9.8	1.4	-32.9	-48.4	-31.6	-49.3	21	27.4
PA2	11.6	1.1	-35.8	-50.0	-34.2	-50.7	21	27.4
PA3	9.3	1.9	-34.3	-47.8	-32.5	-48.6	21	27.4
PA4	13.4	2.1	-34.3	-47.7	-32.2	-48.6	21	27.4

Table 4.2: Modulated signal measurement results for individual PAs within 2x2 array at 0.6λ

transmitter array operation. At 0.6λ spacing with SISO DPD applied, all four PAs exhibit similar efficiencies however the linearity performance is unacceptable with NMSE averaging around 6.3% and ACPR around -44.7dBc. It is clear that in terms of single PA linearity performance, 0.6λ spacing with -21.4 array coupling cannot be linearized with SISO DPD due to significant cross-talk. At 0.7λ spacing with SISO DPD applied, a similar trend can be observed from 0.6λ for 0.7λ spacing with slight linearity performance. All four PAs exhibit the same efficiency levels as 0.6λ, and the linearity performance is improved with NMSE averaging around 4.2% and ACPR around -46.5dBc. The same is true for 0.8λ spacing with SISO DPD applied, all four PAs exhibit the same efficiency levels as 0.6λ and 0.7λ, and the linearity performance is the same as 0.7λ. The difference between 0.7λ and 0.8λ is negligible in terms of linearity, power, and efficiency for each PAs, suggesting the extra coupling improvement from -24.0 dB to -26.3 dB is not needed for SISO DPD. With DISO DPD however, at 0.6λ, a significant improvement can be seen in terms of linearity with NMSE averaging around 1.6% and ACPR around -48.9dBc compared to NMSE around 4.2% and ACPR around -46.5dBc with SISO DPD. The improvement in linearity from SISO to DISO is significant especially considering NMSE. At 0.7λ and 0.8λ

Four Chain Measurement with SISO DPD (31 coeff.): PA variation								
PA#	NMSE (%)		ACPR Left (dB)		ACPR Right (dB)		Average DE (%)	Average Power (dBm)
	Before DPD	After DPD	Before DPD	After DPD	Before DPD	After DPD		
PA1	7.8	3.6	-32.8	-45.4	-31.3	-46.4	21	27.4
PA2	11.0	4.6	-35.8	-46.9	-34.6	-48.2	21	27.4
PA3	8.5	4.8	-34.7	-45.9	-33.1	-46.9	21	27.4
PA4	10.3	3.8	-33.2	-45.8	-31.5	-46.7	21	27.4
Four Chain Measurement with DISO DPD (43 coeff.): PA variation								
PA#	NMSE (%)		ACPR Left (dB)		ACPR Right (dB)		Average DE (%)	Average Power (dBm)
	Before DPD	After DPD	Before DPD	After DPD	Before DPD	After DPD		
PA1	7.8	1.4	-32.8	-49.1	-31.3	-49.7	21	27.4
PA2	10.6	2.2	-35.8	-50.5	-34.6	-52.0	21	27.4
PA3	8.4	2.8	-34.7	-48.6	-33.1	-49.6	21	27.4
PA4	10.4	2.3	-33.2	-48.0	-31.5	-48.9	21	27.4

Table 4.3: Modulated signal measurement results for individual PAs within 2x2 array at 0.7λ

spacing with DISO DPD applied same linearity performance is also observed for all PAs, suggesting the DISO DPD can calibrate for various coupling levels from -21.4 dB to -26.3 dB. Overall, DISO DPD can linearize the PAs close to the linearity of singular PA connected with antenna, regardless of array spacing between 0.6λ to 0.8λ. SISO DPD however, cannot achieve satisfactory NMSE for all spacing between 0.6λ to 0.8λ.

Monitoring the PAs outputs in a 2x2 transmitter setup may not truly reflect the transmitted signal quality since outputs from each antenna will combine vectorially in air and form signals that are different from each PA output. To account for this combination, new performance indicators are used for overall transmitter evaluation instead of each PA antenna chain. The normalized mean square error (NMSE) of the combined signal is calculated by comparing the vectorially combined output signal of all four PAs to the vectorially combined input signal. A similar concept can be said for the adjacent channel power ratio (ACPR) of the combined signal, which is found by comparing the in-band and out-of-band emissions of the vectorially combined output signal. These new calculation methods can yield a similar result to measuring ACPR and NMSE over-the-air at bore-sight to compensate for the lack of OTA measurement in this setup. The spectrum plots are shown

Four Chain Measurement with SISO DPD (31 coeff.): PA variation								
PA#	NMSE (%)		ACPR Left (dB)		ACPR Right (dB)		Average DE (%)	Average Power (dBm)
	Before DPD	After DPD	Before DPD	After DPD	Before DPD	After DPD		
PA1	9.2	4.6	-32.8	-46.3	-31.3	-47.3	21	33.4
PA2	11.5	4.0	-36.3	-48.2	-34.7	-49.6	21	33.4
PA3	7.9	4.5	-34.5	-46.2	-32.6	-47.6	21	33.4
PA4	12.4	3.9	-33.2	-46.2	-30.1	-46.7	21	33.4
Four Chain Measurement with DISO DPD (43 coeff.): PA variation								
PA#	NMSE (%)		ACPR Left (dB)		ACPR Right (dB)		Average DE (%)	Average Power (dBm)
	Before DPD	After DPD	Before DPD	After DPD	Before DPD	After DPD		
PA1	9.2	1.8	-32.8	-49.0	-31.3	-49.7	21	33.4
PA2	11.3	2.0	-36.2	-52.4	-34.6	-53.7	21	33.4
PA3	7.9	2.6	-34.5	-48.9	-32.6	-50.1	21	33.4
PA4	12.3	1.9	-33.2	-47.9	-31.0	-48.4	21	33.4

Table 4.4: Modulated signal measurement results for individual PAs within 2x2 array at 0.8λ

in Figure 4.14 for overall transmitter performance in 2x2 setup with 0.6λ, 0.7λ and 0.8λ array spacing. 5G 3GPP [1] technical specification documents present a minimum ACPR limit of 45dB for a typical sub-6GHz BS requirement, this standard will be a key indicator to evaluate the 2x2 front-end demonstrator results and analysis.

The comparison for overall transmitter performance is compiled in Table 4.5 for different array spacing. The ACPR, efficiency, and power of the overall combined signal follow the same behavior as individual PA output signal results with the exception of NMSE. A major difference can be seen between the NMSE of individual PA output signals and the NMSE of the combined signal, the overall NMSE is significantly improved with SISO DPD at 0.6λ from 6.3% to 2.7%, at 0.7λ from 4.2% to 2.9% and at 0.8λ from 4.2% to 3.2%. So, while SISO performance at 0.6λ spacing is unsatisfactory for individual PA output signals, the combined signal shows viable performance with NMSE at 2.7% and ACPR at -45 dBc. Similar evaluation can be said for 0.7λ and 0.8λ with SISO DPD. Aside from the NMSE difference, the combined signal performances follow closely with regards to individual PA output signals results. SISO DPD can linearize the combined signal, and ACPR improves as spacing increases, approaching DISO DPD results as coupling levels decrease. DISO

DPD can linearize the combined signal regardless of spacing with similar output power and efficiency.

Four Chain Measurement with SISO DPD (31 coeff.): array spacing variation								
Array Spacing	NMSE of Combined Signal (%)		ACPR of Combined Signal Left (dB)		ACPR of Combined Signal Right (dB)		Average DE (%)	Average Power (dBm)
	Before DPD	After DPD	Before DPD	After DPD	Before DPD	After DPD		
0.6 λ	9.4	2.7	-34.4	-44.3	-32.7	-45.0	21.5	33.4
0.7 λ	9.5	2.9	-34.4	-46.5	-32.6	-47.0	21.3	33.4
0.8 λ	9.4	3.2	-34.4	-47.1	-32.7	-47.9	21.0	33.4
Four Chain Measurement with DISO DPD (43 coeff.): array spacing variation								
Array Spacing	NMSE of Combined Signal (%)		ACPR of Combined Signal Left (dB)		ACPR of Combined Signal Right (dB)		Average DE (%)	Average Power (dBm)
	Before DPD	After DPD	Before DPD	After DPD	Before DPD	After DPD		
0.6 λ	9.2	1.3	-34.4	-48.5	-32.7	-49.2	21.3	33.4
0.7 λ	10.2	1.3	-34.7	-49.2	-32.9	-49.8	21.2	33.4
0.8 λ	9.4	1.3	-34.7	-49.4	-32.8	-50.2	21.0	33.4

Table 4.5: Modulated signal measurement results for different spacings with SISO and DISO DPD

From the analysis made above with each PA output signal and overall combined signal performances, a few conclusions can be made regarding 2x2 transmitter operations. In summary, first, the output power per PA and drain efficiency varied negligibly regardless of antenna cross-talk levels, which suggests the average drain impedance seen by the transistors to be constant, despite excursions due to cross-talk induced load modulation. Second, linearity degrades as cross-talk increases, with the ACPR of the combined class AB PA signal varying from -44 dBc to -48 dBc under SISO DPD, however the improvement plateaus as coupling level decrease past -24dB. On the other hand, DISO DPD is able to linearize the 2x2 transmitter to nearly the same level as the single PA with antenna load (ACPR below -48 dBc in all cases). Third, the combined signal NMSE doesn't show the improvement over larger spacing, unlike individual PA output signal NMSE performance. The cross-talk interference does not scale with NMSE performance can be possibly due to the averaging of constructive and destructive interference within the band to be constant. While ACPR does show a trend with regards to antenna spacing, suggesting the antenna

cross-talk mainly affects and scales with out-of-band distortions.

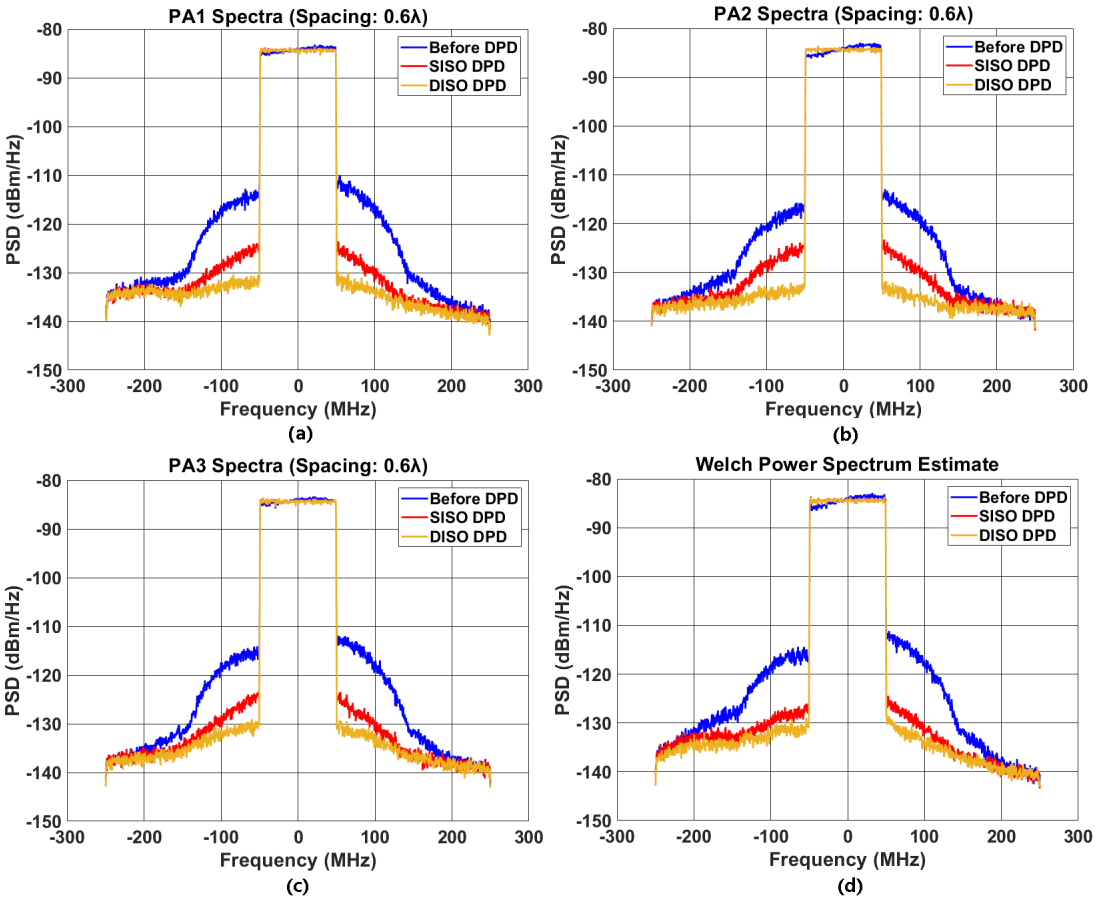

Figure 4.11: 2x2 modulated signal measurement results at 0.6λ for: (a) PA1, (b) PA2, (c) PA3, (d) PA4.

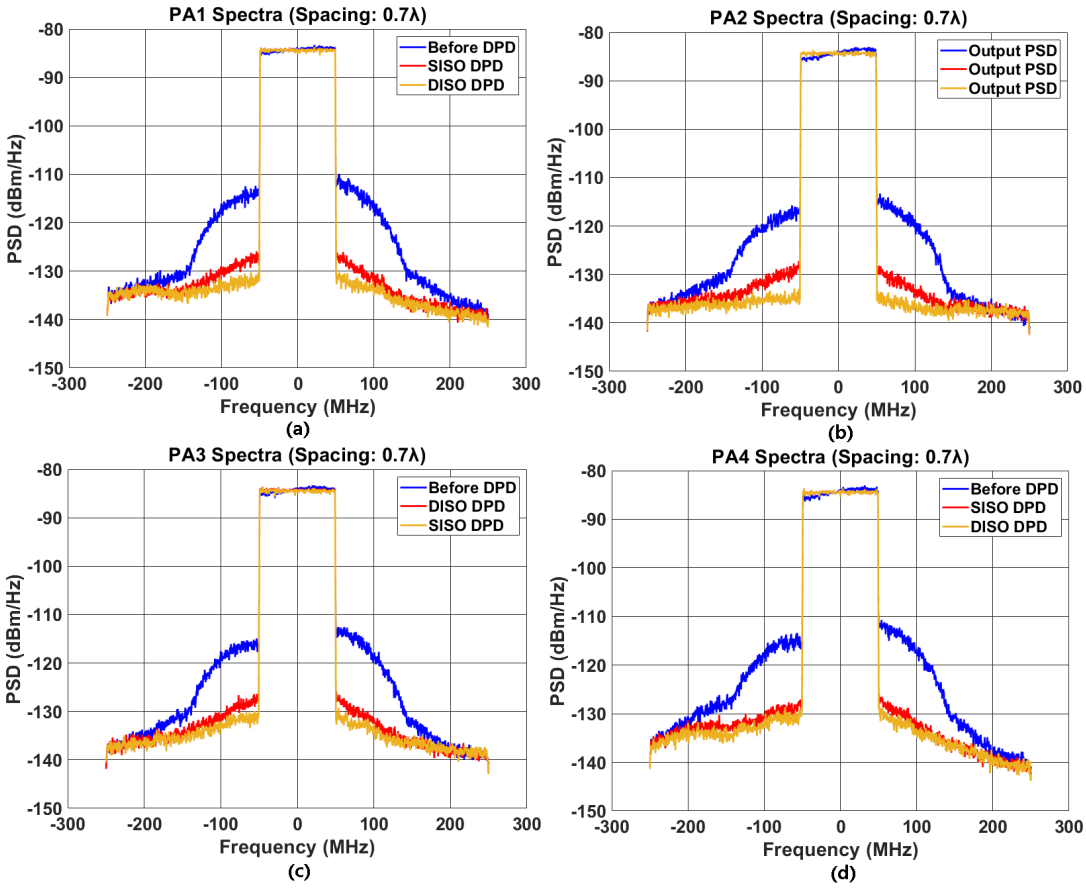

Figure 4.12: 2x2 modulated signal measurement results at 0.7λ for: (a) PA1, (b) PA2, (c) PA3, (d) PA4.

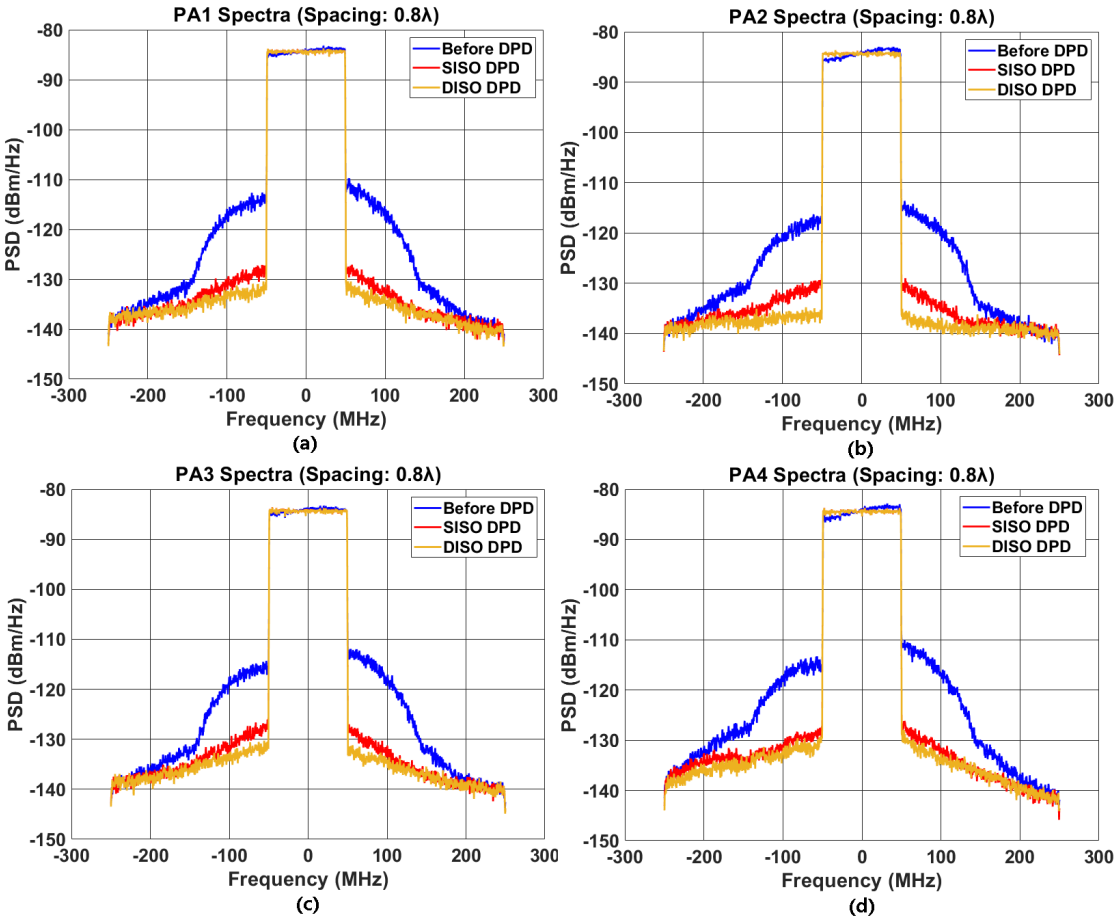

Figure 4.13: 2x2 modulated signal measurement results at 0.8λ for: (a) PA1, (b) PA2, (c) PA3, (d) PA4.

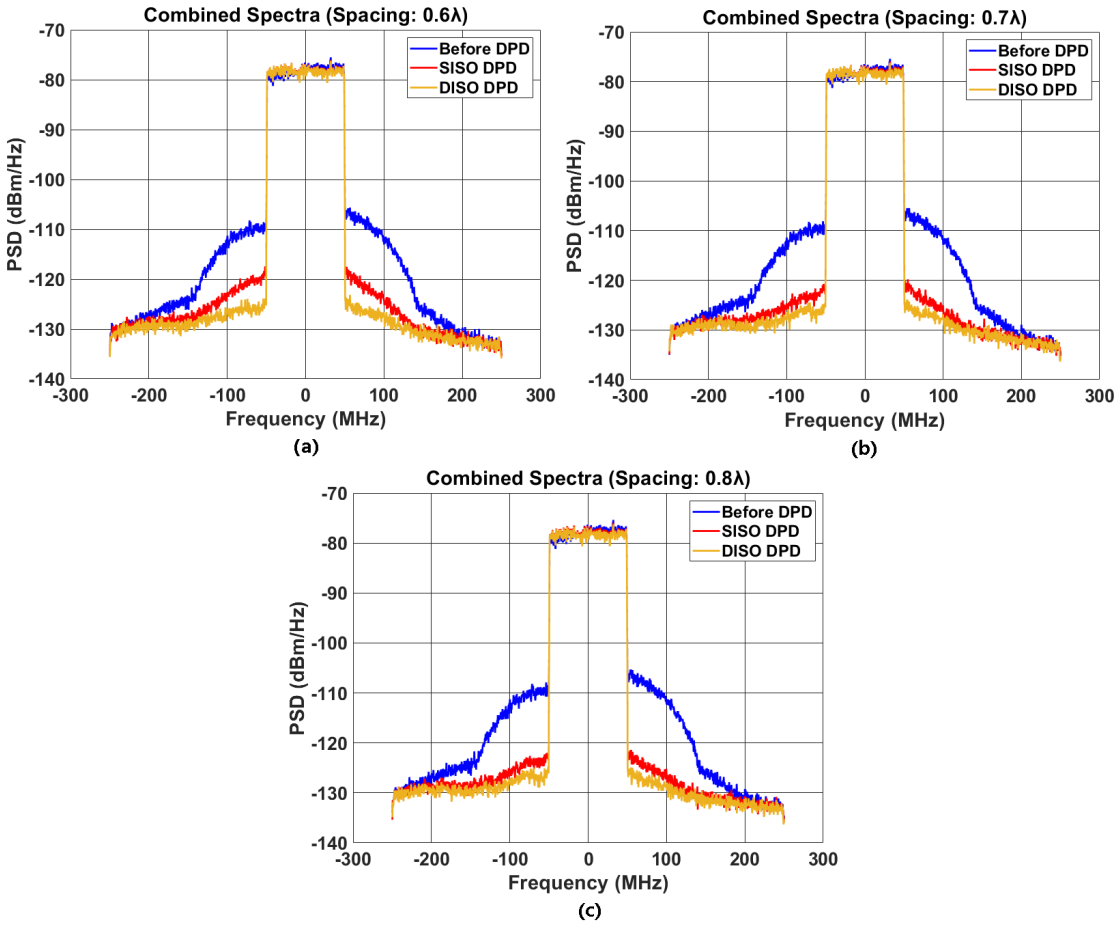

Figure 4.14: 2x2 modulated signal measurement results of combined output at: (a) 0.6λ, (b) 0.7λ, (c) 0.8λ.

Chapter 5

Conclusions and future work

5.1 Conclusions

The evolution from 4G to 5G and the anticipated 100x capacity improvement required by our ever-increasing demand for data requires a fundamental change in cellular communication RF system architecture and design. In 5G, due to the increased number of RF chains in the transmitter system, each PA's output power is significantly lowered compared to that in 4G. The trade-off of PA efficiency over linearity is no longer valid, as using DPD to compensate for nonlinearity may lead to more power lost than gained from individual PA efficiency. Additional issues such as PA load mismatch and cross-talk induced load modulation also significantly affect PA performance. A literature review was conducted for sub-6 GHz PAs with reduced load sensitivity, BS antenna designs, and sub-6GHz mMIMO transmitter architecture implementations. However, for sub-6GHz mMIMO transmitter architectures, the literature is more populated by works focused on DPD system implementation rather than circuit-focused system implementation. The majority of work uses simple and close to ideal circuit elements within their systems, thus critical information regarding trade-offs between circuit-level designs and system specifications are missing. This gap calls for a circuit-focused system implementation of a sub-6GHz mMIMO transmitter. This paper presents an experimental study of the effects of antenna cross-talk on the linearizability and efficiency of 5G sub-6GHz wide-band mMIMO transmitters.

The transmitter studied in this work consists of a 2x2 array of class AB PAs connected to an antenna array with a re-configurable spacing. A vast BS antenna design survey was conducted and an optimal antenna structure was chosen with both electrical and mechanical considerations for mMIMO implementations. In the end, a modular wide-band

and high isolation 2x2 patch antenna array was designed, capable of varying inter-element spacing. A class AB PA array was also designed with high linearity and high efficiency over a 3.2-3.8GHz bandwidth. The PA was shown to be linearizable in modulated signal testing with signal bandwidths up to 200MHz. Lastly, a modular front-end frame was made to house the 2x2 antenna array with up to eight PAs. The frame was designed for high integration between the antenna and PA elements with the ability to scale up to a 4x4 or 8x8 configuration.

Modulated signal measurements were conducted to investigate the effect of PA mismatch and array cross-talk in the 2x2 transmitter system. The ability of SISO and DISO DPD techniques to linearize the PA arrays was assessed under 5G-candidate 100 MHz OFDM test signals. The measurement results revealed that antenna load mismatch was the dominant factor degrading performance in the MIMO system, impacting output power, efficiency and linearity significantly. Antenna cross-talk mainly impacted linearity, degrading ACPR under SISO DPD, but DISO DPD was able to successfully linearize the transmitter front-end (ACPR below -48 dBc) in all array spacing variations.

5.2 Future work

The current work only conducted experiments for a 2x2 sub-6GHz MIMO transmitter front-end. The size of this array is too limited and leaves much to be desired. Future work should extend the array up to 4x4 and 8x8 versions. This would be crucial to provide a fuller picture of mMIMO transmitter operation. The up-scaling would require more attention to key considerations such as integration of the PA and driver, advanced cooling methods, DC control board, and cable management. In the future, as hardware, test equipment, and testing space becomes more readily available, dual-polarized MIMO transmitter measurements should also be done for the 2x2x2 PA array for a true 5G BS transmitter experiment. Although simulation results showed limited variation in performance between the single and dual-polarized operations due to the high isolation and cross-polarization of the antennas, measurement validation is needed. Another key step would be conducting over-the-air testing, where a far-field probe antenna would be able to receive, combine and down-convert the signal to obtain ACPR, EVM, and NMSE of the transmitted signal. Multiple test cases, from simple line-of-sight to complex EM environment recreations are needed to fully understand the overall system effect of key design decisions made for transmitter front-ends.

As for antenna performance, improvements can be made in terms of lowering the size of individual elements (down to 0.5λ) to enable array spacings of 0.5λ instead of the

concurrent 0.6λ to fully study the trade-offs between array radiation patterns and antenna cross-talk interference on the overall transmitter performance. Another key enhancement would be to improve the in-band matching. From the experiments conducted as part of this work, it was verified that by migrating from an ideal 50Ω load to the antenna load, significant power, efficiency, and linearity were lost in terms of PA modulated signal operation. This was partially due to the hand-soldered couplers' poor performance and partially due to the antenna matching. Once antenna matching is enhanced, the load seen by the PA would more closely approximate 50Ω, and the loss in the performance would be lowered.

As for the PA performance, improvements could be found by utilizing advanced PA techniques to reduce load sensitivity. From the literature review, it was evident that the current load sensitivity reduction techniques all require a much more complex design while offering limited load sensitivity reductions. A simpler and more effective technique would be needed for the practical implementation of BS PAs due to the size limitations for higher integration. Another approach would be to co-design the PA and antenna elements. This concept is rather risky, however, since the PA would be designed with a certain antenna in mind and as a consequence might have reduced flexibility. Co-design would require very well simulated or measured S-parameters of the antenna input since the load which the PA experiences contributes significantly towards power and efficiency. The designed PA would not be able to be evaluated under standard CW measurements as the PA would no longer be designed for ideal 50Ω termination. A solid and hard connection must be achieved between the PA and the antenna since any interference or instability will cause performance loss for the PA. However, the co-design method would eliminate or improve the mismatch performance loss experienced during testing which is significant.

References

[1] 5G 3GPP. Base station (bs) radio transmission and reception (3gpp ts 38.104 version 15.2.0 release 15). July 2018.

[2] Jeffrey G. Andrews, Stefano Buzzi, Wan Choi, Stephen V. Hanly, Angel Lozano, Anthony C. K. Soong, and Jianzhong Charlie Zhang. What will 5g be. *IEEE Journal on Selected Areas in Communications*, 32(6):1065–1082, 2014.

[3] Alireza Asoodeh, Hossein Miri Lavasani, Mengye Cai, and Shahriar Mirabbasi. A highly linear and efficient 28-ghz pa with a psat of 23.2 dbm, p1 db of 22.7 dbm, and pae of 35.5 in 65-nm bulk cmos. *IEEE Journal of Solid-State Circuits*, 56(3):914–927, 2021.

[4] Constantine A Balanis. *Antenna theory: analysis and design*. Wiley-Interscience, 2005.

[5] F. M. Barradas, P. M. Tomé, J. M. Gomes, T. R. Cunha, P. M. Cabral, and J. C. Pedro. Power, Linearity, and Efficiency Prediction for MIMO Arrays With Antenna Coupling. 65(12):5284–5297, December 2017.

[6] C. Fager, X. Bland, K. Hausmair, J. C. Cahuana, and T. Eriksson. Prediction of Smart Antenna Transmitter Characteristics Using a New Behavioral Modeling Approach. In *2014 IEEE MTT-S International Microwave Symposium*, pages 1–4, Tampa, FL, USA, 2014.

[7] Yue Gao, Runbo Ma, Yapeng Wang, Qianyun Zhang, and Clive Parini. Stacked patch antenna with dual-polarization and low mutual coupling for massive mimo. *IEEE Transactions on Antennas and Propagation*, 64(10):4544–4549, 2016.

[8] Bersant Gashi, Sebastian Krause, Rüdiger Quay, Christian Fager, and Oliver Ambacher. Investigations of active antenna doherty power amplifier modules under beam-

steering mismatch. *IEEE Microwave and Wireless Components Letters*, 28(10):930–932, 2018.

[9] Cristiano F. Goncalves, Filipe M. Barradas, Pedro M. Cabral, and José Carlos Pedro. Switch-based variable length stubs network for pa load sensitivity reduction. *IEEE Access*, 7:152576–152584, 2019.

[10] R. Harrington and J. Mautz. Theory of characteristic modes for conducting bodies. *IEEE Transactions on Antennas and Propagation*, 19(5):622–628, 1971.

[11] K. Hausmair, S. Gustafsson, C. Sánchez-Pérez, P. N. Landin, U. Gustavsson, T. Eriksson, and C. Fager. Prediction of Nonlinear Distortion in Wideband Active Antenna Arrays. 65(11):4550–4563, November 2017.

[12] Katharina Hausmair, Per N. Landin, Ulf Gustavsson, Christian Fager, and Thomas Eriksson. Digital predistortion for multi-antenna transmitters affected by antenna crosstalk. *IEEE Transactions on Microwave Theory and Techniques*, 66(3):1524–1535, 2018.

[13] Pavel Hazdra, M. Mazanek, and Jiri Cermak. Wideband rectangular microstrip patch antenna using l-probe feeding system. *Radioengineering*, 16, 09 2007.

[14] Walter Honcharenko. Sub-6 ghz mmimo base stations meet 5g's size and weight challenges. *Microwave Journal*, 2019.

[15] Song Hu, Shouhei Kousai, and Hua Wang. Antenna impedance variation compensation by exploiting a digital doherty power amplifier architecture. *IEEE Transactions on Microwave Theory and Techniques*, 63(2):580–597, 2015.

[16] Y.L. Chow K.M. Luk, C.L. Mak and K.F. Lee. Broadband microstrip patch antenna. *Electronics Letters*, 34:1442–1443(1), July 1998.

[17] Shunli Li, Zhi Ning Chen, Teng Li, Feng Han Lin, and Xiaoxing Yin. Characterization of metasurface lens antenna for sub-6 ghz dual-polarization full-dimension massive mimo and multibeam systems. *IEEE Transactions on Antennas and Propagation*, 68(3):1366–1377, 2020.

[18] Yapeng Li, Zhipeng Zhao, Zhaoyang Tang, and Yingzeng Yin. Differentially fed, dual-band dual-polarized filtering antenna with high selectivity for 5g sub-6 ghz base station applications. *IEEE Transactions on Antennas and Propagation*, 68(4):3231–3236, 2020.

[19] Wei Liu, Zhi Ning Chen, and Xianming Qing. Metamaterial-based low-profile broadband mushroom antenna. *IEEE Transactions on Antennas and Propagation*, 62(3):1165–1172, 2014.

[20] Wei Liu, Zhi Ning Chen, and Xianming Qing. Metamaterial-based low-profile broadband aperture-coupled grid-slotted patch antenna. *IEEE Transactions on Antennas and Propagation*, 63(7):3325–3329, 2015.

[21] Jie Lu, Zhenqi Kuai, Xiaowei Zhu, and Nianzu Zhang. A high-isolation dual-polarization microstrip patch antenna with quasi-cross-shaped coupling slot. *IEEE Transactions on Antennas and Propagation*, 59(7):2713–2717, 2011.

[22] Lu Lu, Geoffrey Ye Li, A. Lee Swindlehurst, Alexei Ashikhmin, and Rui Zhang. An overview of massive mimo: Benefits and challenges. *IEEE Journal of Selected Topics in Signal Processing*, 8(5):742–758, 2014.

[23] K.M. Luk and Hang Wong. A new wideband unidirectional antenna element. *Int J Microwave Opt Technol*, 1, 01 2006.

[24] Q. Luo, X. Zhu, C. Yu, and W. Hong. Single-Receiver Over-the-Air Digital Predistortion for Massive MIMO Transmitters With Antenna Crosstalk. 68(1):301–315, January 2020.

[25] Haifeng Lyu and Kenle Chen. Balanced-to-doherty mode-reconfigurable power amplifier with high efficiency and linearity against load mismatch. *IEEE Transactions on Microwave Theory and Techniques*, 68(5):1717–1728, 2020.

[26] Ka Ming Mak, Xia Gao, and Hau Wah Lai. Low cost dual polarized base station element for long term evolution. *IEEE Transactions on Antennas and Propagation*, 62(11):5861–5865, 2014.

[27] Ka Ming Mak, Hua Wah Lai, and Kwai Man Luk. A 5g wideband patch antenna with antisymmetric l-shaped probe feeds. *IEEE Transactions on Antennas and Propagation*, 66(2):957–961, 2018.

[28] Nian-Sheng Nie, Xue-Song Yang, Zhi Ning Chen, and Bing-Zhong Wang. A low-profile wideband hybrid metasurface antenna array for 5g and wifi systems. *IEEE Transactions on Antennas and Propagation*, 68(2):665–671, 2020.

[29] D Pozar. Microstrip antenna aperture-coupled to a microstripline. *Electronics Letters*, 21:49, January 1985.

[30] Jia-Nan Sun, Jia-Lin Li, and Lei Xia. A dual-polarized magneto-electric dipole antenna for application to n77/n78 band. *IEEE Access*, 7:161708–161715, 2019.

[31] C.H. Tsao, Y.M. Hwang, F. Kilburg, and F. Dietrich. Aperture-coupled patch antennas with wide-bandwidth and dual-polarization capabilities. In *1988 IEEE AP-S. International Symposium, Antennas and Propagation*, pages 936–939 vol.3, 1988.

[32] Jiafu Wang, Yue Li, Zhi Hao Jiang, Ting Shi, Ming-Chun Tang, Ziheng Zhou, Zhi Ning Chen, and Cheng-Wei Qiu. Metantenna: When metasurface meets antenna again. *IEEE Transactions on Antennas and Propagation*, 68(3):1332–1347, 2020.

[33] Hang Wong, Ka-Leung Lau, and Kwai-Man Luk. Design of dual-polarized l-probe patch antenna arrays with high isolation. *IEEE Transactions on Antennas and Propagation*, 52(1):45–52, 2004.

[34] Ke-Li Wu, Changning Wei, Xide Mei, and Zhen-Yuan Zhang. Array-antenna decoupling surface. *IEEE Transactions on Antennas and Propagation*, 65(12):6728–6738, 2017.

[35] Junfeng Xu, Wei Tai, and David S. Ricketts. A transmission line based resistance compression network (trcn) for microwave applications. In *2013 IEEE MTT-S International Microwave Symposium Digest (MTT)*, pages 1–3, 2013.

[36] Hang Yu, Emile Traore, Mohammed Almoneer, Jin Gyu Lim, Jingjing Xia, and Slim Boumaiza. Experimental study of the effects of antenna crosstalk on the linearity and efficiency of 5g sub-6 ghz wideband 2x2transmitter arrays. *IMS2021*, June 2021.

[37] Yujuan Zhang. Experimental investigation of the power amplifiers' nonlinearity using a 3.5 ghz two-by-two rf front-end prototype, 2020.

[38] Zhen-Yuan Zhang and Ke-Li Wu. Double torsion coil feeding structure for patch antennas. *IEEE Transactions on Antennas and Propagation*, 67(6):3688–3694, 2019.